R. Müller

Bio-Inspired Flexible Vertebral Drill

The design, manufacturing and evaluation of a prototype

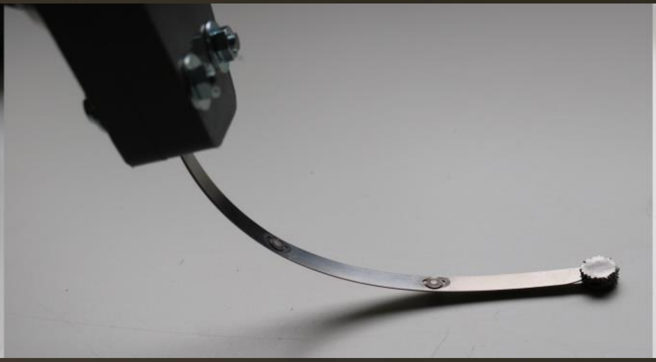

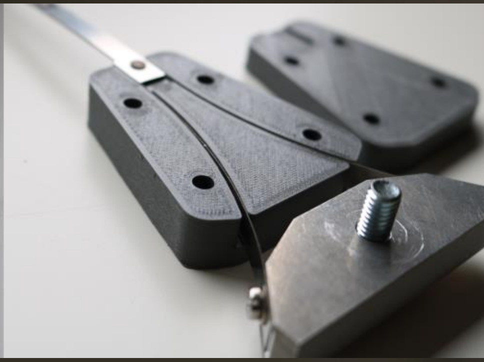

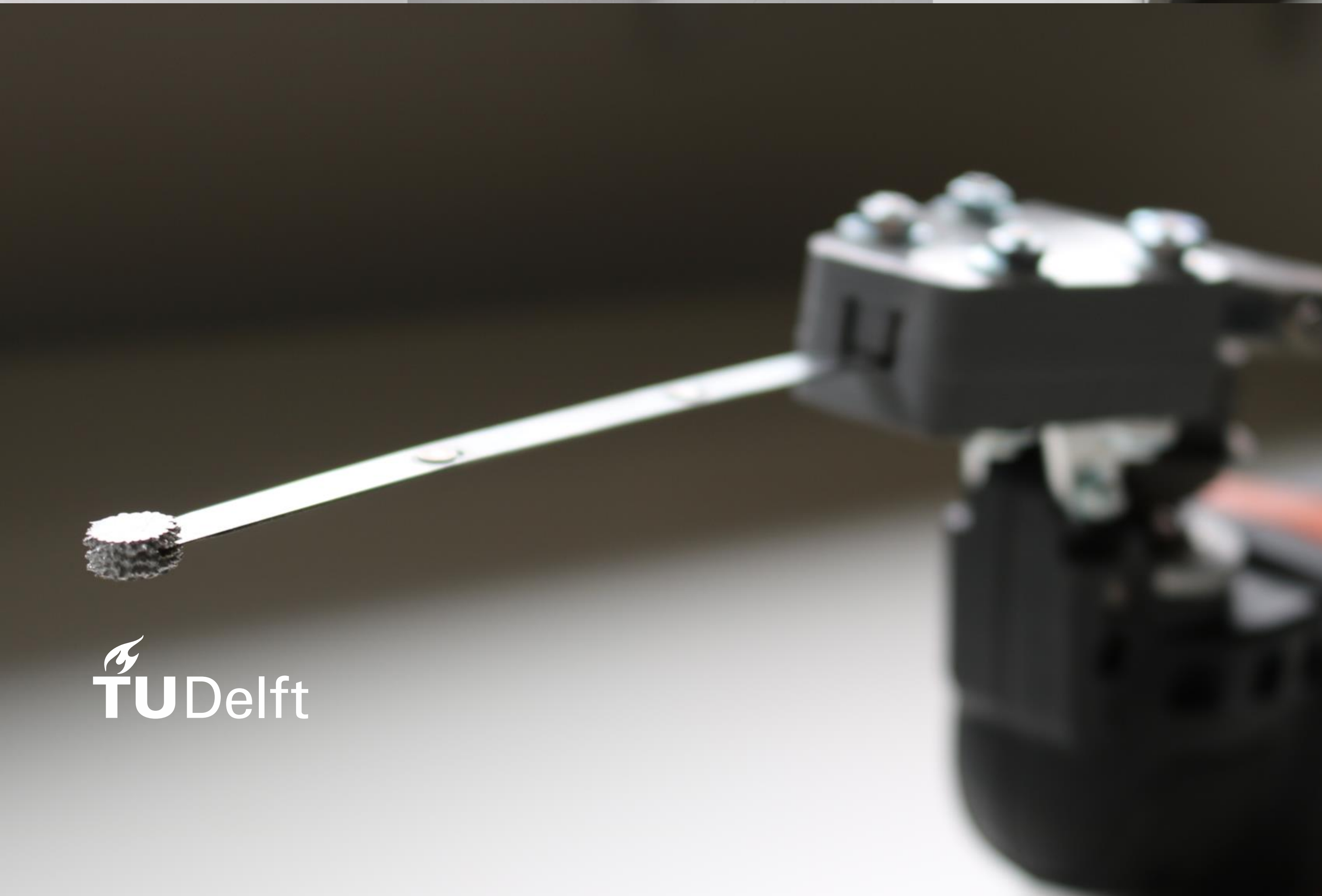

Bio-Inspired Flexible Vertebral Drill

The design, manufacturing and evaluation of a prototype

By

R. Müller

in partial fulfilment of the requirements for the degree of

Master of Science
in Mechanical Engineering

at the Delft University of Technology,
to be defended publicly on Monday January 24th, 2022 at 14:00.

Supervisor:	Ir. E.P. de Kater	
Thesis committee:	Prof. dr .ir. P. Breedveld,	TU Delft
	Dr. ir. A. Sakes,	TU Delft
	Ir. E.P. de Kater,	TU Delft

This thesis is confidential and cannot be published until January 16th, 2024.
For an electronic version of this thesis visit http://repository.tudelft.nl/.

Contents

Bio-Inspired Flexible Vertebral Drill

R. Müller

***Abstract*—Spinal fusion surgery is an operation in which two or more adjacent vertebrae are rigidly connected, with the goal to remedy spinal instability, deformation of the vertebrae, or a herniated intervertebral disc. Vertebrae are conventionally fixated by means of pedicle screws, the downsides of which are accidental cortical wall breaches during drilling and poor holding strength of the screw. The holding strength of the bone anchor may be improved by increasing its contact area with the hard cortical wall of the vertebral body. To accomplish this, a curved hole needs to be made along the inside of the cortical wall. This research presents the design, manufacturing, and testing of a bone drilling device, that is flexible in one plane. To this end, the drill was developed on the basis of the tsetse fly's proboscis, which is a mechanism that uses a cutting surface with its axis of rotation perpendicular to the drilling direction. Implementing this cutting motion has several advantages over conventional drilling: It facilitates using leaf springs as a flexible transmission, and it is not limited to drilling round holes. A prototype was built and tested on Sawbones closed cell foam, which closely mimics the mechanical properties of the cancellous bone found in human vertebrae. The prototype was capable of effectively cutting through foam with densities up to 10 pounds per cubic foot (PCF) with a feed rate of 50 mm/min. The ability to deflect off and follow a simulated cortical wall was also tested, and proved to be effective up to an insertion angle of 15°. The bio-inspired drilling device presented in this research opens up new possibilities in the development of flexible drilling for a wide variety of orthopaedic applications.**

***Index Terms*— Flexible drilling, vertebral drilling, spinal fusion surgery, bio-inspired.**

I. INTRODUCTION

A. Spinal Fusion Surgery

Anatomy of the human spine

The vertebral column, or spinal column, provides stability and mobility to the human body and protects the spinal cord [1]. From the skull down to the pelvis, the vertebral column can be divided into three areas; 1) the cervical area in the neck, 2) the thoracic area that forms the upper back, and 3) the lumbar area that forms the lower back. Each vertebra consists of two main elements: The cylindrical vertebral body, which supports the applied load, and the vertebral arch, which is connected to the vertebral body by its two pedicles. The vertebral arch consists of the pedicles, laminae and the spinous and transverse processes. The vertebral canal, which is formed by the vertebral body and vertebral arch, securely contains the spinal cord. The vertebrae are connected to each other by intervertebral discs, which absorb shocks and transmit forces between the vertebrae. The intervertebral discs also allow for relative movement of the adjacent vertebrae. The flexible structure that consists of two vertebrae and the intervertebral disc between them is called an interbody joint. The interbody joints provide the spinal column its flexibility [2]. A schematic representation of the human vertebra can be seen in Figure 1.

The vertebral body is not a homogenous cylinder, instead it has a hard and compact outer layer and a softer porous inner structure. The compact bone of the outer layer is called cortical bone and the porous inside is called cancellous or trabecular bone. Both cortical and cancellous bone have a true density in the range of 1600 – 1900 kg/m^3 [3], however they are distinguished by their different porosities. Cortical and cancellous bone have a porosity of 5 – 30 % and 30 – 90%, respectively. The cortical outer wall is approximately 0.4 mm thick [1], but the transition region from cancellous to cortical

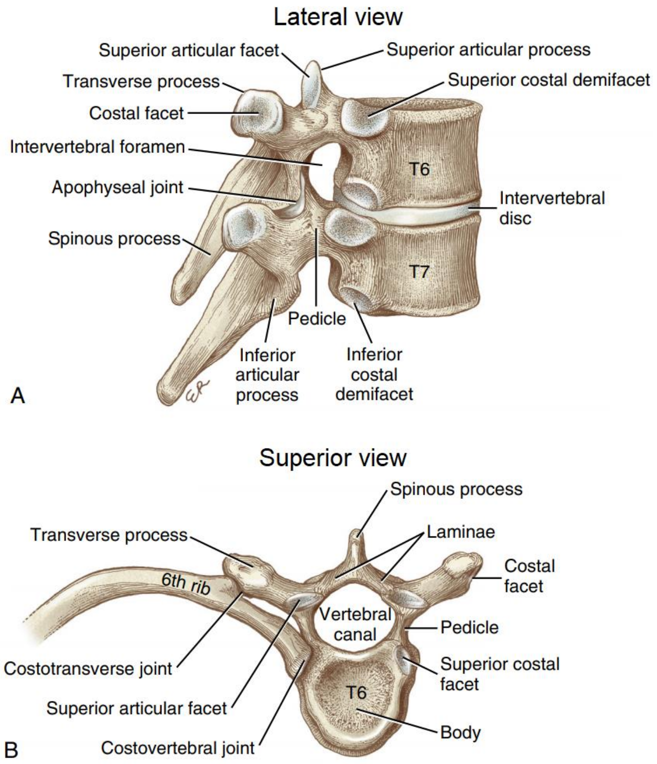

Figure 1: The major characteristics of the human vertebra. A: Lateral view of the T6 and T7 vertebrae with the intervertebral disc. B: Superior view of the T6 vertebra showing the vertebral canal. (Figure adapted from Neumann [51].)

bone is in the range of 3 mm [4]. The pillars that form the porous cancellous bone, which are called trabeculae, have a mean width of approximately 0.13 mm. The mean distance between these pillars, the mean intertrabecular space, is in the range of 1 mm [5]. A cross section of a vertebra, clearly showing the cortical and cancellous bone, is shown in Figure 2.

Surgical approach

Spinal fusion is an operation in which two or more adjacent vertebrae are rigidly connected. This rigid connection fixates the vertebrae with respect to each other, thus negating the interbody joint. There are several reasons why spinal fusion operations might be performed, the first of which is spinal instability. Spinal instability implies that the spinal column is no longer able to support its load, which can be caused by degeneration of the cancellous bone, osteoporosis, or due to injury. Another reason to perform spinal fusion surgery is deformation of the vertebrae caused by, for instance, scoliosis. In this case, fixation of the vertebrae keeps them properly aligned. The third reason is a herniated intervertebral disc. A herniated disc causes pain when it serves a load bearing function. The solution is to bypass the disc by fixating its two opposing vertebrae [1],[6]. The conventional way of fixating thoracic and lumbar vertebrae is by means of rods and screws. The rods hold the vertebrae in place on the posterior side and are connected to them by screws. The screws are placed through the pedicles into the vertebral body, which is why they are referred to as pedicle screws. A schematic illustration of a spinal fusion with rods and pedicle screws is shown in Figure 3. Pedicle screws are produced with different outer diameters such that a screw with a correct outer diameter can be placed. For a solid connection of the screw, it is necessary that the threads cut into the hard cortical outer layer of the pedicle. However, the diameter cannot be too large or it will perforate the pedicle. Breaking a pedicle logically decreases the pull-out strength of the screw, and possibly leads to damage of the spinal cord [1],[7]. A screw diameter of at least 0.5 mm less than the pedicle width is required for safe screw placement [8]. It is important to note that pedicle width varies throughout the spinal column, namely from 3.4 ± 0.6 mm for the T7 vertebra, up to 17.7 ± 2.7 mm for the L5 vertebra [9].

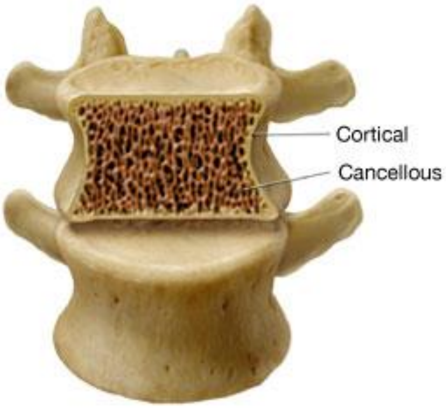

Figure 2: A cross section of a vertebra showing the compact cortical outer layer and the porous cancellous bone inside it. (Figure taken from Malowney [52].)

Figure 3: Spinal fusion by means of pedicle screws and rods on the posterior side. (Figure taken from Weigao Orthopaedic Device [53].)

B. Vertebral Drilling

State of the art

Before the pedicle screws can be inserted through the pedicle, a pilot hole has to be made. The current method of drilling this hole is by means of a pedicle probe. A pedicle probe is a long needle-like instrument with a somewhat curved and blunt tip. After a piece of cortical bone has been removed from the posterior side of the vertebra, the probe is pushed through the cancellous bone beneath it. The probe enters the vertebral body through the pedicle. The surgeon advances the probe through the cancellous bone with manual pressure alone. This conventional way of pedicle screw insertion is illustrated in Figure 4. A downside of this method is that it requires a lot of skill from the surgeon. Perforating the cortical outer wall of the pedicle reduces the holding strength of the screw, but worse, it can cause damage to the surrounding tissue including the spinal cord [1],[7]. The cortical bone wall of the pedicle is used to

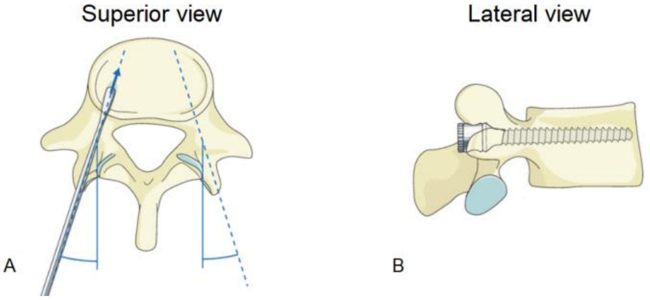

Figure 4: The conventional way of pedicle screw insertion. A: Superior view of a vertebra, a pilot hole is made through the pedicle using a pedicle probe. B: Lateral view of the vertebra with a pedicle screw installed. (Figure adapted from AO Surgery Reference [24].)

navigate the probe through it. Contact with the hard cortical wall will increase the pressure on the probe. However, even for a skilled surgeon, inserting pedicle screws is a high risk operation. With a conventional pedicle probe, a path straight through the centre of the pedicle cannot be guaranteed and it is almost impossible for the surgeon to prevent any perforation of the cortical wall [1]. In fact, cortical wall penetration occurs in 15% - 40% of vertebral screw placement operations [10], [11]. This large range can be attributed to the different methods that were used to identify a cortical breach [7].

Problem analysis

The current methods of through pedicle vertebral drilling and screw insertion leave room for improvement. The first challenge is to ensure that drilling through the pedicle relies less on the skill of the surgeon, than with a conventional pedicle probe. This would reduce the amount of required training as well as the number of cortical wall breaches, which would in turn increase the holding strength of the screw. The second challenge is to increase the pull out strength of the screw by increasing its contact area with the cortical outer layer. A straight screw will engage the cortical layer in the pedicle, but the part that enters the vertebra body is only in contact with cancellous bone. A curved screw or bone anchor, that follows the outer wall of the vertebra, will remain in contact with the cortical layer. This principle is illustrated in Figure 5. This would require a steerable drill that is flexible in at least a two-dimensional plane, such that a curved tunnel along the cortical wall can be created. Another challenge is to minimize the heat that is generated while drilling, because necrosis of the vertebral tissue occurs when it is kept at 47˚C for 1 minute [12]. This is not a problem with a conventional pedicle probe, but it will be when a tool is used that has a high velocity with respect to the vertebral tissue.

C. Tsetse Fly Bio-Inspiration

Piercing mouthparts of the tsetse fly

Piercing organs are abundant within the realm of insects and are used for several different applications, for instance self-defence, attacking prey [13], and laying eggs into a substrate [14]. These structures function on microscale without breaking or buckling and are capable of drilling through hard materials without the need of a high axial load, compared to conventional drilling [15]. In many types of insects, such as flies, mosquitos, moths and bugs, mouthparts have evolved for a specialized form of feeding in which a substance is pierced. For herbivorous insects, this substance can be a plant or fruit, for the purpose of extracting its nutrients. However, in case of blood-feeding insects, the substance is the skin of another animal [16].

Many different mechanisms can be found within the piercing organs of insects. A mechanism, that uses a rotation with its axis perpendicular to the drilling direction, is found in the proboscis of tsetse flies (Diptera). The two parts of the proboscis that form the tip are called labella, these contain both backwards-pointing teeth and rasping ridges that are used to pierce the skin of its host. To initiate penetration, the fly presses its proboscis against the skin of the host and the labella rotate outwards, causing the teeth to cut into it. After the proboscis has entered the skin, the two segments or labella are repeatedly rotated inwards and outwards, each time sinking further into the host. On each rotation, the teeth on the labella cut through the substrate with a rasping motion [17],[18]. The proboscis of the tsetse fly is in the range of 3 mm - 4 mm long and 0.1 mm wide [16]. The ultrastructure of the tsetse fly proboscis tip has been studied by use of a scanning electron microscope as shown in Figure 6.

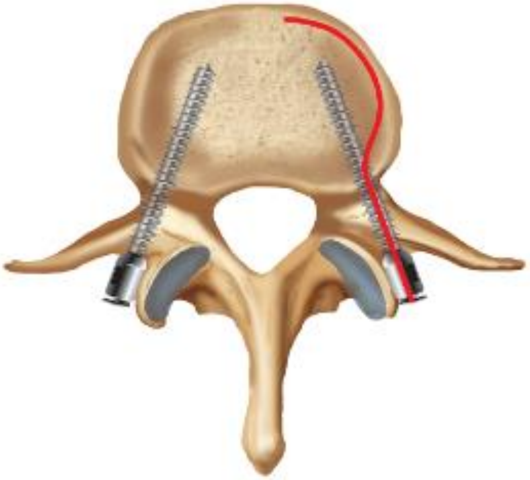

Figure 5: Superior view of a vertebra with two conventional pedicle screws. The red line indicates the curved screw path along the cortical outer layer. (Figure adapted from Chen et al. [54].*)*

Tsetse fly drill mechanism compared to conventional drilling

Implementing the cutting mechanism of the tsetse fly in a flexible bone drilling device has several advantages over the pedicle probe and conventional drills. The use of a rotation with its axis perpendicular to the drilling direction makes it possible to decouple the cutting mechanism from the bending mechanism. This can be done by designing the cutting

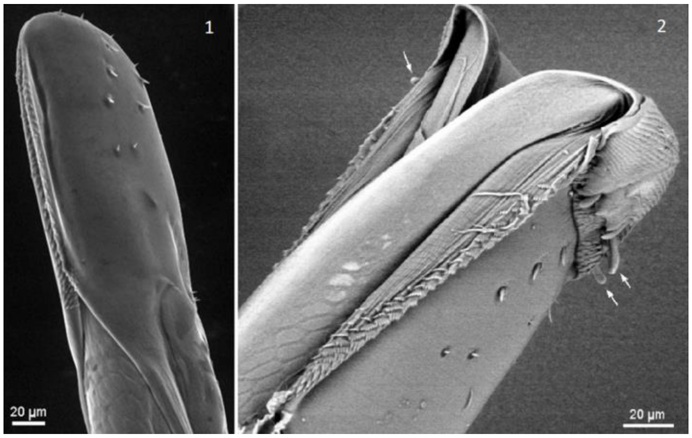

Figure 6: Scanning electron microscopic images of the tsetse fly proboscis. 1 (left): A dorsal view of the proboscis tip with the labella fully inverted. 2 (right): The tip of the proboscis with the labella everted, the teeth and rasping ridges are visible. Gustatory sensilla are indicated with arrows and should not be confused with teeth. (Figure adapted from Gibson et al. [55]*).*

mechanism in a two-dimensional plane, which allows for bending outside of that plane. The plane of bending is thus perpendicular to that of the cutting mechanism. This is impossible to do with a conventional drill, because its rotation is along its longitudinal axis, thus parallel to the drilling direction. This means that the tool continuously rotates with respect to the desired bending direction, meaning that the cutting and bending motions are inherently coupled. That does not mean that conventional drills cannot be made flexible, but it does make doing so more complicated. The flexible surgical drills that are currently in use can only make a curved hole along a predefined path, or with a fixed radius. Multiple patents exist of surgical drills that can actively be steered, but none of them have been commercialised, which may be because of the added complexity [19].

Another advantage over the conventional drill, is the possibility of using asymmetry in the cutting head as a means of steerability. This can for instance be done by creating an angled surface on one side of the tool, which would introduce a lateral force towards the other side, which causes the tool to stray from its straight path. The working principle of steering with a bevelled tip is commonly used by insects like cicada, mosquitoes, and parasitic wasps, which have multiple translating segments in their piercing organ [20].

Furthermore, the rotating motion of the backwards-pointing teeth pulls the proboscis of the tsetse fly into the substrate. Many insects use this principle, of pulling their piercing structure from the front, rather than pushing it from the back, as a means of buckling prevention [21]. As a result, the required axial thrust is lower than that of a pedicle probe or conventional drill, that is actively pushed through the substrate [15]. This decreases the forces on the vertebra, which could reduce the amount of cortical wall breaches.

An important aspect of replacing the pedicle probe with a cutting tool, is material removal. The pedicle probe pushes cancellous bone to the side, which effectively compacts the bone around the pilot hole, whereas a cutting tool removes material from the hole. This design choice can be justified, because compacting the cancellous bone around the pilot hole does not improve the screw holding strength [22].

In conventional drilling, the cross sectional shape of the hole is determined by the rotating motion of the cutting tool. This is however not the case in the tsetse fly mechanism, because the axis of rotation of the cutting head is perpendicular to the drilling direction. Instead, the cross sectional shape of the cutting head determines the shape of the hole that is made. This implies that the device is not restricted to drilling round holes. The shape of the cutting head can thus be adjusted to facilitate innovative bone anchors. One way of improving the holding strength of a bone anchor is to increase its contact with the cortical outer wall of the vertebra. The shape of the drilling device could for instance be adapted to the ovoid cross section of the pedicle [11]. This would, in combination with an ovoid bone anchor, increase the contact area between the anchor and the pedicle. A rectangular cutting head may be suitable to increase the contact area within the vertebral body. As can be seen in Figure 2, the cortical wall of the vertebral body, when viewed from the inside, is convex. The contact area between this convex wall and a round bone anchor is minimal, because two round shapes touch each other in a line contact. Using a rectangular bone anchor would result in an increase in contact area and thus in holding strength. An example of a rectangular bone anchor is the flexible steel tape anchor, presented by Verdult [1]. It is important to realise that screw threads cannot be used in combination with ovoid or rectangular bone anchors, because that would require the anchor to be round in cross section. However, other methods of fixations are possible such as the use of bone cement [1].

D. *Goal of this Research*

The goal of this research is to design and evaluate a bone drilling device, that is flexible in a two-dimensional plane. The drilling device draws inspiration from the tsetse fly, which means that the cutting surface of the device rotates with its axis perpendicular to the drilling direction. The device is to be tested on Sawbones closed cell foam, that closely mimics the mechanical properties of human cancellous bone [23].

E. *Layout of this Report*

This report is structured in the following manner: Section II describes the process of schematically designing the cutting head, flexible transmission, and the actuation of the drilling device. In Section III, this schematic design is dimensioned and the prototypes are manufactured. Section IV consists of several proof-of-principle experiments, which were meant to evaluate the prototypes. Section V provides a discussion on the main results, limitations of this research, some aspects that need to be considered when scaling the drilling device, the extent to which the drilling device can be medically implemented, and possible directions for future research. Section VI concludes this report.

II. SCHEMATIC DESIGN OF THE VERTEBRAL DRILL

A. *Solution Direction*

The vertebral drill is intended to be a handheld device, so it can easily be implemented during spinal fusion surgery. The vertebral drill consists of three major components: The cutting tip, the flexible transmission, and the actuator. The cutting tip removes material from the workpiece with an abrasive surface. The actuator drives the cutting tip and serves as the handle for the user. The cutting tip and actuator are connected by a flexible transmission that serves two functions: 1) It constrains the cutting tip in certain directions, while allowing it to be flexible in a two-dimensional plane, and 2) it transmits the motion of the actuator to the cutting tip. The layout of the device is schematically shown in Figure 7.

The drilling device is meant as a substitute for the pedicle probe. The first step is to locate the entry point on the posterior side of the vertebra using anatomical landmarks. After the superficial cortex at this location is opened using a burr [24], the vertebral drill is inserted into the cancellous bone beneath it. The device drills through the pedicle and into the vertebral body, where it will continue along the cortical outer layer. After the curved tunnel has been made, an interpedicular bone anchor can be inserted.

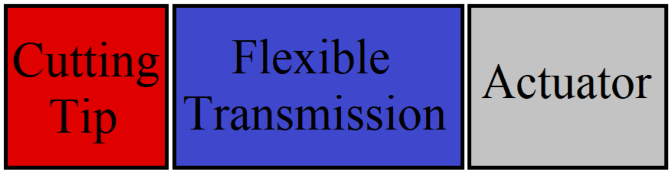

Figure 7: A schematic illustration of the layout of the device. From here on, the cutting tip is shown in red, and the flexible transmission is shown in blue.

B. Requirements

The tsetse fly-inspired vertebral drill should fulfil the following requirements:

- The device is capable of effectively drilling through cancellous bone. A surgeon can make a pilot hole using a pedicle probe in less than a minute [25]. The distance that needs to be drilled through the pedicle and vertebral body is in the range of 50 mm [26]. This results in a required drilling rate of around 1 mm/s to not prolong the operation significantly.
- The device does not increase the temperature of the surrounding tissue above 40˚C, in order to prevent necrosis of bone tissue [12].
- The device is flexible in one plane, with the option of being actively or passively steered.
- The outer diameter of the device should not exceed 10 mm. This shows if the vertebral drill can function in the intended order of magnitude. The limiting factor is the pedicle width, which is in the range of 10 mm for the lumbar vertebrae [9]. Later iterations may be scaled down for use in vertebrae with smaller pedicles.
- The device should be biocompatible, meaning that it does not leave harmful or toxic particles inside the body. This prototype may contain non-biocompatible materials, however it should be possible to make it biocompatible without drastically changing the design.

C. Cutting Tip Design

Cutting surface design

To design the cutting surface, a list was made of all theoretical surfaces, that rotate along an axis perpendicular to the drilling direction. This was done by starting with a one-dimensional case and expanding it from there into two and finally three dimensions. The overview of rotational drilling mechanisms is shown in Figure 8.

Two theoretical cases of a point contact in 1D can be identified: One in which the cutting point coincides with the centre of rotation (1), which essentially means that it does not move, and one in which the cutting point has a distance from it (2), which means that it describes a circular path. A point contact can only move with respect to the workpiece when it is placed outside its centre of rotation. Logically, the rotational cutting tool needs a nonzero thickness in order to make a cutting motion.

The point contact can be extended to a line contact in several ways. Firstly, by creating a line along its path, which results in a circular line contact (3). Because the line contact is moving through the workpiece, it can be extended in that direction. This results in an elongated line contact with a semi-circular tip, which has the shape of a slot (4). Lastly, the one-dimensional cutting point can be extended outside of the plane, which results in a single cutting edge (5).

The found two-dimensional contacts can be added to each other to create a three-dimensional cutting surface. The circular line contact (3) and the single cutting edge (5) together form a cylindrical cutting surface (6). Similar to the two-dimensional slot, this cylinder can be extended in the drilling direction, which results in a surface which resembles a belt (7). Another way of approaching a three-dimensional surface is by multiplying the found line contacts. Adding circular line contacts, each with a slightly rotated orientation, can create a spherical cutting surface (8). Note that the sphere does not rotate as one unit, instead each line segment rotates around its axis. The line contacts overlap each other in a way that resembles a ball of wool. Again, this structure can be extended in the drilling direction. This forms a slot that is rotated around its length axis (9).

It should be stated that only the surface contacts are considered to be implemented in the drilling device. The one- and two-dimensional cases are only used to construct these three-dimensional surfaces. Of these surfaces, the cylinder (6), the belt (7), and the rotated slot (9) can be used. The rotated circle (8) however, is an impractical design because the surfaces form a sealed sphere, this would make it nearly impossible to actuate.

Combining cutting surface and material

The cutting surfaces that were found in Figure 8 are decoupled from the cutting tool material. To combine a cutting surface and tool material, basic understanding of the mechanics of a cutting operation is required. The fundamentals of machining theory can be found in Appendix I. To find out which cutting tool materials may be used in the drilling device, an experiment was conducted in which a wide range of commercially available cutting tools was tested on polyurethane foam. This experiment is shown in Appendix II. In order to choose the most suitable combination between cutting surface and tool material, it is necessary to identify which of the tool materials, that were tested in Appendix II, are compatible with which surface. The cylindrical surface (6) can be used in combination with metal teeth or abrasive particles. The belt surface (7) and the last two surfaces (8) and (9) can also be used in combination with abrasive particles and would function similarly to belt grinding machines. The problem with using an abrasive surface that consists of bonded particles, is that it is not biocompatible, because these particles will wear off of the surface and stay behind in the vertebra. A solution for this could be to use biocompatible abrasive grains. Still, metal teeth are less susceptible to wear than abrasive particles, because they have fewer wear mechanisms [27]. So besides biocompatibility, choosing metal teeth over abrasive particles is beneficial for the lifespan of the tool. It can be concluded that out of the possible combinations of tool material and cutting surface, metal teeth on a cylindrical surface are best suitable for the drilling device.

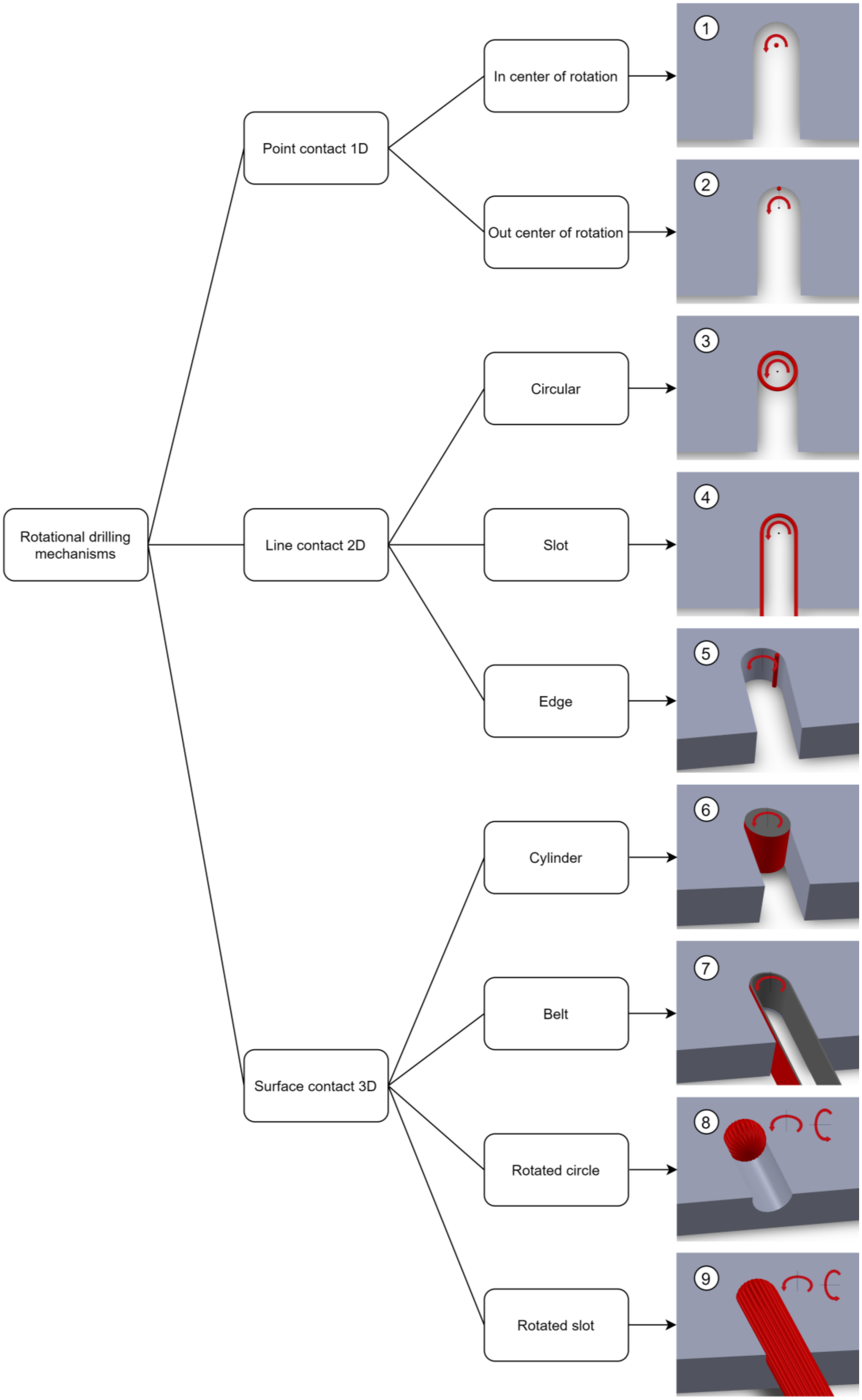

Figure 8: An overview of cutting surfaces that rotate along an axis perpendicular to the drilling direction. The cutting surfaces are indicated by their red colour and corresponding number and the workpiece is represented by a grey block.

Number of cutting surfaces

When using one rotating cutting surface, the cutting head might have the tendency to roll over the workpiece material instead of cutting it, because the friction force pushes it to the side. This is illustrated in Figure 9. The friction force is in this case the reaction force to the cutting force, as seen in Appendix I. Using multiple surfaces could eliminate this problem, when these surfaces are configured in such a way that the friction forces cancel each other out. The different configurations that were considered are shown, along with the friction forces they experience from the workpiece, in Figure 10.

The use of a single surface (a) would result in the least complicated design. There are two fundamentally different ways of adding extra surfaces: 1) adding an extra surface on the axis of rotation of the existing one, or 2) adding one with another axis of rotation. If two cylindrical surfaces are used next to each other on different axes (b), they can balance each other if they rotate in opposite directions. However, the diameter of the cylinders can only be half the length compared to using one axis, because the required maximum dimensions remain the same. The outer diameter of the device may not exceed 10 mm, which means that the two cylinders cannot be larger than 5 mm in diameter. This would greatly complicate the actuation of the cutting surfaces, which is why the use of a single axis is chosen.

If an extra surface is added on the same axis as the first one (c), it needs to rotate in the opposite direction of the existing surface in order to counteract the rolling tendency. However, the rotations in opposite directions would introduce a moment around the axis parallel to the drilling direction. This moment could cause the device to twist. Adding one more rotating surface could counteract this twisting moment. Using three surfaces with the same axis of rotation (d) can drill without twisting if the two surfaces on the outside rotate in the same direction, while the middle surface rotates in the opposite direction. Rolling is prevented by making the two outer cylinders together as wide as the middle one. Only when three surfaces are used is the device truly balanced. Another aspect to consider is that with each surface that is added, the actuation becomes progressively more complex and the device becomes thicker. This extra thickness is at the expense of flexibility. Also, friction is introduced between the counter-rotating surfaces, making the device less efficient. Small parts of workpiece material, blood and tissue can also get stuck in between the cylinders, which would further increase the friction. The advantages of using multiple surfaces do not seem to outweigh the complications, which is why the use of a single cylindrical surface is chosen.

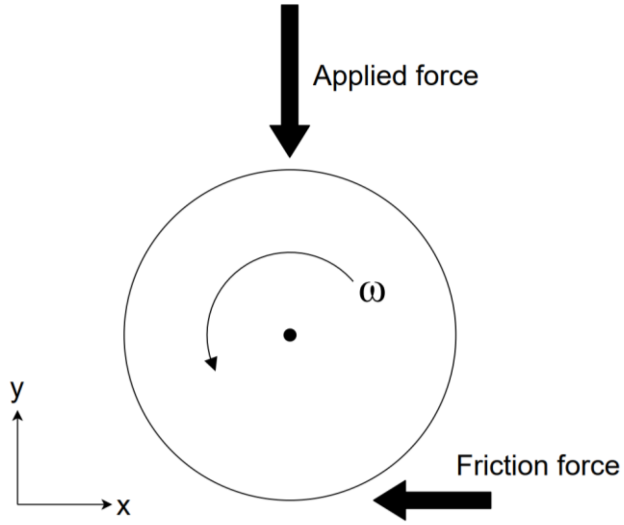

Figure 9: A free body diagram of a rotating cutting surface. The applied force is in the drilling direction, which is in the negative y-direction. With a counter clockwise cutting motion, this results in a friction force in the negative x-direction. The cutting surface will thus move downwards and to the left.

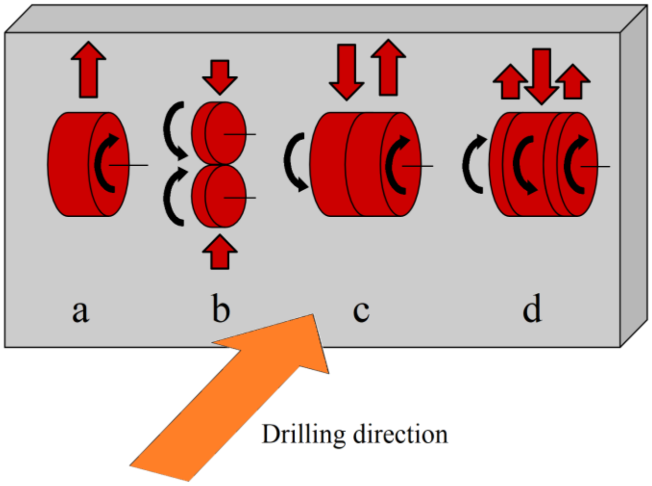

Figure 10: The different configurations that were considered. The red surfaces cut into the grey workpiece in the direction of the orange arrow. The rotations are shown with the black arrows, and the friction forces on the cutting surfaces are shown in red.

D. *Transmission*

Cutting head motion

The cylindrical cutting surface has been chosen, the next step is designing a flexible transmission that connects the cutting head to the actuator. Before this can be done, the motion of the cutting head needs to be defined. This could be either a continuous rotation, or an oscillating rotation. A continuous rotation is however not possible without introducing a part on or next to the cylinder that is not a cutting surface. For instance, the cylinder could be actuated by a belt or cable that loops around it, which would make it impossible to have cutting teeth on that part of the cylinder. The cylinder could also be actuated by an axle that protrudes from the side, which could be connected to gears or cables. Again, this addition would prevent the tool from drilling, because the protrusion would get stuck in the workpiece. In order to retain a complete cutting surface, the cylinder should be oscillating instead of continuously rotating. It is important to realise that due to the oscillating motion, the cutting head needs to be able to cut in both directions. This can be done by making the cutting teeth symmetrical.

Transmission design

The use of a cutter, with its axis of rotation perpendicular to the cutting direction, makes it possible to design the cutting mechanism in a two-dimensional plane. This allows the transmission to be flexible in the plane perpendicular to it. This principle is frequently used in two-dimensional paper pop up mechanisms, that are able to transmit motions within a page of a book [28]. The input of the transmission was chosen to be an oscillation, similar to the output. An oscillating actuator can be used to drive the device, so it is not necessary to convert a continuous rotation into an oscillation in the transmission.

The different mechanisms that were considered for transmitting an oscillation in a two-dimensional plane are shown in Figure 11. The schematic illustrations show the side plane of the transmission, with the input on the right and the output on the left with a red cutting surface. The input and output are connected by a grey shaft and blue transmitting elements, that are flexible in the top plane, so outside of the paper. A distinction was made between transmissions with translating and rotating elements. Two fundamentally different translating mechanisms are shown. The first one is a four bar linkage (A), in which the flexible shaft functions as the fixed link and the transmission functions as the intermediate link. To transmit the oscillation, the intermediate link needs to push and pull. Adding another intermediate link below the fixed link makes it possible to use elements that only have to push or pull (B). Two cables could for instance be used, these are elements that can only pull. When the two beams are used in a way that they only have to push, it means they do not have to be hinged to the cutting head.

The two rotational transmissions that are shown seem less feasible than the translating ones, mainly because they are more complex without added benefit over the translating mechanisms. Furthermore, this complexity only increases with the length of the transmission, which is not the case for the translating mechanisms. The transmission with a single rotating element (C), that functions as a partial gear, has the problem that its angle of rotation depends on the length of the tool, because it cannot protrude above or below the cutting head. This partial gear also needs to be flexible, because the transmission is required to bend. Using multiple rotating segments (D), eliminates the problem of the angle of rotation being dependent on the tool length, however it results in a highly complex transmission with many moving parts.

Of the four mechanisms shown in Figure 11, the translating mechanisms are best suited for the device, because they do not require rolling contacts, but simple hinges, and because the transmission does not become more complicated when the length of the device increases. For these reasons, the translating transmission mechanisms were explored further.

As stated before, using two intermediate links allows the transmitting beams to only push or pull. If two pushing elements are used, the two hinges at the cutting head are no longer necessary, because the fixed link is still hinged at the cutting head and provides the necessary pulling force. This can be seen in Figure 12a. However, it is also possible to use this idea the other way around. If the two intermediate links are hinged at the cutting head, they are able to both push and pull, which means that the fixed link becomes redundant. The fixed link and two intermediate links can thus be integrated into a transmission with two beams. This principle can be seen in Figure 12b. The advantage of integrating the two intermediate links with the fixed link is that only two beams are needed for the transmission, which minimises the number of parts and allows for a more flexible device.

The transmission with two pushing and pulling beams seems to be similar to the four bar linkage of Figure 11. The difference is that, in the four bar linkage, one of the beams is hinged in the centre of the cutting head, where in the transmission of

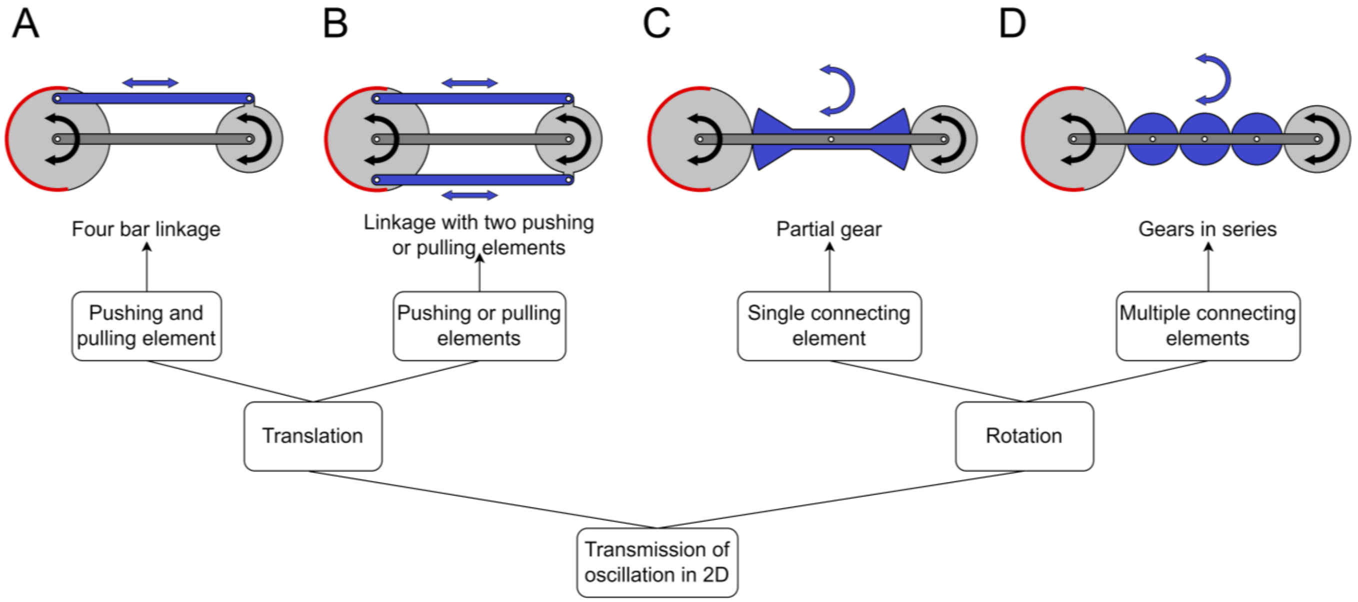

Figure 11: A structured overview of different mechanisms that are used to transmit an oscillation in a two-dimensional plane.

Figure 12b, the two beams are connected at the top and bottom of the cutting head. This means that the distance between the hinges of the transmission of Figure 12b is larger. This increases the moment arm of the two beams, which lowers the force on the hinges. The increased distance between the hinges also makes the device easier to build on a smaller scale. For these reasons, the transmission with two pushing and pulling elements was chosen.

At this point, it is important to mention that the beams of the transmission will not be as small as they are schematically shown in Figure 12b, instead they will be approximately as high as the diameter of the cutting head, as shown in Figure 12c. This is because they need to be axially stiff, while being flexible outside of the plane of the paper. This can only be done by increasing their height, because increasing the thickness would decrease their flexibility. Increasing the height of the beams to the outer dimensions of the device implies that the beams cannot be placed directly on top of each other, instead they have to be placed side by side.

Flexibility

Flexibility of the transmission can be either discrete or distributed. Discrete flexibility implies that the transmission consists of a multitude of rigid elements that are connected in such a way that allows for movement between those elements. Discrete flexibility has the advantage that the material itself does not need to be flexible, the downside however, is the added complexity due to the number of components. This is especially problematic on a small scale. Distributed flexibility implies that the transmission consists of flexible elements that span the entire length of the device. This type of flexibility was chosen because it greatly simplifies the manufacturing process.

To design the flexible transmission, it is important to identify the degrees of freedom of the cutting head that are required, and those that need to be constrained. It needs to be stated that the cutting motion of the device is not taken into account in this section. Only the movements of the cutting head due to flexibility of the transmission are considered. Flexibility in a two-dimensional plane is required, while remaining axially stiff. This means that the allowable degrees of freedom (DOF) are rotation in the top plane, jaw, and sideways translation. Figure 13 clearly shows the steps that are taken to ensure the other DOF are constrained.

When the cutting head is free to move in three dimensions, it has 6 DOF. This is shown in Figure 13a. A flexible, but axially stiff rod can be added, that constrains the translations to the front and back. This enables the device to handle the applied force when cutting. Figure 13b shows the rod and the remaining 5 DOF. The cutting head is still able to move up and down. Expanding the rod into a vertical plane, or leaf spring, constrains two other DOF: pitch, and translations up and down. The remaining 3 DOF are shown in Figure 13c. The final DOF that should be constrained is rotation in the front plane, roll. Rolling of the cutting head is not expected to be a problem, because this is caused by twist in the transmission. This will only occur when the cutting head is asymmetrically loaded, which could for instance happen when the workpiece material is harder on one side of the cutting head than the other, or when the tool is only cutting on one side. The twisting moment is expected to be negligible, because the moment arm is half of the cutting head thickness, which is relatively small to begin with. If, in practice, this does prove to be a problem, it could be solved without the need to add an additional element to the transmission. Instead, the applied force could be decreased, because this results in a lower cutting force, which in its turn lessens the twisting of the cutting head. For simplicity, the first iteration of the transmission will be constrained by leaf springs as in Figure 13c, with the possibility of further improvement. Rolling of the cutting head could be eliminated by adding a helix to the leaf spring. A helix is able to constrain twist without reducing flexibility in the desired bending direction [29]. The addition of the helix and the remaining 2 DOF are shown in Figure 13d. The problem with adding a helical shape to the transmission is the complexity in manufacturing. The helix could be 3D printed, although this would require the printed material to be biocompatible, flexible, and tough enough to withstand the applied forces during cutting. Another option would be to use a compression spring in combination with the leaf spring of Figure 13c, but this would require the two components to be rigidly connected.

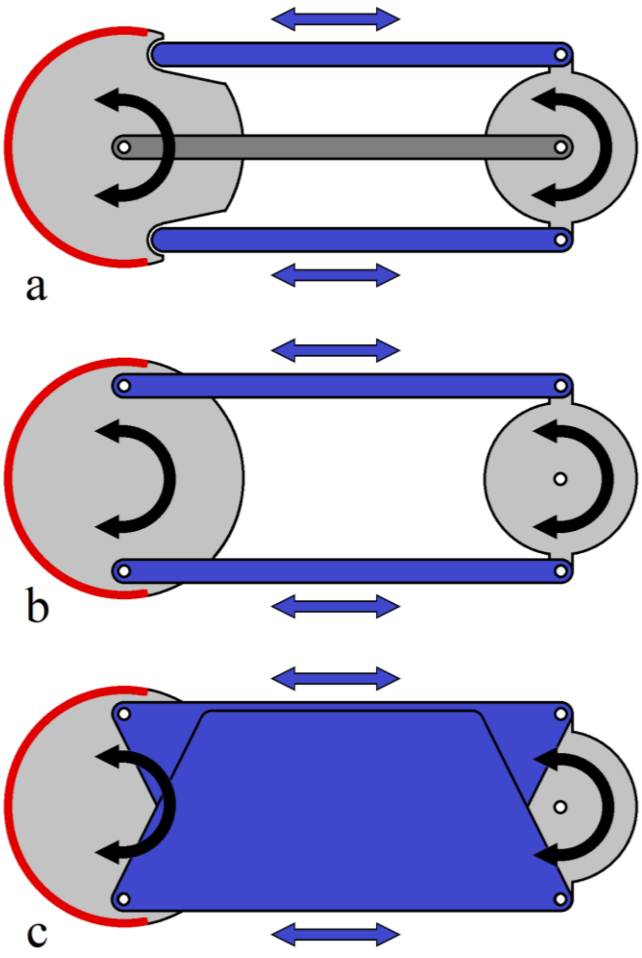

Figure 12: Three versions of linkages with two pushing or pulling elements. a) The two beams are used to only push, which eliminates the need for hinges at the cutting head. b) The two linkages are used to both push and pull, which eliminates the need for the fixed beam. c) The same mechanism as shown in b, but with reinforced beams to handle the cutting forces.

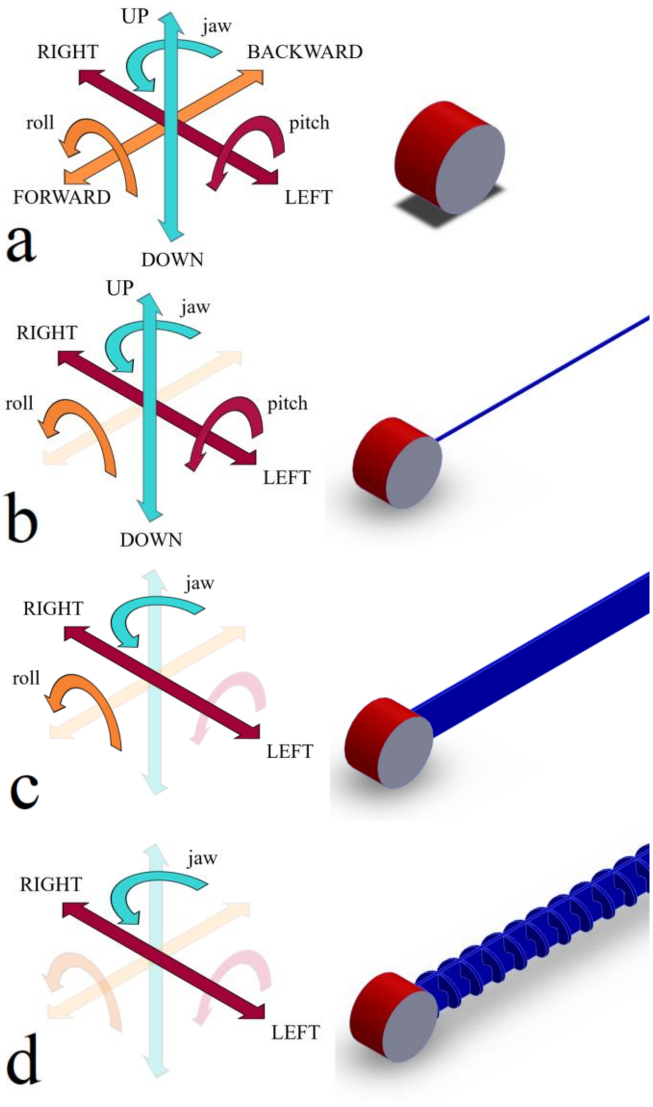

Figure 13: The different elements that comprise the flexible transmission, along with their corresponding degrees of freedom. Each element that is added constrains one or more movements.

Connection to the cutting head

After the pushing and pulling mechanism, and the type of flexible elements were chosen for the transmission, the way how this transmission is connected to the cutting head and actuator could be defined. Keeping in mind that the two transmitting beams are placed side by side, they can be connected to the cutting head in two different ways: on the inside, or on the outside of the cutting head, as shown in Figure 14a and 14b, respectively. Connecting the beams on the inside of the cutting head has the advantage that the pushing and pulling forces on the hinges are as close together as possible in the top plane. This means that the generated moment is mostly around the intended axis of rotation, which is the dotted line in Figure 14. Connecting the beams on the outside would place the pushing and pulling forces further apart. Increasing the distance between the pushing and pulling forces introduces an unwanted moment in the top plane, which would move the cutting head from side to side.

Connecting the beams on the outside also has the disadvantage that the beams have to be bent towards each other, so that the transmission remains flexible in the top plane. This would make the device more difficult to build. When connecting the beams on the inside of the cutting head, bending them is not necessary.

The final point to consider is the overall width of the cutting head. Placing the beams on the inside implies that the cross section in the top plane has four layers: Two layers of the cutting head on the outside, and two layers of transmission beams on the inside. When placing the beams on the outside, only three layers are needed: Two layers of transmitting beams on the outside and one layer of the cutting head on the inside. So in theory, a thinner device can be made when the transmission is connected to the outside. In this case however, the device is not required to be as thin as possible. The only dimensional constraint is that of the cutting head diameter. This requirement is met as long as the cutting head is thinner than 10 mm, which can be accomplished with the configuration shown in Figure 14a. Weighing the pros and cons related to the generated moment, ease of manufacturing, and total width of the device, the transmission was chosen to be connected to the inside of the cutting head.

Having the two oscillating beams placed side by side has an effect on the position of the cutting head, when the transmission is bent. This effect becomes evident when the top view is considered, as in Figure 14. Bending the device causes the two beams to slide over each other. Because they have a nonzero thickness, the result is that one beam will protrude. This is the beam that is on the side to which the device is bent. Because one beam sticks out further than the other, the cutting head will be slightly offset. Depending on which beam is connected to the top and bottom of the cutting head, and in which direction the device is bent, the cutting head will rotate up or down. The magnitude of this rotation depends on how far the device is bent, and on the thickness of the translating beams. This unwanted rotation needs to be taken into account when the angle of oscillation is defined, otherwise there may be a chance that the device is not able to make a full cutting motion in a bent state.

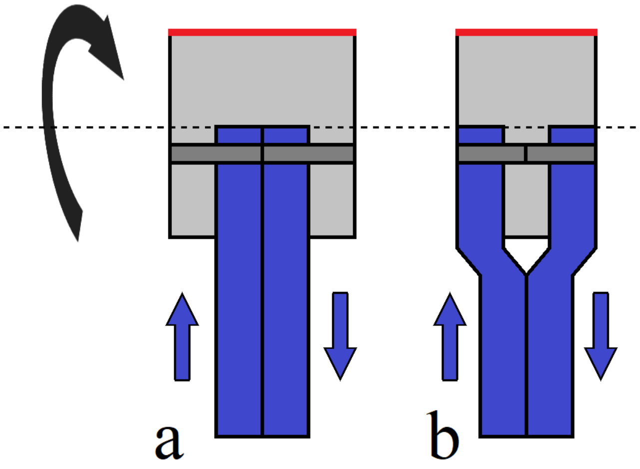

Figure 14: Top view of the two ways of connecting the transmission to the cutting head. a) Shows the connection on the inside, and b) on the outside.

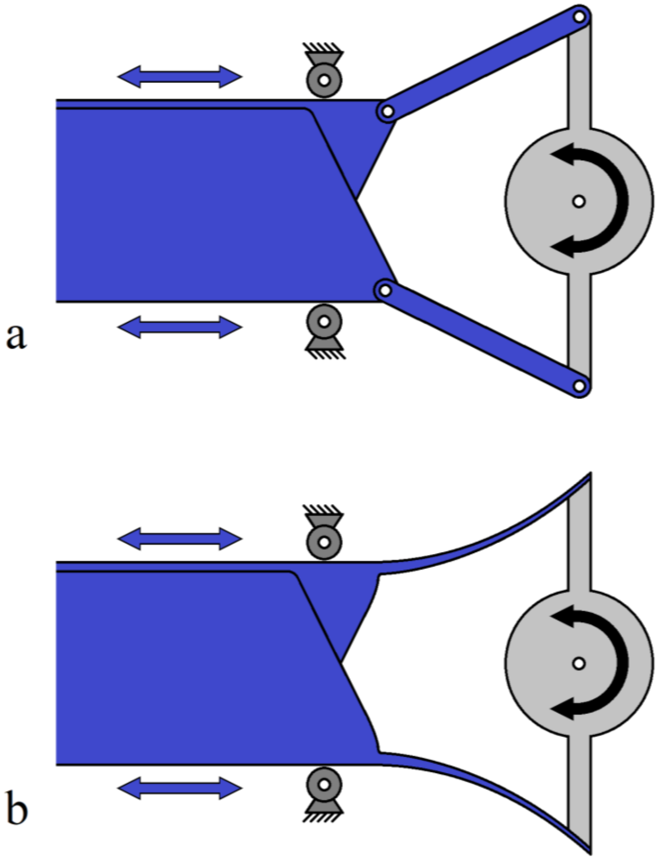

Figure 15: The connection of the extended oscillating input beam to the transmission. a) Shows a connection with hinges, while b) shows the same connection in a compliant form. The constraint on the transmission is indicated by the two rollers above and below the transmitting beams.

Connection to oscillating input

For the sake of simplicity, the device is designed as an add-on to an existing oscillating power tool, which means that the actuation was not designed from the ground up. The design challenge is connecting the two translating beams to the oscillating input. In the previous Figures 11 and 12, the transmissions were shown with a 1:1 ratio, meaning that the distance between the hinges of the cutting head are equal to those of the oscillating input. This can only work if the input has the oscillation angle that is needed at the tip. In reality, oscillating power tools are used in combination with cutting attachments that are approximately an order of magnitude larger than the bone drilling device will be, think for instance of the blade of an oscillating cast saw. Because the bone drilling device is smaller in diameter, it needs a larger angle of oscillation at the cutting tip for the same travel of the cutting teeth. This means that the oscillation angle of the input needs to be multiplied in the transmission.

Figure 15a shows an extended oscillating input, that is connected to the transmission by means of four hinges. These additional hinges are needed when rigid beams are used. A way of simplifying this design is to avoid the use of hinges by making the connection to the oscillating input flexible. Flexible beams can in this case be used instead of hinges, because the displacements are relatively small. This principle can be seen in Figure 15b, and can be easily integrated into the transmission, because the two reciprocating beams are already required to be flexible. It is important to note however that the device, as shown in Figures 11 and 12, needs to be able to bend out of the plane, while the connection to the oscillating input needs to bend within the plane. This transition in flexibility can, for instance, be made by folding the thin flexible material around its length axis. Because of the reduction in complexity, the flexible connection to the oscillating input was chosen for the device.

The final aspect to consider are the degrees of freedom of the transmission with respect to the oscillating input. Without some form of guidance, the device has two degrees of freedom: The intended movement, which is the two transmitting beams reciprocating horizontally, and an unintended movement, which is the whole device rotating up and down along with the input. A guiding mechanism is thus necessary in order to keep the transmission in its horizontal position, this is shown in Figure 15. The two rollers above and below the transmission indicate a constraint in the vertical direction, but allow for horizontal movement.

Buckling prevention

The final aspect of the flexible transmission to consider is buckling. Failure due to buckling can occur in two different ways. The pushing beam can buckle due to the applied force of the actuator, and both beams can buckle together due to the load applied by the user. Buckling due to the actuating forces can be prevented by keeping the leaf springs connected so they can slide parallel to each other.

One could think of many different ways of connecting the leaf springs side by side, as shown in Figure 16a. The first two options are connections that use folded tabs, the advantage of which is that no additional parts are needed. The connection as shown in Figure 16b has a series of tabs that originate from the left beam, and are folded over the right spring at the top and bottom. The downside of this option is manufacturing. The tabs can never be folded in such a way that they lie flat on the right beam, this is because of the spring back effect. The tabs on the leaf spring need to be bent further than the desired angle to account for spring back. This is not possible however, because this would require the material to move through itself.

The option shown in Figure 16c is essentially the same, but the tab is rotated a quarter turn. Bending the tab to the desired shape is possible in this case, because it leaves a gap in the left leaf spring. This means that there is room to bend the tab in both directions. The downside of this option is that the material that is used for the tab no longer supports the forces from the actuator. This means that the effective height of the leaf spring is drastically decreased.

The last two options are connections that use additional parts to keep the two leaf springs together. Figure 16d shows the use of a sleeve around the two beams. Even though this introduces an additional part, it would be easy to manufacture when for instance a shrink sleeve is used. There are two reasons why this option was not chosen: Adding a sleeve around the two leaf springs introduces additional layers that decrease the flexibility of the transmission. The second reason is durability. The sleeve is constantly subjected to friction from the two oscillating beams, which decreases its lifespan.

The final option is the use of a pin in the left spring, that is constrained by a slot in the right spring. This connection is shown in Figure 16e. While this is arguably the most complex option in terms of manufacturing, it is able to connect the two beams without compromising the strength, durability, and flexibility of the transmission. For these reasons, the connection using a pin and slot was chosen for the transmission.

Connecting the two beams prevents buckling due to the actuation, however as stated before, the whole transmission could buckle due to the applied load. It needs to be stated that this is only a problem when the device is outside of the workpiece material, because when it is drilling into the workpiece, it is constrained by its own tunnel. Once again, the solution for this problem is found in nature. Insects encounter the same problem when piercing a substrate, and have two solutions that can be applied to the vertebral drilling device: The first option is to decrease the unsupported length of the device by simply holding it. This is possible because the oscillation of the two beams is relatively small. The operator could hold the actuator with one hand, and the transmission with the other. The second option is the use of a tube that guides the device when it is outside of the workpiece material. The tube needs to be telescopic because the unsupported length of the transmission decreases, as the device advances into the workpiece [21]. For the first prototype, it was chosen to hold the transmission to prevent buckling due to the applied load. If this proves to be impractical, the telescopic guiding tube could be added without the need to make adjustments to the rest of the device.

E. Wall Guidance

While the goal of this research is to design a flexible drilling device, with the possibility of being made steerable, it is important to address the different types of steerability. Verdult [1] describes two main categories of steerable devices: actively, or passively steered. Active steerability implies that the direction of the tool is determined by the operator, while the device is being used. Passive steerability can fall in one of two categories: tool dependent or material dependent steerability. These types depend on the properties of the device, and on the properties of the workpiece material, respectively, while active steerability depends on the operator. Workpiece material dependent steerability does not require additional parts or features on the drilling device.

An example of material dependent steerability is the concept of wall guidance [1]. As seen in Section I.A, the porous inner material of the vertebrae is encased by a harder outer layer, the cortical wall. Wall guidance assumes that the drilling device follows the path of least resistance. When the drilling device comes into contact with the cortical wall, while it is cutting through the cancellous bone inside it, it could be deflected by this wall because of the difference in material properties. In this way, the drilling device is able to automatically follow the cortical outer layer of the vertebral body. The extent to which this could work depends on the flexibility of the transmission, the angle at which the cutting head comes into contact with the

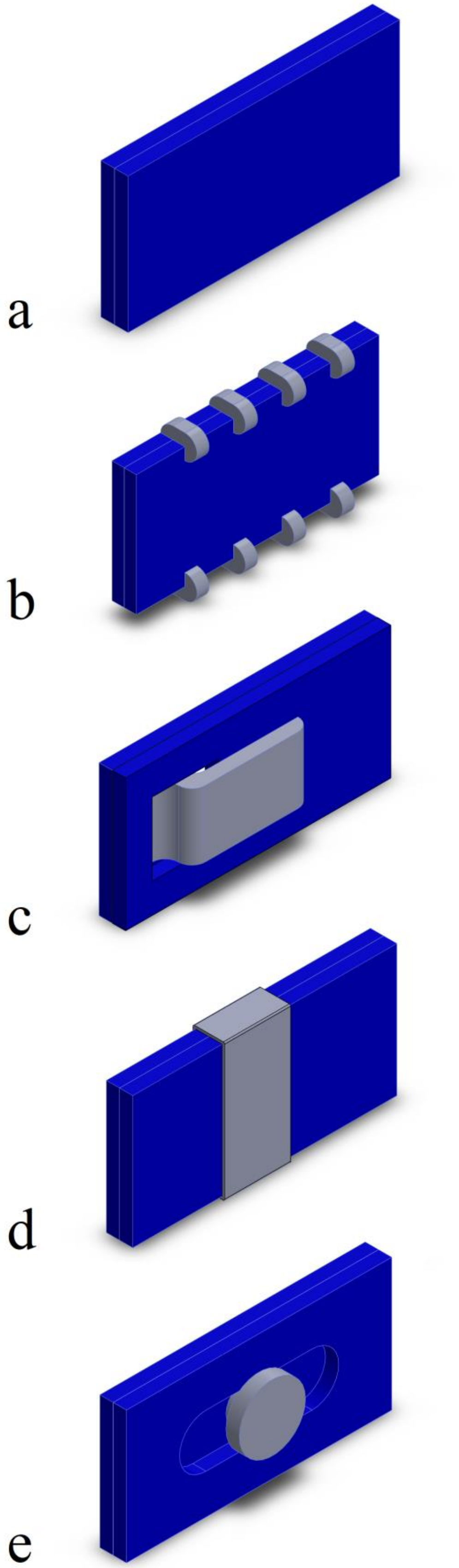

Figure 16: The four concepts for buckling prevention that were considered. The two transmitting beams are partially shown in blue, while the added parts are shown in grey.

cortical wall, and the difference in mechanical properties between the cancellous bone and the cortical outer layer. The focus of this research is to create a flexible drilling device, that is able to cut effectively through cancellous bone. However, the design as it is could be passively steered by means of wall guidance.

F. Schematic Design

The solutions found in Sections II.C and II.D are combined into the schematic design shown in Figure 17. The oscillating cutting head is connected to the two blue translating leaf springs with two hinge pins. The transmission will be mounted at the inside of the cutting head, however it is shown on the outside in Figure 17 for the sake of clarity. The two beams are connected to each other by the two grey pins, that prevent buckling due to the cutting force. One pin is in theory enough to constrain all unwanted relative movement between the two beams, because they are both connected to the cutting head. To prevent buckling however, more pins may be needed depending on the tool length. The pins are connected to the rear beam, and the slot in the front beam allows for relative movement between the two. Because the vertical distance between the two hinge pins of the cutting head changes as the head rotates up and down, the slots in the front beam of the transmission need to be curved. The radius of this curvature is equal to the distance between the hinge pins. The transmitting beams are compliantly connected to the oscillating input, which eliminates the need for more hinges. The constraint on the transmission is indicated by the two rollers above and below the transmitting beams. This constraint is connected to the stationary part of the actuator, which also serves as the handle for the operator. The oscillating actuator is shown as a grey block in Figure 17.

III. PROTOTYPE DIMENSIONING AND MANUFACTURING

A. Cutting Head

The chosen Dremel cutting tool

The 9933 Dremel bit with structured tungsten carbide teeth was used, because it performed well in the test on polyurethane, which can be seen in Appendix II, and because the teeth are not angled towards one side. This means that the teeth are able to cut in both directions, which is necessary in an oscillating cutting tool. The structured tungsten carbide bit has characteristics of both a cutting and a grinding tool. The particles are arranged, or structured, perpendicularly to the axis of rotation. The orientation of the particles is thus not random, unlike in a grinding tool. However, the particles do have a negative rake angle and lack relief angles, which is typical for a grinding tool [30]. Attritious wear and grain fractures are highly unlikely due to the high hardness and toughness of the tungsten carbide particles with respect to the workpiece material. This tool is, unlike a grinding tool, not designed to lose particles by bond fractures, instead the tungsten teeth are brazed onto the steel central shaft. A close-up image of the used Dremel cutting tool is shown in Figure 18. A 4 mm slice of this tool was used as the cutting head. The slot for the transmission was cut to the centre line, because cutting further would decrease the effective diameter of the tool. Furthermore, the slot was made wider near the teeth of the cutting head, so they do not cut into the leaf springs when the device is bent.

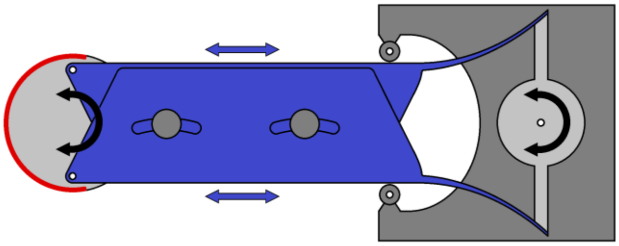

Figure 17: A schematic illustration of the drilling device. This Figure combines the solutions found in Sections II.C and II.D.

Dimensional constraints

The dimensions of the Dremel bit determine the maximum distance between the two hinges. The maximum distance is desired, because this gives the lowest possible force on the hinges. The tool is 7.9 mm in diameter including the teeth, and 6 mm without. The hinges need to be placed slightly off centre, because the slot is cut up to the centre line. This allows the 1 mm thick hinge pins to be placed 4 mm apart. The device is able to cut effectively only if the oscillation of the cutting head is larger than the distance between the teeth. The teeth are roughly 1 mm apart, but to ensure the teeth will cut the along the whole surface, 2 mm of travel is chosen. For 2 mm of travel along the cutting surface, a rotation of 30° is necessary, this means 15° to either side from the neutral position. The formula that is used to calculate this value is shown in Appendix III. A model of the cutting head connected to the two leaf springs that comprise the transmission is shown in Figure 19. As stated before, the curved slots by which the leaf springs are connected have a radius equal to the distance between the hinge pins of the cutting head, which is 4 mm.

B. Oscillating Input

The chosen oscillating actuator

The oscillating input is provided by the Black and Decker MT300KA, which has an oscillation of 2.8°, a 300 W motor, a maximum cutting speed of 22,000 rpm, and 6 mm internal threads to which the device can be connected [31].

Figure 18: The Dremel 9933 tungsten carbide cutter that was used for the cutting head.

Figure 19: A model of the cutting head and the two leaf springs. a) A side view showing the two hinge pins in the cutting head, and the curved slot in the leaf springs. b) A top view showing the slot in which the leaf springs are mounted. Note that the slot widens at the outside of the cutting head, which ensures the teeth do not damage the springs when the device is bent.

Transmission ratio

An oscillation of 30° is necessary at the cutting head, however the chosen input has an oscillation of only 2.8°. The oscillation from the input should thus be amplified. One way to do this is to make the arm connected to the oscillating input longer than the 4 mm between the pins of the cutting head. The minimally necessary arm length was calculated to be 41 mm. The calculations that led to this value is shown in Appendix III.

C. Transmission

Number of pins for buckling prevention

The number of connecting pins in the transmission is a critical aspect of the design, because the leaf springs are not able to transmit the cutting forces if they are not sufficiently supported. To constrain the leaf springs to their desired motion, only one pin is needed, because the cutting head also acts as a connecting element. These two points of connection constrain the leaf springs to remain parallel to each other. However, additional pins may be needed to account for buckling of the individual leaf springs. The number of pins to prevent buckling is dependent on the thickness of the leaf springs. Leaf spring thickness is a compromise between axial stiffness and thus the ability to transmit cutting forces, and flexibility, which allows the drilling device to be more easily steered. A leaf spring thickness of 0.2 mm was chosen for the prototype, with a width of 6 mm, which corresponds to the cutting head diameter excluding the teeth. The leaf springs are made of stainless steel 1.4310, also known as 301, which has a Young's modulus of approximately 190 GPa [32]. The first step in calculating the necessary number of pins for buckling prevention, is to determine the applied force on each leaf spring. The force on the leaf springs is calculated in the hypothetical case in which the cutting head is fixed. This is a worst case scenario which could occur when the device gets jammed into the workpiece. The maximum allowable distance between the leaf spring pins is calculated to be 39 mm. This calculation is shown in Appendix III. A leaf spring length of 120 mm was chosen, with three pins placed 38 mm apart. A render of the cutting head, leaf springs and the arm, that is to be connected to the oscillating input, is shown in Figure 20. The 90° folds in the leaf springs are made 10 mm long, leaving 110 mm of flexible transmission.

Rotation of cutting head due to bending

Bending the transmission of the device will cause the cutting head to rotate. This offset can be problematic if it exceeds the angular displacement of the cutting head, which is 15° from the neutral position. In this case, the slot in the cutting head would face the workpiece, which means that the device is no longer capable of cutting along its whole frontal surface. To ensure that bending the transmission does not hinder the cutting capabilities of the device, the offset of the cutting head was calculated in case of a 90° bend. The resulting rotation of the cutting head was calculated to be approximately 4.5°. Bending of the device should not reduce its cutting capabilities, because the offset does not exceed the angular displacement of the cutting head. Appendix III shows the corresponding calculations.

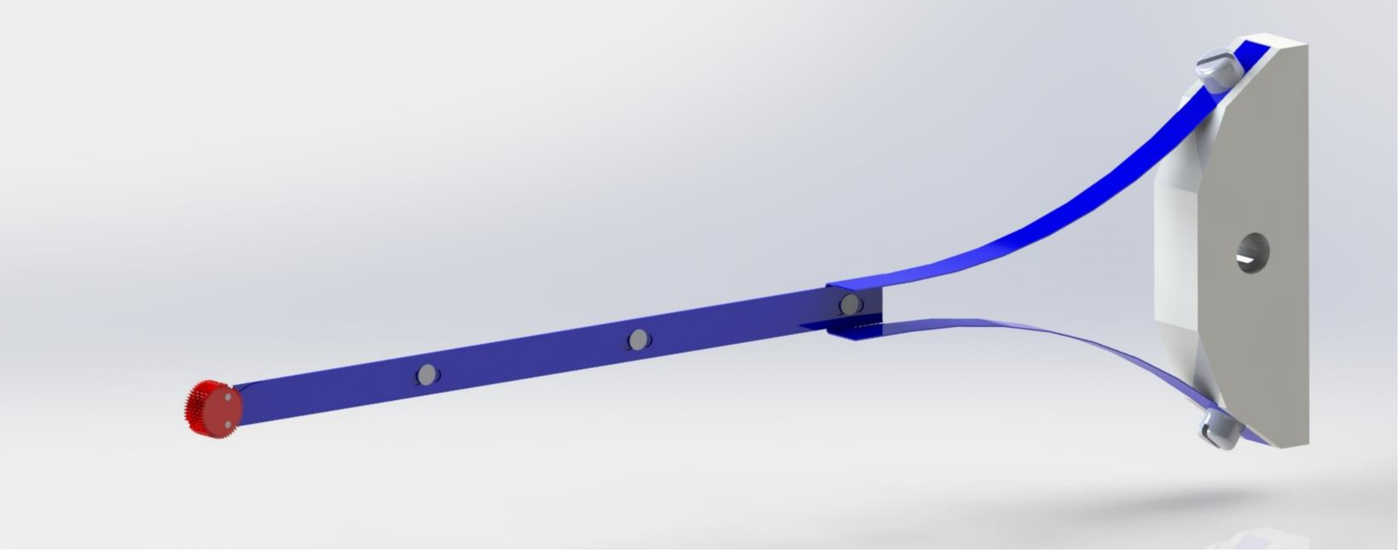

Figure 20: A render of the cutting head (red), flexible transmission with its three pins (blue), and the oscillating input (light grey) of the vertebral drilling device.

D. Guidance

To constrain the flexible transmission to its desired movements, a guiding part is necessary near the oscillating input. Without guidance, the whole device would oscillate around the axis of the input, and the parts of the leaf springs that are connected to the oscillating input could buckle instead of transmitting a linear motion. To counter these problems, the part as shown in Figure 21 was designed. The bent sections of the leaf springs do not travel along the same path throughout their oscillation. Even though this difference is less than a millimetre, the slots in the guiding part were designed taking this effect into account. The dimensions of the slots were determined by the extreme positions of the leaf springs, and 0.5 mm clearance was added on each side to ensure smooth oscillation. A total of 1 mm of clearance may seem excessive for a part of 0.2 mm in thickness. Keeping in mind, however, that the guiding part would be 3D printed, extra clearance is needed because the filament is still somewhat flexible when printed, resulting in a thinner slot. The exact amount of shrinkage is hard to predict, because it depends on the shape of the slot, print speed, print temperature and filament material. Figure 22 shows the cover that keeps the leaf springs in the slots of the guiding part.

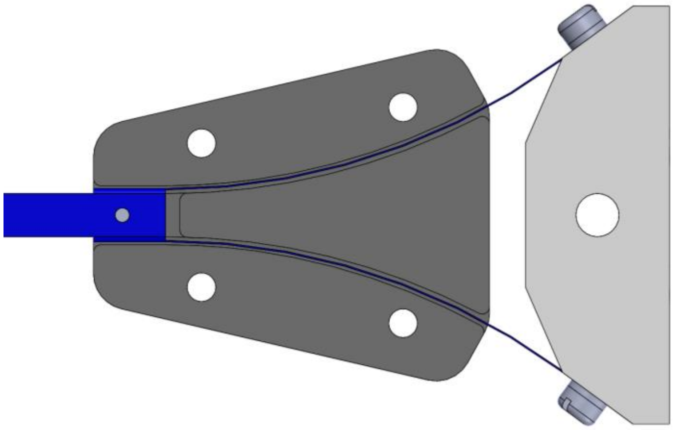

Figure 21: A top view of the flexible transmission with the guiding part (dark grey).

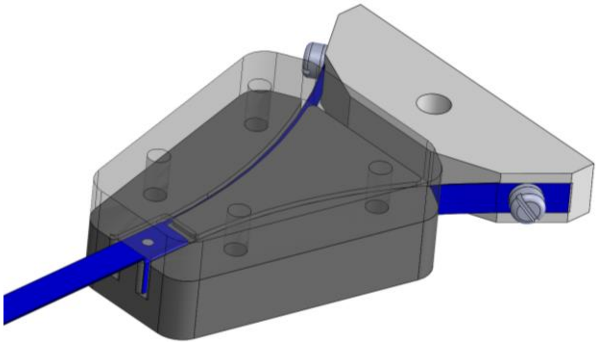

Figure 22: The leaf springs of the flexible transmission (blue) are kept in place in the slots of the guiding part (dark grey) by a covering part, which is shown here transparently.

E. Manufacturing and Assembly

The final design of the prototype of the vertebral drilling device is shown in Figure 23, and consists of all the previously mentioned components. Table 1 provides a brief overview of the chosen material and manufacturing process of each component. The teeth of the cutting head are made of tungsten carbide, which requires the part to be cut by means of wire electrical discharge machining (EDM). However, the centre of the cutting bit consists of steel, so the holes for the cutting head pins could be drilled on the drill press. The leaf springs and oscillating arm were also cut using wire EDM, not because the material requires it to, but because this was the most convenient available method to precisely create these parts from the CAD drawings. The slots in the aluminium oscillating arm, which accept the ends of the leaf springs, were milled in, after the outline of the part had been cut. Two holes were drilled and tapped to accept the M3 bolts that secure the leaf springs to the oscillating arm. The two guiding parts were printed on an Ultimaker 3. From the available filaments, PETG was chosen over PLA because of the increased strength and heat resistance. The holes in the guiding parts were printed slightly too narrow to accept the M4 bolts that were used, so they had to be drilled to 4 mm on the drill press. The pins in the cutting head and the transmission were turned on the lathe from tool steel, and riveted into position. Figures 24 to 26 show the first prototype of the vertebral drilling device.

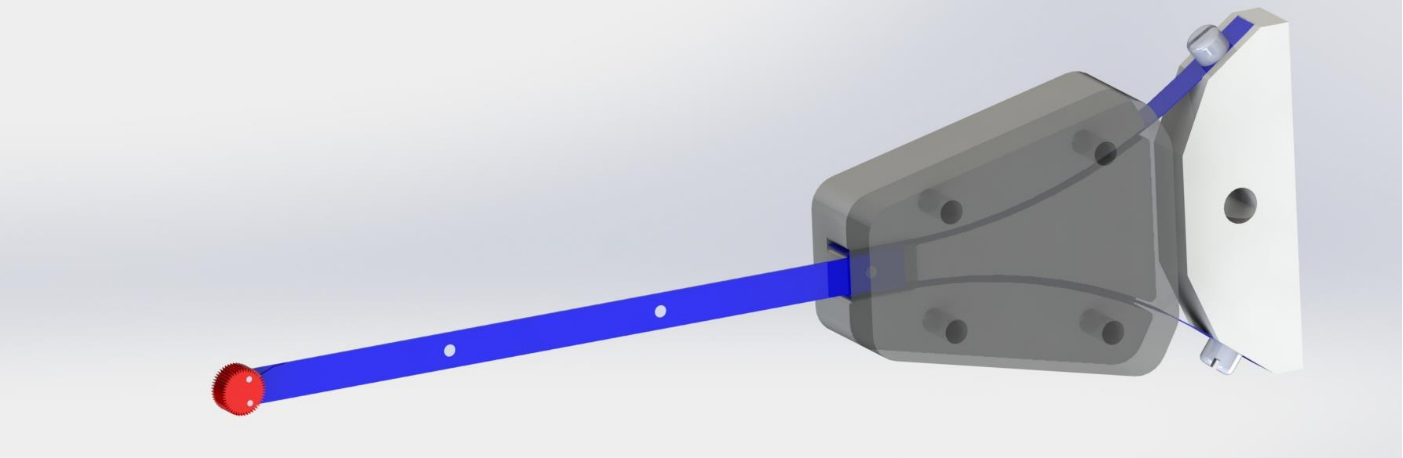

Figure 23: A render of the final design of the vertebral drilling device. The device consists of four major components: The cutting head (red), the flexible transmission (blue), the guiding block (dark grey), and the oscillating input (light grey).

Table 1: An overview of the major components that comprise the prototype, their material, and method of manufacturing.

Part	***Material***	***Manufacturing***
Cutting head	*Tungsten carbide*	*Wire EDM*
Cutting head pins	*Tool steel*	*Lathe*
Leaf springs	*Spring steel*	*Wire EDM*
Transmission pins	*Tool steel*	*Lathe*
Guiding parts	*PETG*	*3D printed*
Oscillating arm	*Aluminium*	*Wire EDM / mill*

Figure 24: The prototype of the vertebral drilling device without the guiding parts. This is the realisation of the render shown in Figure 20.

Figure 25: A closeup of the cutting head with a match stick as a reference. Note that the pins in the cutting head are visible.

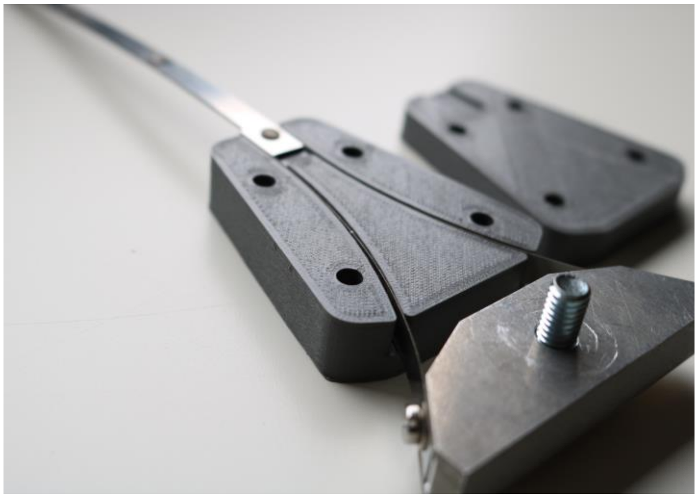

Figure 26: A closeup of the 3D printed guiding parts containing the flexible transmission.

The prototype is connected to the Black and Decker MT300KA in two ways: The oscillating arm is fastened to the output of the machine by an M6 bolt, and the guiding parts are connected to a stationary part of the machine by means of two aluminium brackets. Figure 27 shows the complete device, including the oscillating input.

F. *Second Iteration*

A second iteration of the prototype was made, because the first one broke down during testing before all data were collected. However, some of the results that were found with the first prototype could be used and are presented in Section IV. The first prototype failed at the connection between the leaf springs and the cutting head. A detailed description of how and why this connection failed, as well as the improvements that were made are shown in Appendix IV. To reinforce the transmission, the leaf spring thickness was increased from 0.2 to 0.3 mm. The teeth on the cutting head did not show any signs of wear, so it was not necessary to replace it. However, the slot in the cutting head had to be modified to facilitate the new leaf springs. Even though the leaf spring thickness was increased, the same guiding block could be used. The clearance in the slots of the guiding block was enough for the new leaf springs to slide in without jamming. The oscillating arm could also be reused, because the height of the springs was not changed. The new leaf springs could be easily mounted into the rest of the prototype, as they are only connected by the two screws in the oscillating arm. The rear ends of the leaf springs can be inserted into the front end of the guiding block, so there is no need to take it apart. The second iteration of the prototype is shown in Figure 28. The CAD drawings of the second prototype are shown in Appendix V.

Figure 27: The complete prototype of the vertebral drilling device, including the oscillating actuator.

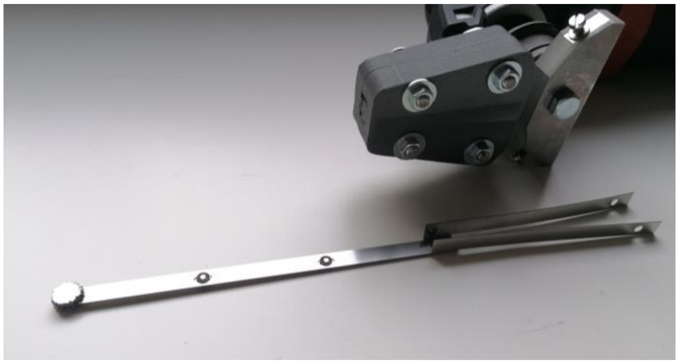

Figure 28: The second iteration of the prototype, with 0.3 mm thick leaf springs.

IV. PROOF-OF-PRINCIPLE EXPERIMENTS

A. Experiment 1: Static deflection

Goal and hypothesis

The goal of this experiment was to discover how the magnitude of a transverse applied force relates to deflection of the cutting tip. This experiment was done with both prototypes, (0.2 mm and 0.3 mm thick leaf springs). We hypothesised that the difference in stiffness should be proportional to the difference in the bending moment of inertia of the two transmissions. Because the thickness of the second prototype is increased by 50%, we expect the necessary applied force to be $1.5^3 \approx 3.4$ times as high to result in the same deflection.

Dependent and independent variables

The dependent variable was the radially applied force. The independent variables were the deflection, which was varied from 0 to 50 mm in steps of 5 mm, and the leaf spring thicknesses, which were 0.2 and 0.3 mm.

Experimental setup

The prototype was clamped in at the base of the transmission and placed upon graph paper, with a 1x1 millimetre square grit. A FUTEK 1 lb load cell, which was stable up to two digits after the decimal, was used to deflect the tip of the drilling device up to a certain deflection. During the experiment, the load cell was held horizontally, so it was not rotated along with the cutting head, as seen in Figure 29.

Experimental procedure

The LabVIEW file was turned on so the measurements from the load cell could be noted. Holding the load cell on its side introduced an offset in the measurement. Compensations were made for this offset in the LabVIEW file before proceeding. Both prototypes were tested three times from 0 to 50 mm in 11 steps, so the following sequence was repeated 66 times in total:

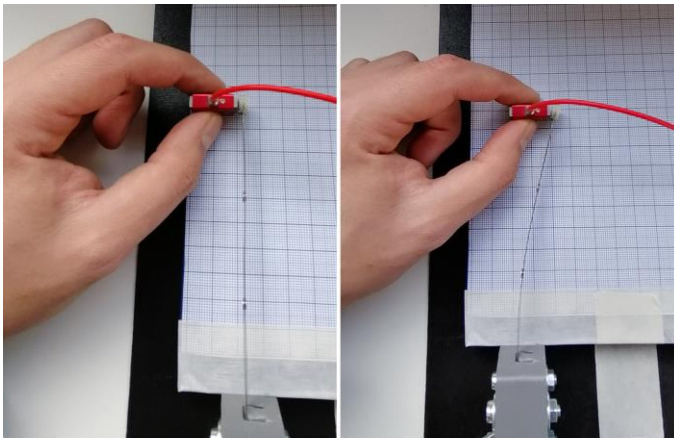
Figure 29: The experimental setup of the deflection test. The prototype starts in its neutral position (left), and is pushed by the load cell up to the desired deflection (right).

1) Starting from the neutral position, the cutting tip of the prototype was pushed up to the desired deflection with the load cell.
2) The measured force was noted.
3) After each deflection, the leaf springs were let go to their neutral position to ensure they were not plastically deformed.

Data analysis

The load cell data were manually noted during the experiment, and put into MATLAB R2019b afterwards. The mean applied force and standard deviations were calculated for each defection for both prototypes. The resulting values were combined with their corresponding deflections to obtain a force-deflection curve. The raw data of this experiment are shown in Appendix VI.

B. Experiment 2: Static buckling

Goal and hypothesis

The goal of this experiment was to discover how the magnitude of an axially applied force relates to buckling of the transmission. Similar to the experiment described in Section IV.A, this experiment was conducted with both prototypes. Because buckling deflection is also proportional to the bending moment of inertia, a factor $1.5^3 \approx 3.4$ difference is expected between the applied axial force of both prototypes as well.

Dependent and independent variables

The dependent variable was the axially applied force. The independent variables were the deflection, which was varied from 0 to 10 mm in steps of 1 mm, and the leaf spring thicknesses, which were 0.2 and 0.3 mm.

Experimental setup

This test was similar to the static deflection test, however the drilling device was loaded axially instead of radially. To do this in a controlled manner, a linear stage was used to apply force onto the transmission of the drilling device. A FUTEK 25 lbs load cell is used to measure the applied force, and graph paper with a 1x1 millimetre square grit was used to measure the deflection. The experimental setup is shown in Figure 30.

Experimental procedure

The LabVIEW file was turned on so the measurements from the load cell could be noted. Before proceeding, compensations were made for any offset in the load cell. Both prototypes were tested three times from 0 to 10 mm deflection in 11 steps, so in total 66 measurements were taken. For each test the following sequence was conducted:

1) The linear stage was used to carefully make contact between the cutting head of the prototype and the load cell. This is the starting point at 0 mm deflection.
2) The linear stage was lowered in steps of 0.1 mm until the leaf springs reached a 1 mm deflection.
3) The measured force was noted.
4) The linear stage was again lowered in steps of 0.1 mm until an additional 1 mm of deflection was reached.
5) The measured force was noted.

Steps 4 and 5 were repeated until a total deflection of 10 mm was reached. The procedure of the buckling test is illustrated by Figure 31.

Data analysis

The load cell data was manually noted during the experiment, and put into MATLAB R2019b afterwards. The mean applied force and standard deviations were calculated for each defection for both prototypes. The resulting values were combined with their corresponding deflections to obtain a force-deflection curve. The raw data of this experiment are shown in Appendix VI.

C. Experiment 3: Straight trajectory drilling

Goal and hypothesis

The goal of this experiment was to see how cutting speed, feed rate, and workpiece material density influence the prototype in terms of the necessary cutting force and heat generation. A comparison was made with a regular twist drill in terms of material removal rate, cutting force and heat generation for straight trajectory drilling.

We hypothesised that an increase in cutting speed, which is the oscillating speed of the cutting head, decreases the cutting force, and increases the generated heat. Both an increase in feed rate and in workpiece material density were expected to increase the cutting force and generated heat. Because of the geometry of the cutting particles and the higher cutting speed, the prototype was expected to generate more heat than a regular twist drill.

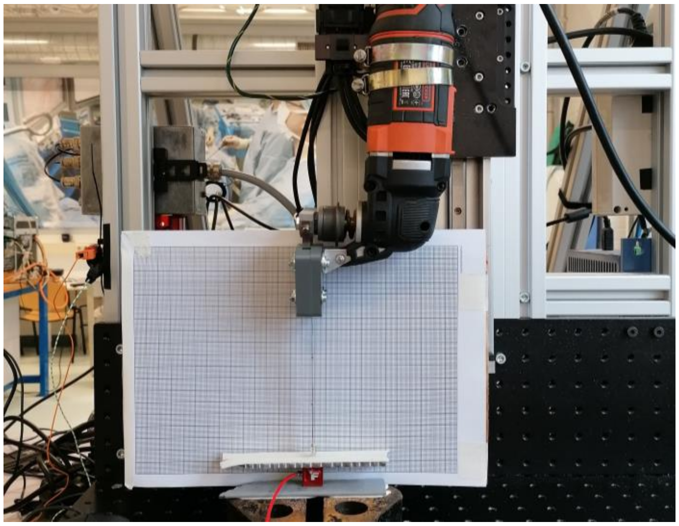

Figure 30: The experimental setup of the buckling test. The prototype is mounted onto the linear stage, above a load cell. Graph paper is placed directly behind it to measure the deflection.

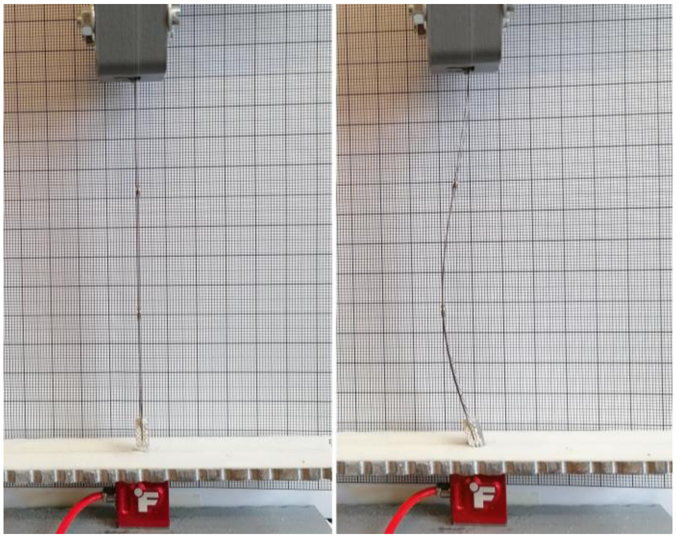

Figure 31: The buckling test starts with the prototype in its neutral position (left), and is axially loaded up to the desired deflection (right).

Dependent and independent variables

The dependent variables for the prototype were the removed mass per cut, the cutting force and the generated heat. The independent variables were the cutting speed, feed rate, and workpiece material density. The cutting speed was varied between 10,000, 16,000 and 22,000 rpm, which are the lowest, middle, and highest settings of the oscillating actuator [31]. The Dremel 9933 tungsten carbide cutter, that is used for the cutting tip, is rated for up to 35,000 rpm [33], the actuator can thus be theoretically run at its maximum settings. The feed rate was varied between 30, 50 and 70 mm/min, because this is a safe velocity in terms of the applied force and generated heat for a regular drill. This is shown in the research of F. Karaca [34]. The workpiece material density was varied between 5, 10 and 15 pounds per cubic foot (PCF). Sawbones closed cell foam was used, which closely mimics the mechanical properties of cancellous bone [23].

The dependent variables for the regular twist drill were the removed mass per cut, the cutting force and the generated heat. The independent variable was the workpiece material density. Only the workpiece material density was varied. Sawbones closed cell foam of 5 and 10 PCF was used.

Experimental setup

To test the prototype, the oscillating actuator was mounted onto the linear stage. This experiment was conducted with the second prototype, with 0.3 mm leaf springs. A FUTEK 25 lbs load cell was placed under the cutting head of the prototype. Three thermocouples were used to measure the temperature of the foam blocks during drilling. Because the actuator vibrates quite violently, the cutting head would also start to oscillate out of plane when it is not supported. This is a problem, because this would influence the distance from the cutting head to the thermocouples, resulting in inconsistent temperature measurements. To counter this, an additional guiding part was 3D printed in which the prototype could slide up and down, but not move from side to side. The experimental setup with the prototype is shown in Figure 32. The Sawbones closed cell foam blocks were cut into slabs of approximately 13x4x2 cm.

To test the regular twist drill as a comparison, a drill chuck connected to a Makeblock 57BYG stepper motor was mounted onto the linear stage instead of the prototype. The experimental setup with the regular drill is shown in Figure 33. The drill bit diameter is chosen to match the cross-sectional area of the bone drilling device. For the bone drilling device, this is 31.6 mm^2. The closest matching conventional drill bit is one with a diameter of 6 mm, which has a cross-sectional area of 28.3 mm^2. According to the research of F. Karaca, a drill bit with a diameter of 6 mm can be run at 200 rpm with a feed rate of 50 mm/min without the risk of necrosis of the surrounding bone [34]. This is why these parameters were chosen for the regular twist drill. The depth of cut was set to 25 mm for all experiments, so at a feed rate of 50 mm/min one cut would take 30 seconds. The retraction rate was set to 60 mm/min for all experiments.

Experimental procedure

The following experiments were conducted:

- For each cutting speed, five cuts were made with the prototype with a feed rate of 50 mm/min, in 5 PCF foam.
- For each feed rate, five cuts were made with the prototype at 22,000 rpm, in 5 PCF foam.
- For each workpiece material density, five cuts would be made with the prototype with a feed rate of 50 mm/min and a cutting speed of 22,000 rpm.
- For both 5 and 10 PCF foam, five holes were drilled with the regular twist drill at 200 rpm with a feed rate of 50 mm/min.

Each of the aforementioned tests was conducted in the following manner. Figure 34 shows the prototype during the experiment.

1) A block of foam was weighed on a TF-4FW scale. This scale has an accuracy of approximately 0.003 g, which is necessary for the difference in weight after a cut is relatively small.
2) The locations for the thermocouples were marked at 10, 20 and 30 mm along the cutting path.
3) The block was placed atop of the load cell and the three thermocouples were inserted so that they are approximately 3 mm from the hole that was drilled. Double sided tape was used to secure the block.
4) The LabVIEW file was turned on, collecting data from the thermocouples and load sensors.
5) The oscillating actuator or stepper motor was turned on, After which the linear stage was turned on, initiating the cut.
6) After the linear stage had reached the 25 mm depth, the oscillating actuator or stepper motor was turned off.
7) After the linear stage had fully retracted the prototype and the graphs of the thermocouples had reached their highest point, meaning that the heat had reached the thermocouples, the LabVIEW file was turned off.
8) The foam block was removed and weighed again. Before weighing, the dust and particles created during drilling were tapped out of the hole.

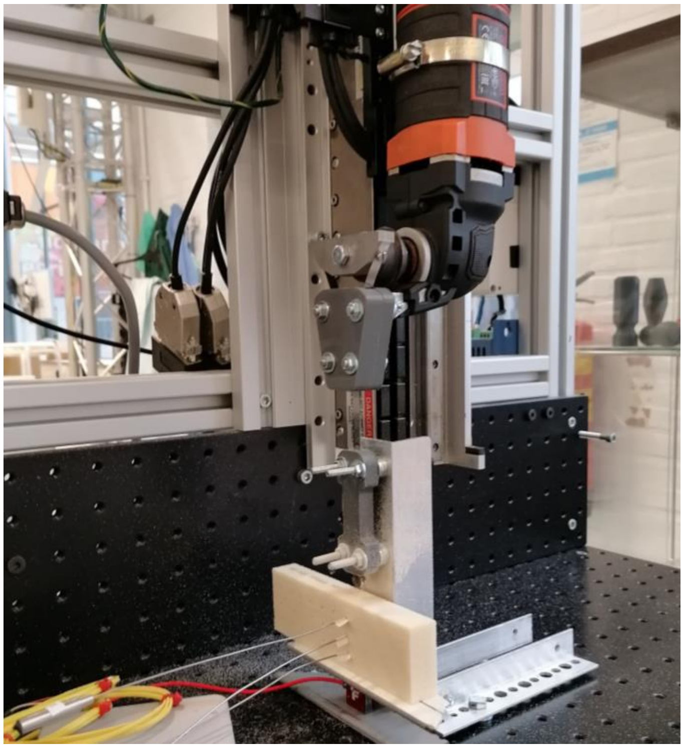

Figure 32: The experimental setup for straight trajectory drilling with the prototype. The tip of the prototype is supported by an additional 3D printed guiding part, which is bolted onto the linear stage. A block of foam is positioned on the load cell, with the thermocouples inserted along the cutting path.

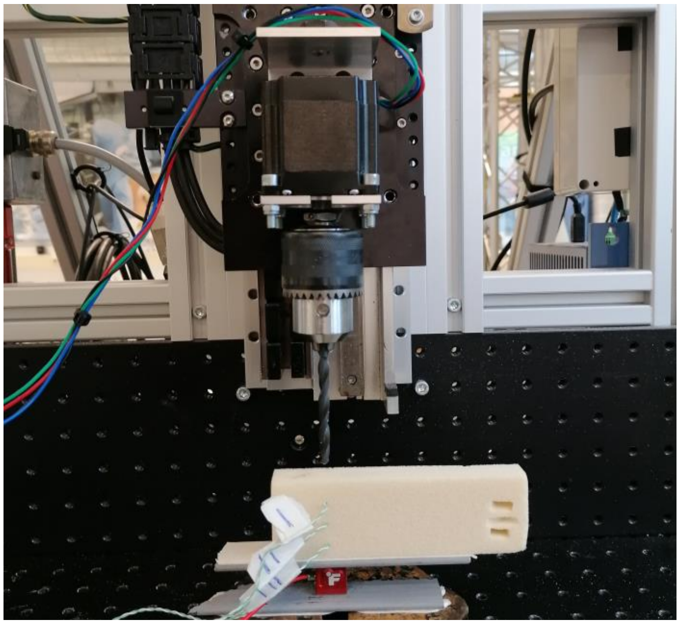

Figure 33: The experimental setup for straight trajectory drilling with the regular drill. A block of foam is positioned on the load cell, with the thermocouples inserted along the cutting path.

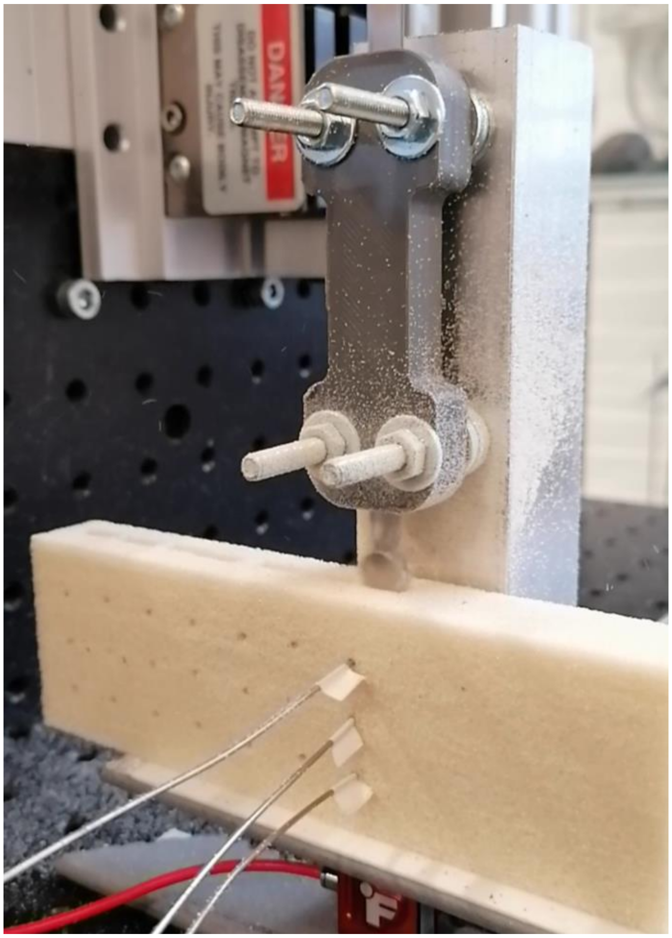

Figure 34: The prototype during the straight trajectory drilling test. The rectangular holes that had already been drilled can be seen on the top left side of the foam block.

Data analysis

The weight measurements were used to calculate the removed mass per each cut, which can be seen in Appendix VI. The time for each cut can be calculated directly from the feed rate, because the hole depth is known. Together, this data was used to calculate the material removal rate [g/s]. The maximum temperature was found for each thermocouple. For each condition, the maximum temperatures were used to calculate the mean maximum temperature, and the standard deviation for all three thermocouples. During testing, the weight of the foam block changes, so there is an offset in the load cell data. This offset was corrected after testing by setting the measured load before drilling to zero. Similarly to the temperature data, the maximum cutting forces were extracted from the load cell data, and for each condition a mean maximum cutting force and standard deviation were calculated. For some of the measured maximum temperatures and cutting forces, analysis of variance was used to see if the differences are statistically significant. If the p-values are lower than $5*10^{-2}$, the difference in temperature or cutting force can be seen as significant. This means that the risk of unjustly concluding a difference in temperature is less than 5% [35].

D. Experiment 4: Curved trajectory drilling

Goal and hypothesis

The goal of this experiment is to discover if steering based on difference in material properties, or wall guidance as discussed in Section II.E, is a viable strategy. In other words, how the insertion angle with respect to a simulated cortical layer relates to deflection of the cutting tip. The cutting tip was expected to deflect, because of the difference in material properties between the simulated cancellous and cortical bone.

Dependent and independent variables

The dependent variable in this experiment was the deflection of the cutting tip. The independent variable was the insertion angle. It was hard to predict up to which angle the prototype would be able to deflect off of the simulated cortical wall. As a solution, a stand was made that could be angled from 10˚ up to 45˚, with the idea to steadily increase the insertion angle. The Sawbones 5 PCF closed cell foam was used to simulate the cancellous bone, and a plate of Sawbones thick short fibre epoxy was used to mimic the cortical outer layer of bone. The feed rate was kept constant in this experiment at 50 mm/min. The cutting speed was set to 16,000 rpm. It seemed sensible to set the actuator to less than the maximum possible cutting speed, because both the bending of the prototype and the hard fibre reinforced epoxy increased the likelihood that the prototype would break.

Experimental setup

This experiment was conducted with the second prototype, with 0.3 mm leaf springs. The oscillating actuator was mounted onto the linear stage, similar to the test described in the previous Section IV.C. This time however, because a deeper cut was required for the prototype to deflect, and because the placement of the hole was less critical, the additional 3D printed guiding part was not used. Instead, the cutting head of the device was guided by hand and released once it had entered the workpiece material. The experimental setup is shown in Figure 35.

Experimental procedure

The stand was first set to an insertion angle of 10˚. The tests were conducted in the following manner:

1) The 5 PCF foam and fibre reinforced epoxy were secured onto the stand with a clamp.
2) The oscillating actuator was turned on.
3) The linear stage was turned on, initiating the cut.
4) The prototype cut into the cancellous bone phantom and advanced into the simulated cortical bone layer. If the cutting tip dug into the simulated cortical layer, the experiment was stopped immediately to prevent failure of the prototype.
5) If the cutting tip was able to deflect, the cut was continued all the way through the cancellous bone phantom.
6) The oscillating actuator was turned off and the prototype was retracted from the foam.

Figure 35: The experimental setup for curved trajectory drilling with the prototype. A block of foam is clamped onto the simulated cortical wall, which is indicated by the red arrow, and placed at an angle below the prototype.

The insertion angle was increased in steps of 5˚ up to the point where the cutting head of the prototype would no longer deflect off of the simulated cortical wall. Three cuts were made before advancing to the next insertion angle.

Data analysis

The 5 PCF closed cell foam and the simulated cortical wall were examined after the experiment. By separating the two, the marks made by the cutting head in the plate of Sawbones short fibre epoxy were made visible. The block of foam was cut along each cutting path, in order to make a side view of the curved holes.

E. Results

Experiment 1: Static deflection

Figure 36 shows how the magnitude of a transverse applied force relates to deflection of the cutting head, for both prototypes. The mean applied forces at 50 mm deflection are 0.11 and 0.44 N for the 0.2 and 0.3 mm transmissions, respectively.

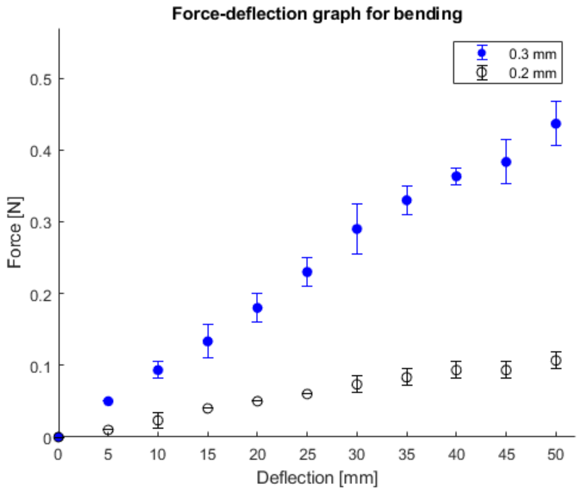

Figure 36: Force-deflection graph for the bending of the two prototypes. The mean force per deflection is marked with a dot, and the error bars show one standard deviation.

Experiment 2: Static buckling

Figure 37 shows how the magnitude of an axially applied force relates to deflection of the transmission, for both prototypes. Each line in the graph represents one continuous measurement. For the 0.2 mm transmissions, the three measurements are close to each other. The measured forces at 10 mm deflection are approximately 2.2 N. For the 0.3 mm transmission, one of the measurements stands out from the other two. It flattens later than the other two and has a lower maximum force. The measured forces at 10 mm deflection are 7.8, 8.3, and 8.5 N.

Experiment 3: Straight trajectory drilling

The straight trajectory drilling experiments were conducted with the 0.3 mm prototype only. Figure 38 shows the material removal rates of the prototype and a regular drill for two bone phantom densities. The mean material removal rates of the prototype are 2.7*10^{-3} and 5.0*10^{-3} [g/s] for 5 and 10 PCF,

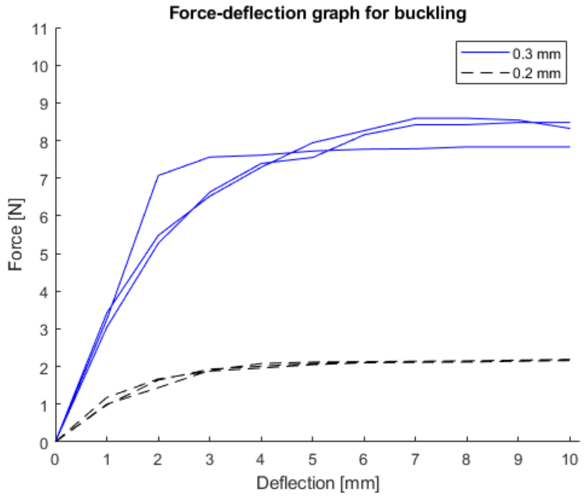

Figure 37: Force-deflection graph for buckling of the two prototypes. Each line represents one continuous measurement.

respectively. The mean material removal rates for the regular drill are $1.7*10^{-3}$ and $3.2*10^{-3}$ [g/s]. The spread in material removal rate of the prototype is higher than that of the conventional drill for both bone phantoms. Because the feed rate is constant, the material removal rate for the 10 PCF phantom is roughly twice as high as for the 5 PCF phantom, for both the prototype and the regular drill. The prototype was also tested on a 15 PCF foam, it was however unable to cut through it and got stuck at a depth of 10 mm into the foam. To prevent breaking the prototype, the 15 PCF test was left out.

Figure 39 shows the maximum measured axial cutting forces of the prototype and a regular drill for two bone phantom densities. The cutting forces of the prototype are lower than those of the regular drill. When the material density is doubled, the axial cutting forces of the prototype increase proportionately more than those of the regular drill. The mean axial cutting forces of the prototype are 0.5 and 1.7 N for 5 and 10 PCF, respectively. The mean axial cutting forces for the regular drill are 2.1 and 3.0 N. In one of the five tests with the prototype on 10 PCF foam, the maximum measured cutting force was considerably lower than the rest, at 1.0 N.

Figure 40 shows the characteristic temperature curves of the prototype and a regular drill. The graph contains the measured temperatures for one test in 10 PCF foam at a cutting depth of 10, 20 and 30 mm. It is remarkable that the generated heat of the prototype was measured after the hole had been drilled, while the cutting head was retracted from the foam. The highest temperature was measured at 10 mm. The measurement at 20 mm lags behind the one at 10 mm, and is lower. A small rise in temperature was registered at 30 mm after the prototype had been retracted from the foam. The regular drill did not generate a significant amount of heat.

Figure 41 shows the maximum measured axial cutting forces of the prototype for different cutting head speeds, with a feed rate of 50 mm/min in 5 PCF foam. The mean axial cutting forces are 1.00, 0.59 and 0.46 N for 10,000, 16,000 and 22,000 rpm, respectively. Less than five red dots are shown per cutting speed in Figure 41, because some of the measured forces are equal to each other. Analysis of variance was used to see if the difference in measured force is statically significant. The p-values found, when comparing the values for 22,000 with 16,000 rpm, and 16,000 with 10,000 rpm, are $6.80*10^{-5}$ and $6.81*10^{-7}$, respectively. These p-values are smaller than $5*10^{-2}$, so the difference in axial cutting force is statistically significant.

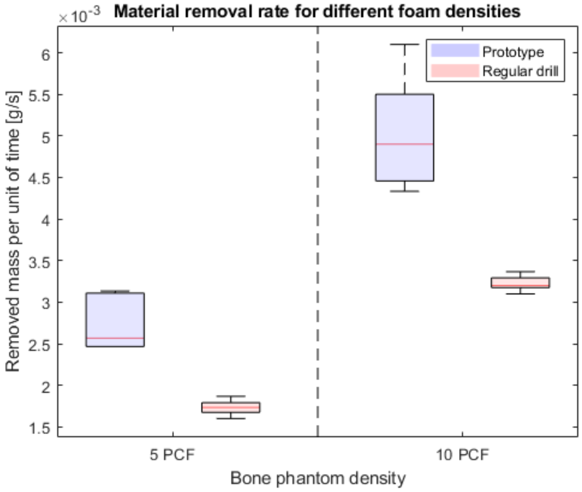

Figure 38: A box plot of the material removal rates of the prototype and a regular drill for two bone phantom densities. The horizontal red lines indicate the median. The top and bottom of the boxes are the upper and lower quartile, respectively. The lines above and below the boxes indicate variability outside this interquartile range.

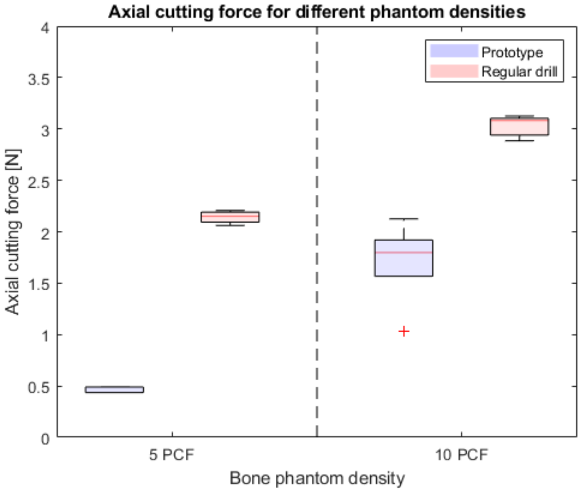

Figure 39: A box plot of the measured axial cutting forces of the prototype and a regular drill for two bone phantom densities. The top and bottom of the boxes are the upper and lower quartile, respectively. The lines above and below the boxes indicate variability outside this interquartile range. An outlier is indicated by the red + sign.

Figure 42 shows the maximum measured temperatures of the prototype for different cutting head speeds, with a feed rate of 50 mm/min in 5 PCF foam. The measured temperature decreases as the cutting depth increases for all cutting head speeds. The highest temperatures were consistently found at 22,000 rpm. Analysis of variance was used to see if the increase in temperature from a cutting speed of 16,000 to 22,000 rpm is significant. The p-values at cutting depths of 10, 20 and 30 mm are $1.17*10^{-2}$, $0.10*10^{-2}$ and $0.71*10^{-2}$, respectively. These p-values are smaller than $5*10^{-2}$, so the difference in temperature is statistically significant.

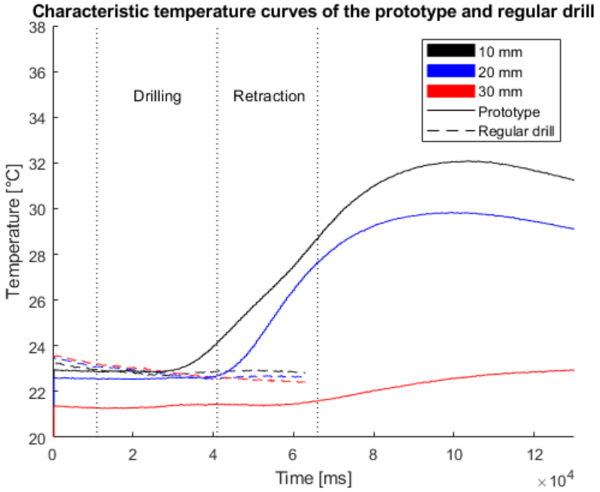

Figure 40: Characteristic temperature curves of the prototype and a regular drill, at various cutting depths in 10 PCF foam. The vertical dotted lines indicate the intervals of drilling into the foam, and retraction from it.

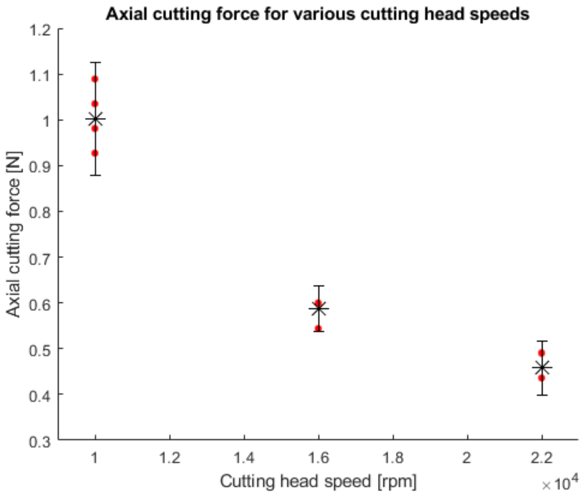

Figure 41: The measured axial cutting forces of the prototype for different cutting head speeds, with a feed rate of 50 mm/min in 5 PCF foam. The means are indicated by asterisks and the different measurements are indicated by red dots. The error bars show one standard deviation.

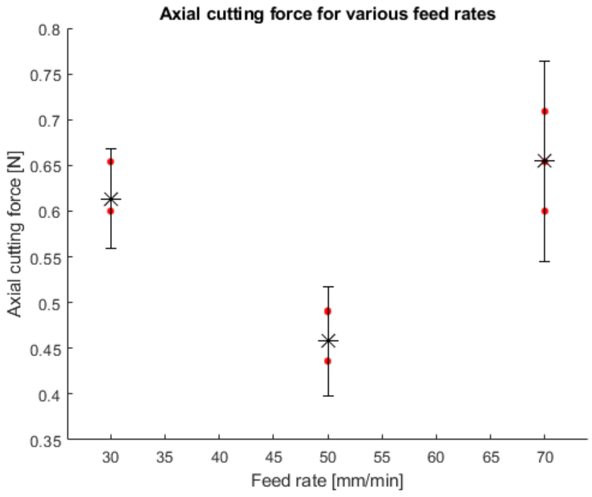

Figure 43: The measured axial cutting forces of the prototype for different feed rates, with a cutting speed of 22,000 rpm in 5 PCF foam. The means are indicated by asterisks and the different measurements are indicated by red dots. The error bars show one standard deviation.

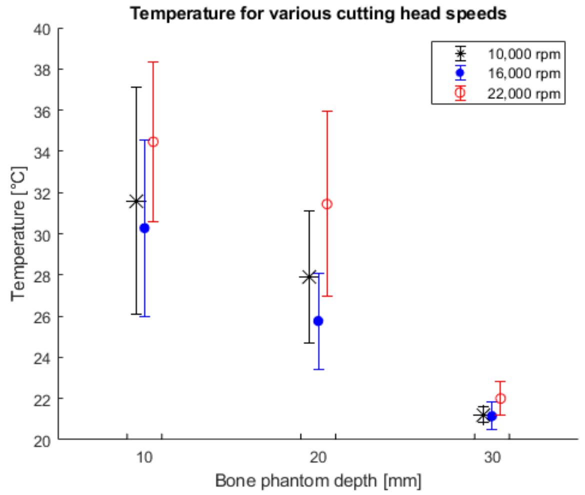

Figure 42: The maximum measured temperatures of the prototype for different cutting head speeds, with a feed rate of 50 mm/min in 5 PCF foam.

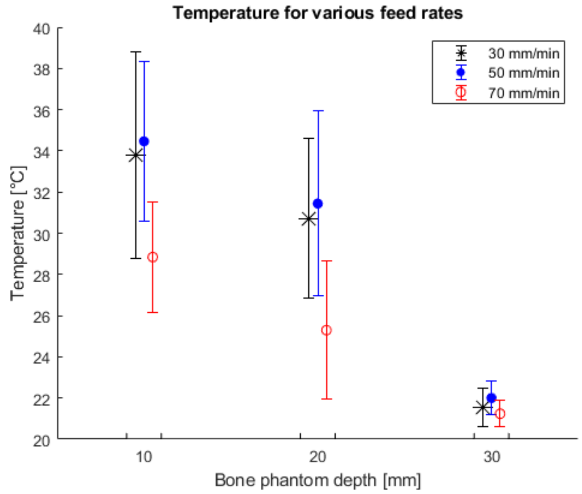

Figure 44: The maximum measured temperatures of the prototype for different feed rates, with a cutting speed of 22,000 rpm in 5 PCF foam.

Figure 43 shows the maximum measured axial cutting forces of the prototype for different feed rates, with a cutting speed of 22,000 rpm in 5 PCF foam. The mean axial cutting forces are 0.61, 0.46 and 0.65 N for 30, 50 and 70 mm/min, respectively. Less than five red dots are shown per cutting speed in Figure 43, because some of the measured forces are equal to each other. Analysis of variance was used to see if the difference in measured force is statically significant. The p-values found, when comparing the values for 70 with 50 mm/min, and 50 with 30 mm/min, are $1.05*10^{-4}$ and $3.51*10^{-4}$, respectively. These p-values are smaller than $5*10^{-2}$, so the difference in axial cutting force is statistically significant.

Figure 44 shows the maximum measured temperatures of the prototype for different feed rates, with a cutting speed of 22,000 rpm in 5 PCF foam. The measured temperature decreases as the cutting depth increases for all feed rates. The lowest temperatures were consistently found at 70 mm/min. Analysis of variance was used to see if the decrease in temperature from a feed rate of 50 mm/min to 70 mm/min is significant. The p-values at cutting depths of 10, 20 and 30 mm are $0.07*10^{-2}$, $0.12*10^{-2}$ and $1.15*10^{-2}$, respectively. These p-values are smaller than $5*10^{-2}$, so the difference in temperature is statistically significant.

Experiment 4: Curved trajectory drilling

The prototype was able to deflect off, and follow the simulated cortical wall in a straight line up to an insertion angle of 15˚. Three successful tests were conducted at an angle of 10˚, and another three at 15˚. The cortical wall was only lightly scratched at 10˚. At 15˚, the scratches in the cortical wall are noticeably deeper. At 20˚, the prototype was not able to deflect off the cortical wall and cut into the material. Figure 45 shows side views of the cutting paths and the marks on the simulated cortical wall for insertion angles of 10˚, 15˚ and 20˚.

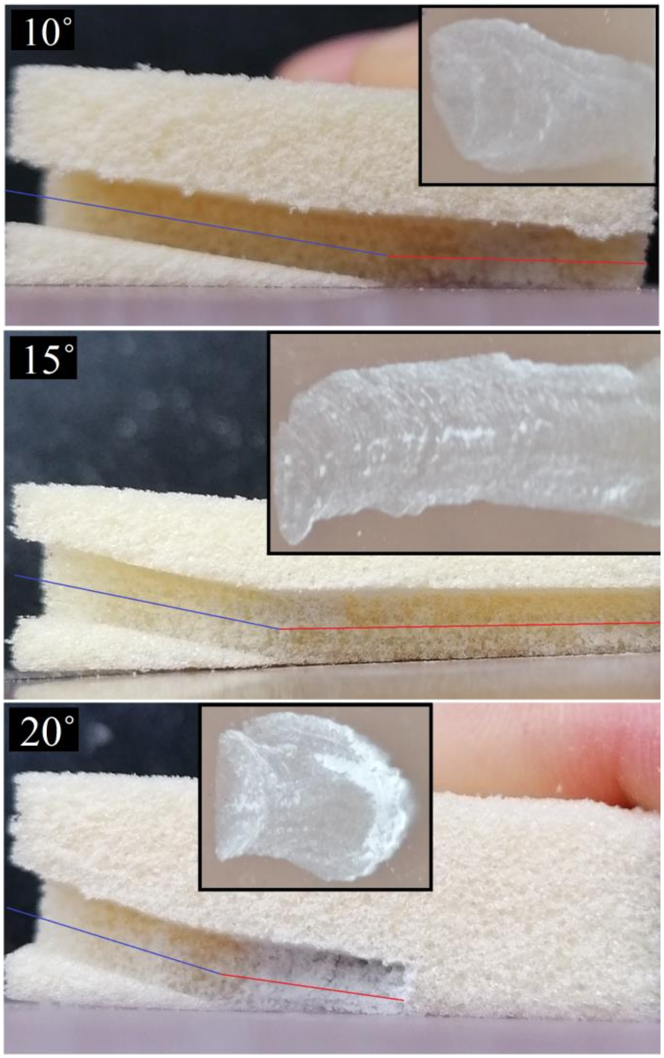

Figure 45: Side views of curved cutting paths in 5 PCF foam. From top to bottom, the insertion angles are 10˚, 15˚ and 20˚. The blue lines indicate the initial drilling direction, and the red lines the drilling direction after the cutting head came into contact with the simulated cortical wall. Top views of the simulated cortical wall are outlined in black. The horizontal positions of which correspond to that of the side views.

V. DISCUSSION

A. Main Results

Bending and buckling tests

The prototype presented in this study was evaluated in four experiments: In Experiment 1 and 2, the stiffness of the prototype with 0.3 mm thick leaf springs was four times higher than that of the prototype with 0.2 mm leaf springs, which was higher than expected based on the calculations made in Section IV.A. A possible explanation of this behaviour could be friction between the two leaf springs. The three pins holding the leaf springs together were riveted on tighter in case of the 0.3 mm prototype, resulting in extra friction between the two leaf springs, which prevents them from freely sliding over each other, increasing the overall stiffness of the transmission.

Straight trajectory drilling

In Experiment 3, the axial cutting forces in the 5 and 10 PCF Sawbones closed cell foam were lower than the force at which buckling occurs, and the prototype could successfully cut through. In case of the 15 PCF foam, the transmission buckled while the measured force rapidly increased up to 50 N, after which the experiment was stopped. At that point, the prototype had cut approximately 10 mm into the foam. The prototype is thus able to cut 15 PCF to some extent, it could however not keep up with the 50 mm/min feed rate. As the density of the closed cell foam increases, the strength of the foam also increases [23], logically increasing the necessary cutting force. Another aspect to consider is the volume fraction, which also increases with the foam density [23]. The loose particles generated during cutting can be pushed into the cavities of the foam, clearing the cutting path. The increase in volume fraction may be the reason why the axial cutting forces increase proportionally more in case of the prototype than with a regular drill, when the foam density is increased from 5 to 10 PCF. This is because the regular drill has flutes, that are designed to remove the generated particles from the hole, and the prototype does not. Even though the prototype and regular drill have the same cross-sectional area, the material removal rate of the prototype was higher because the cutting head moves slightly from side to side. This is because its centre of rotation is not in its geometrical centre.

During the cutting tests, the prototype generated a measurable amount of heat, while the regular drill did not seem to increase the temperature of the foam at all. The highest temperature was measured when the prototype was retracted from the hole, which means that the prototype had heated up significantly during drilling. This may be because of the flat sides on either side of the cutting head, which constantly rub against the foam during oscillation. The same cutter that was used for the cutting head produced notably less heat in the tests of Appendix II, in which no flat sides were present. Another possibility is that the friction between the leaf springs generated heat, which was passed on to the cutting head.

Similar to conventional drilling, decreasing the cutting speed of the prototype increases the axial cutting force [36]. Decreasing the cutting speed from 22,000 to 16,000 rpm significantly decreased the generated heat. In conventional drilling, increasing the feed rate increases the axial thrust force [36]. As expected, increasing the feed rate from 50 to 70 mm/min significantly increased the axial cutting force of the prototype. Unexpectedly however, lowering the feed rate from 50 to 30 mm/min increased the axial cutting force from 0.46 to 0.61 N. This may be explained by means of the machining theory of Appendix I, in which the concept of the critical cutting depth is introduced. If the cutting depth is too low, the abrasive particle is not able to shear off a piece of material and ploughs through the surface. It is possible that a feed rate of 30 mm/min was not fast enough to reach the critical cutting depth in time, and that ploughing of the cutting head increased the measured axial force. Increasing the feed rate has shown to decrease the generated heat. A higher feed rate means that more material is removed per unit of time, which would logically also increase the amount of heat that is generated per unit of time.

However, if the cutting depth is constant, the total drilling time decreases, which would mean that the prototype has less time to generate heat.

Curved trajectory drilling

In Experiment 4, the cutting head changed direction as soon as it hit the simulated cortical wall, as seen in Figure 45. If the prototype was able to fully deflect off of the cortical wall, it drilled along it in a straight line, instead of continuing the curved path. In case of the 20° insertion angle, the sharp edge of the cutting head dug into the cortical wall, creating a ledge from which the cutting head could no longer deflect. To prevent this, and thus to increase the insertion angle at which wall guidance is possible, the edges of the cutting head could be rounded off. For smaller insertion angles, *e.g.*, 10° and 15°, the prototype deflected successfully off of the simulated cortical wall.

B. Limitations and Recommendations

The Sawbones closed cell foam, that was used in the cutting tests, is made for mechanical testing. While it closely mimics the mechanical properties of cancellous bone, it does not replicate its thermal properties. Because of this, the thermocouple data cannot be interpreted in the absolute sense, but still provide insight in the way heat is generated by the drilling device. Furthermore, the pores of the Sawbones closed cell foam are an order of magnitude smaller than the 1 mm mean intertrabecular space of cancellous bone, which has an open cell structure [5]. These differences may influence the cutting forces and generated heat.

During experiment 2 described in Section IV.B, the position of the cutting head with respect to the load cell may have differed between tests. This would explain the inconsistency in the force deflection graph of the 0.3 mm prototype, as seen in Figure 37. Fixing the lateral position of the cutting head with respect to the load cell would solve this problem. During experiment 3 as seen in Section IV.C, the additional guiding block, that constrained the cutting tip from moving sideways and out of plane, was subjected to high temperatures due to friction and melted on the inside. The transmission came into contact with molten plastic, which may have influenced the measured axial forces. Furthermore, the resolution of the FUTEK 25 lbs load cell is relatively low. As seen in the axial force graphs of experiment 3 of Section IV.E, the data points are spaced approximately 0.06 N apart, and multiple data points often overlap. Obtaining consistent data using thermocouples also proved to be difficult, because the measured temperature strongly depends on the distance from the thermocouple to the cutting path. In experiment 4 described in Section IV.D, the horizontal position of the prototype was constrained. This rigid connection to the linear stage resulted in a compound bend in the flexible transmission, which made it more difficult for the cutting head to deflect. Allowing the base of the transmission to translate horizontally would eliminate the compound bend, which could increase the maximum insertion angle at which the cutting head is able to deflect off of the simulated cortical wall. This idea is illustrated in Figure 46.

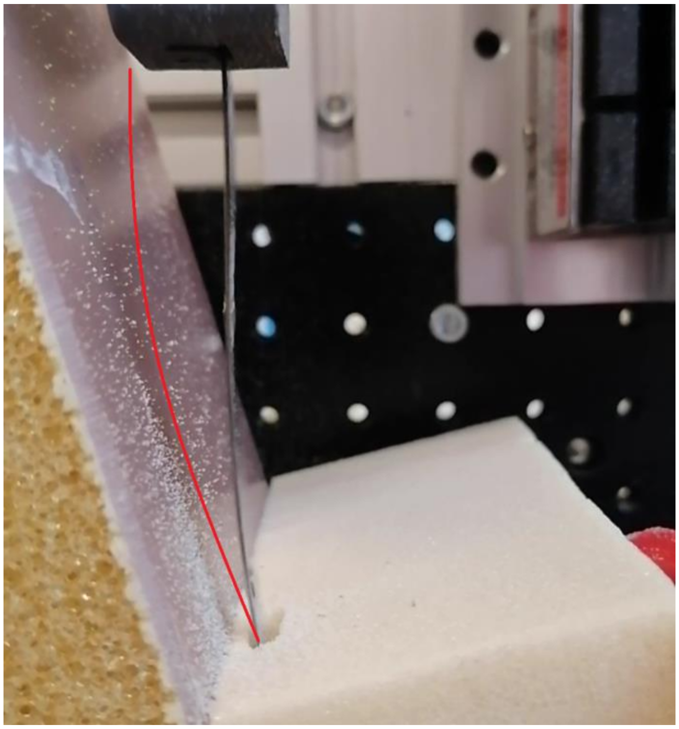

Figure 46: The compound bend in the flexible transmission in the curved trajectory drilling test, which is caused by the fixed position of the base of the transmission. If the base is not horizontally constrained, the transmission could bend as illustrated by the red line. This may increase the maximum insertion angle.

C. Scale Effects

The size of the prototype that was built in this research is in the right order of magnitude for its intended use in spinal fusion operations. The prototype could be refined for this purpose without the need to take scale effects into account. However, if the concept of this drilling device is to be used on a different scale, it is worth exploring how changing the size of the device would influence its performance and manufacturability.

If a slot is desired for thin bone anchors such as the flexible steel tape anchor [1], the width of the cutting head needs to be decreased. To truly minimise the thickness however, it would be more suitable to change the connection between the cutting head and the leaf springs. As stated in Section II.D, the leaf springs can be placed on the outside or inside of the cutting head. Placing the leaf springs on the inside has the potential of an overall thinner device, as seen in Figure 14.

If the height of the device is to be minimised for the use on smaller bones, such as the cervical vertebrae, the hinge pins that connect the leaf springs to the cutting head could become critical. A solution could be to eliminate these pins altogether by integrating the transmission and the cutting head into one compliant part. A concept of this compliant version of the drilling device is shown in Figure 47. Note that the mechanism of this flexible transmission is fundamentally different, because the flexures cannot overlap.

An increase in drilling depth may be needed if another path through the vertebrae is chosen, which would require a longer transmission. If the length of the flexile transmission is increased, more pins are needed to account for buckling due to

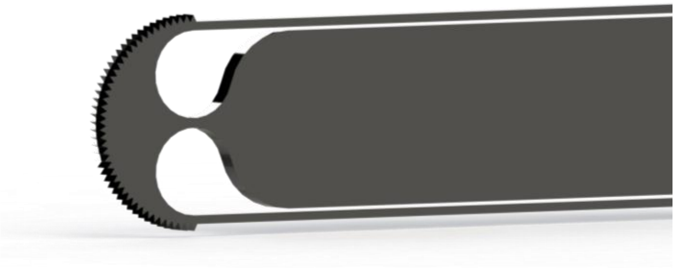

Figure 47: A concept of a compliant version of the drilling device.

the cutting forces. More points of contact between the leaf springs result in more friction during oscillation. However, friction between the drilling device and the workpiece material remains constant, because this depends on the contact with the cutting head. This is another advantage of the drilling device over conventional drilling, in which drilling depth is the biggest factor in heat generation except for tool diameter [12].

D. Medical Implementation

The drilling device presented in this research is designed to be used in spinal fusion operations. To drill along the path shown in Figure 5, flexibility in the range of 45˚ to 90˚ with a bending radius of ±15 mm is required. This is necessary in order to follow the cortical wall of the vertebral body, which can be seen as an elliptic cylinder with a minor diameter in the range of 30 mm [43]. A bending radius of 15 mm is however too small for the leaf springs of the transmission. The 0.3 mm prototype can be comfortably bent up to 90˚ with a bending radius of approximately 50 mm. An alternative to improving the flexibility of the transmission could be to choose other paths through the vertebrae, that do not require such sharp bends. An option would be to move through the pedicle and upwards along the anterior cortical wall. Furthermore, the drilling device is not limited to vertebral drilling, but can be used in a wide variety of orthopaedic surgeries.

The drilling device is meant to be handheld by the surgeon operating it, similar to the pedicle probe. If the prototype would be used in its current state, the surgeon would have one hand on the actuator, controlling the on-off switch and the cutting speed dial, and one hand on the flexible transmission, guiding the cutting tip. The prototypes were made out of stainless steel alloys, which means they are already biocompatible. The tungsten carbide teeth are brazed onto the cylinder, prevent them from braking off inside the bone during surgery.

E. Future Research

In future prototypes, excessive heat generation should be prevented. Heat generation at the flat sides of the cutting head could be minimised by eliminating the contact between the side of the cutting head and the workpiece material. This can be done by making the sides concave instead of flat, which is shown in Figure 48a. Another option would be to give the cutting head a taper in the top plane, which is shown in Figure 48b. Heat generation between the two leaf springs may be minimised by adding a low friction coating. These adaptations would also make the system more efficient, because the drilling energy is directly related with the amount of heat generated during drilling [37].

In this research, steerability by means of wall guidance was tested. The cutting head design could be optimised for wall guidance by rounding off the sharp corners on the sides, which would decrease the chance that the cutting head gets stuck on the cortical layer. A rounded cutting head can be seen in Figure 48c. Note that this concept can be combined with those seen in Figures 48a and 48b.

As stated before in Section II.E, other types of steerability may be implemented besides wall guidance. Tool dependent steerability can for instance be realised by using an asymmetrical cutting head. This asymmetry could be achieved by creating an angled surface on one side of the cutting head. This angled surface would be subjected to a reaction force perpendicular to it, which pushes the cutting head to one side. This concept is shown in Figure 48d. Another implementation of tool dependent steerability would be to permanently bend the transmission. This way, the cutting head would follow the curve of the leaf springs. Tool dependent steerability however has the downside that the curvature in the cutting path is constant.

The final option is user dependent, or active, steerability. The drilling device could be made actively steerable by adding cables on either side of the transmission. Pulling one of the cables would bend the transmission in that direction. It is also possible to improve on this idea by attaching multiple cables along the length of the transmission, which would allow the operator to bend the transmission in a specific location. This also makes it possible to create compound bends in the transmission. This principle is demonstrated by the HelicoFlex [29] in Figure 49. This type of steerability would provide the most freedom, but the implementation is complex because of the added parts.

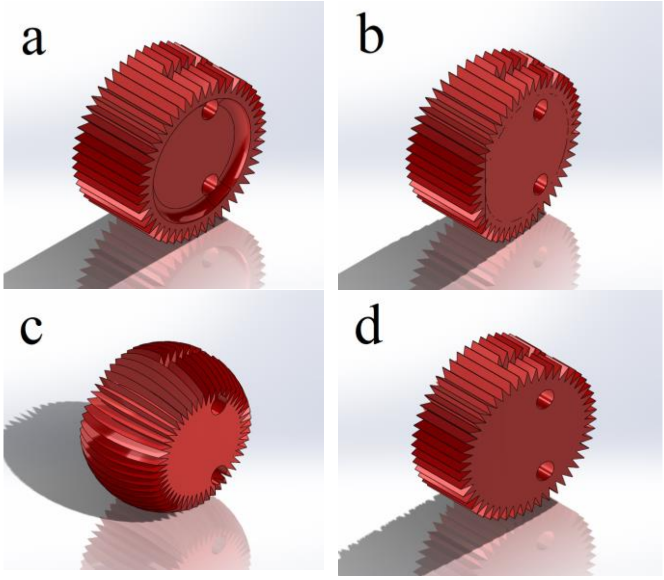

Figure 48: Different adaptations of the cutting head design. a) Making the sides concave to reduce contact area. b) A taper in the top plane to reduce contact area. c) Rounded corners to increase performance for wall guidance. d) An asymmetrical surface which pushes the cutting head to one side.

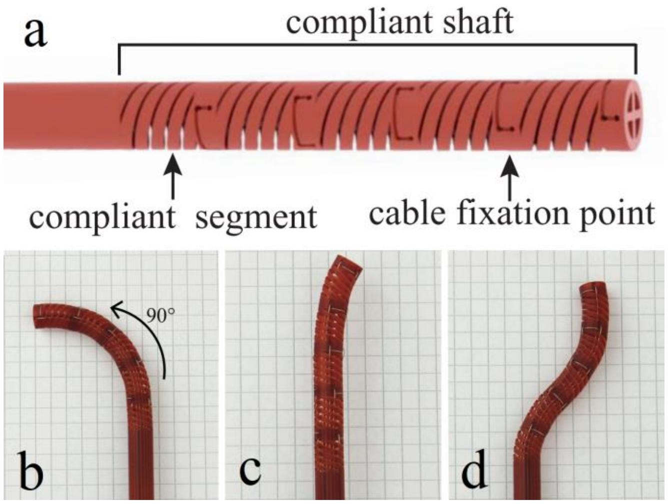

Figure 49: Active steerability as shown by the HelicoFlex. a) Each compliant section of the shaft has a cable fixation point, which allows each segment to be controlled separately. This makes it possible to: b) bend the shaft as a whole in one direction, c) bend one specific segment individually, and d) create a compound curve in the shaft. (Figure adapted from Culmone et al.[29]*).*

Another idea for future research, that may be relevant depending on the intended application, is to locally manipulate the stiffness of the transmission by decreasing the height or thickness of the leaf springs. It may be useful to increase flexibility near the cutting head to make steering it easier. It needs to be stated that increasing flexibility locally will decrease the overall transmittable cutting force. To counter this, the necessary cutting force could be lowered by optimising the teeth profile of the cutting head. The teeth of the Dremel 9933 bit are blunt and have a negative rake angle. The machining theory of Appendix I has shown that tool shape and sharpness are among the major independent variables of the cutting process [30]. Implementing sharp teeth with positive rake angles would likely reduce the required cutting force. Making the centre of rotation coincide with the geometrical centre of the cutting head would reduce the amount of material that is removed per oscillation, by eliminating any sideways movement. This would also lower the cutting force, especially in case the cutting head gets stuck in the workpiece. One final option is to decrease the size of the cutting teeth, which would decrease the amount of material that the cutting head is able to remove per oscillation. While this results in lower cutting forces, it also decreases the feed rate at which the device can be used, which would give it more time to generate heat.

The most interesting aspect of the drilling device presented in this research is its flexibility. However, another useful feature of this concept is that the shape of the hole depends on the cross-sectional shape of the cutting head. Besides the rectangular cross section that was used in the prototypes, square, round, and oval shapes are all possibilities, depending on the desired shape of the hole. If flexibility is not required, the drilling device could be specialised to make straight holes with unconventional cross sections by increasing the stiffness of the transmission. An easy way to realise this is to make folds in the leaf springs along their length-axis. With the aforementioned improvements, the vertebral drill presented in this research may be used in a wide variety of orthopaedic applications.

VI. CONCLUSION

This research presents the design, prototype and evaluation of a flexible bio-inspired bone drilling device. The motion of the cutting surface, with its axis perpendicular to the drilling direction, is inspired by the proboscis of the tsetse fly. The prototype was capable of effectively drilling through Sawbones closed cell foam with densities up to 10 PCF with a feed rate of 50 mm/min. The prototype was designed to be flexible in a two-dimensional plane, with the goal to follow the cortical outer layer of the vertebral body, which could facilitate innovative bone anchors. Steerability by means of wall guidance was tested and was effective up to insertion angles of 15˚. Compared to conventional drilling, the prototype requires lower axial forces, at the cost of more generated heat. Heat generation can be minimised by reducing friction between the cutting head and the workpiece material, and between the leaf springs that comprise the transmission. The properties of the leaf springs in the transmission determine its lateral flexibility, which is necessary to make the device steerable, and its axial stiffness, which is necessary to transmit the cutting forces. In future prototypes, the goal should thus be to minimise the generated heat and necessary cutting force, while increasing the flexibility. The drilling mechanism presented in this research is a major step in the development of steerable drilling devices for orthopaedic applications.

APPENDIX I: MACHINING THEORY

Orthogonal Cutting

Effectively implementing the cutting mechanism of the tsetse fly requires an understanding of the mechanics of a cutting operation, which can be found in fundamental machining theory. Conventional rotary cutting tools, such as mills and circular saws, have their axis of rotation perpendicular to the cutting direction, similar to the proboscis of the tsetse fly. These cutting mechanisms can be explained with the use of a two-dimensional model, also known as the orthogonal cutting model, which is shown in Figure 50. The model shows a cutting tool that travels from right to left through the workpiece. The independent variables in this model are the tool geometry, its movement with respect to the workpiece and the workpiece material. This includes the rake angle α [˚], relief angle, depth of cut t_0 [m] and the cutting velocity V $[m/s]$. These influence the chip formation. The dependent variables are thus chip thickness t_c [m], the shear angle φ [˚], surface finish, but also the forces that are generated during cutting and with that the dissipated heat.

A cutting operation can be modelled using the definition of power. The cutting power is the product of the velocity of the cutting tool with respect to the workpiece, V $[m/s]$, and the force applied to the workpiece by the cutting tool, F_c $[N]$. The cutting power is thus given by:

$$P_c = F_c V \quad \left[\frac{Nm}{s}\right] \qquad (1)$$

The volume of material that is removed from the workpiece per second is calculated by multiplying the radial infeed velocity, v_f $[m/s]$ with the cross-sectional area of the hole. In case of a rectangular hole, this area is the length, a $[m]$ multiplied by the width, b $[m]$ [38]. The volumetric removal rate is thus given by:

$$Q = v_f\, ab \quad \left[\frac{m^3}{s}\right] \qquad (2)$$

Dividing the cutting power by the volumetric removal rate yields the energy that is needed to remove a certain volume of material from the workpiece, the specific cutting energy:

$$u_c = \frac{P_c}{Q} \quad \left[\frac{J}{m^3}\right] \qquad (3)$$

It is possible to further decompose the cutting force and velocity to see which parameters influence the specific cutting energy. Figure 51a shows the cutting force F_c $[N]$ and the tangential force F_t $[N]$, which pulls the cutting tool into the workpiece. These two forces can be combined into the resultant force R $[N]$. This resultant force is decomposed in two ways: First with a component along the rake face of the tool, with angle α. This gives force F $[N]$, which is the friction force between the chip and the tool. The second decomposition is done along the shear plane, with angle φ [˚]. This gives force F_s $[N]$, *i.e.* the shear force. This is the force component that actually deforms the workpiece. Figure 51b shows the cutting speed V $[m/s]$, also decomposed along the rake face and shear plane. This provides the chip velocity V_c $[m/s]$ and shear velocity V_s $[m/s]$, respectively. It is now possible to multiply the found forces with their corresponding velocities. This yields the shearing power, P_s $[Nm/s]$ and friction power, P_f $[Nm/s]$:

$$P_s = F_s V_s \quad \left[\frac{Nm}{s}\right] \qquad (4)$$

$$P_f = F V_c \quad \left[\frac{Nm}{s}\right] \qquad (5)$$

Dividing the shearing power and friction power by the volumetric removal rate, Q $[m^3/s]$, yields the specific energies for shearing and friction, which comprise the specific cutting energy:

$$u_c = u_s + u_f \quad \left[\frac{J}{m^3}\right] \qquad (6)$$

This shows that the power needed for a cutting operation depends on the shearing of the workpiece material and the friction between the chip and tool [30].

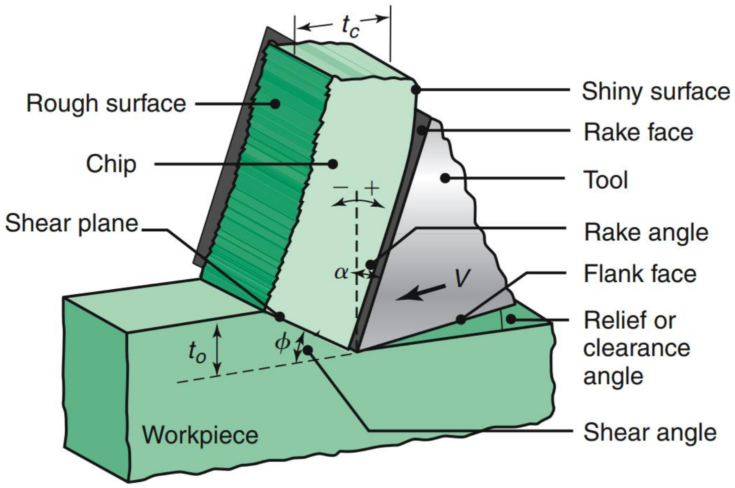

Figure 50: The orthogonal cutting model. (Figure adapted from Kalpakjian et al. [30]*).*

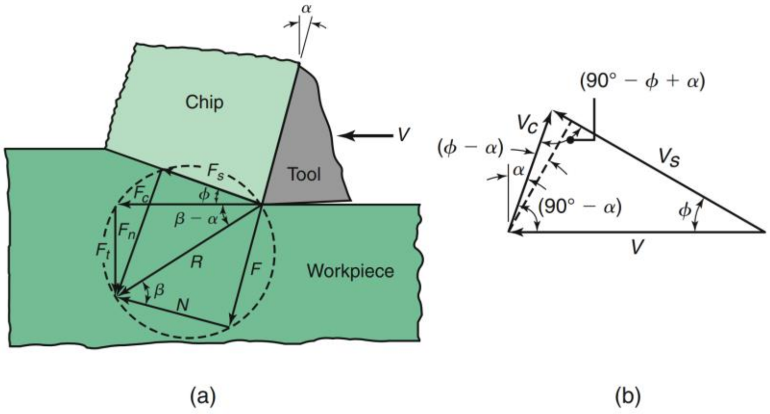

Figure 51: The different components of the cutting force and velocity. (Figure adapted from Kalpakjian et al. [30]*).*

Abrasive Machining

Another type of conventional machining, that is often used in combination with a rotary motion, is grinding or abrasive machining. The fundamental difference between a grinding and cutting operation is the geometry of the tool. A grinding operation utilises abrasive grains to remove material from the workpiece. The grains that comprise the cutting surface are irregularly shaped and orientated randomly, which makes modelling the grinding operation difficult. It can be stated however that abrasive grains generally have a large negative rake angle, which is around -60°. This large negative rake angle introduces a smaller shear angle and greater deformation of the produced chips, when compared to the orthogonal cutting model. A schematic two-dimensional model of a grinding operation is shown in Figure 52. The smaller shear angle and large negative rake angle consequently introduce a larger shear velocity, which can be derived from Figure 51b. This means that, for an equal shear force, the specific cutting energy for shearing, u_s, is higher in a grinding operation than in a cutting operation [30].

The second difference between orthogonal cutting and grinding is the introduction of a wear flat on the abrasive grain, which can be seen in Figure 52. Similar to a cutting tool without relief angle, the wear flat introduces a surface where friction takes place. A grinding operation thus involves three heat generation zones: the rake face, shear plane, and the wear flat. This causes a higher temperature rise than in a cutting operation where only the rake face and shear plane generate heat [39]. The energy dissipation due to friction caused by sliding introduces another component to the specific cutting energy, namely the specific sliding energy, $u_{sl}\ [J/m^3]$. Similar to the specific energies seen in the previous section, this is calculated by dividing the power by the volumetric removal rate. The sliding power, $P_{sl}\ [Nm/s]$, is the product of the tangential sliding force, $F_{sl}\ [N]$, and the parallel grain velocity, $V\ [m/s]$:

$$u_{sl} = \frac{P_{sl}}{Q} = \frac{F_{sl}V}{Q} \quad \left[\frac{J}{m^3}\right] \tag{7}$$

Where the tangential sliding force is given by:

$$F_{sl} = \mu p b l_c A \quad [N] \tag{8}$$

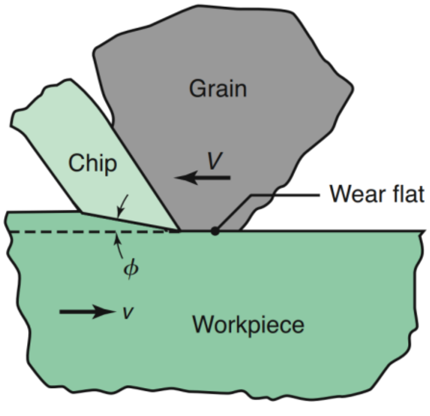

Figure 52: Schematic two-dimensional illustration of a grinding operation. (Figure adapted from Kalpakjian et al. [30]*).*

Where $\mu\ [-]$ is the friction coefficient, $p\ [N/m^2]$ is the average contact stress, $b\ [m]$ is the width of the grinding surface, $l_c\ [m]$ is the length of the cutting surface along the grinding tool, which is in contact with the workpiece, and $A\ [m^2]$ is the percentage of the grinding tool surface that is flat.

Another factor that influences the specific grinding energy in abrasive machining is ploughing. Ploughing introduces energy dissipation in the form of plastic deformation of the workpiece material. The amount of dissipated energy depends on the critical cutting depth, $h'[m]$, which is illustrated in Figure 53. When the abrasive grain comes in contact with the workpiece material, its depth of cut increases from zero to the maximum cutting depth, $h_m\ [m]$. If the depth of cut is between zero and $h'\ [m]$, the abrasive grain is unable to shear off material and pushes it forward and to the sides, similar to an agricultural plough. Logically, no material is removed from the workpiece in this stage. Material removal only happens when the critical cutting depth is reached and chip formation can take place. In order to keep a grinding operation as efficient as possible, it is important to decrease the critical cutting depth, which means that the abrasive grains are able to form chips more quickly. The critical cutting depth depends on several factors: Sharpness of the grain, the rake angle of the grain, and lastly the friction coefficient between the grain and the workpiece material. The friction coefficient is thus material dependent and can only be changed by using another type of grain for an equal workpiece. The grain geometry however can be influenced, a sharper grain with a smaller negative rake angle will have a lower critical cutting depth. Another way to minimise energy dissipation due to ploughing is to change process parameters, namely the length of the cutting path of the grain, and the radial infeed velocity, $v_f\ [m/s]$. Increasing the length a means that the cutting path of the grain becomes longer, while the length of the ploughing stage remains the same. In this way, the ploughing stage has become relatively shorter. Figure 53 shows a surface grinding operation, where $a\ [m]$ corresponds to the depth of cut. However, if a grinding wheel is used to drill a hole, $a\ [m]$ is equal to the diameter of the wheel. This means that a larger grinding wheel is more efficient with respect to ploughing, because increasing the wheel diameter increases $a\ [m]$. Increasing the infeed velocity means that the grinding wheel passes through the workpiece material faster. This means that the critical cutting depth is reached earlier. For an equal grain velocity, this means that the length of the ploughing stage decreases.

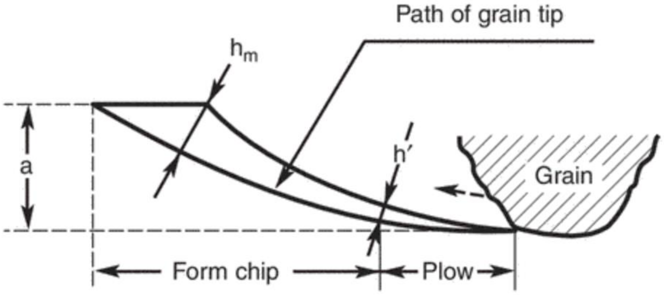

Figure 53: Schematic illustration of the critical cutting depth h'[m], which separates ploughing from chip formation. (Figure adapted from Kannappan et al. [40]*).*

The total specific energy for grinding thus includes the specific energy for cutting, which was derived in the previous section, with the addition of the components of sliding and ploughing [41]:

$$u_{total} = u_s + u_f + u_{sl} + u_{pl} \quad \left[\frac{J}{m^3}\right] \qquad (9)$$

The final difference between a cutting and a grinding tool is their number of wear mechanics. The main wear mechanism of a cutting tool is dulling of the cutting edge. A grinding wheel however, has three wear fundamentally different wear mechanisms, which are shown in Figure 54: Attritious wear, grain fracture, and bond fracture. Attritious wear is the dulling of an abrasive grain. Similar to dulling of a cutting edge, this introduces a wear flat, which increases the specific grinding energy. Grain fracture implies that a part of the abrasive grain breaks off. This introduces a new, sharp cutting surface. Bond fracture means that the connection between different grains fail. The underlying grains form a new grinding surface and come into contact with the workpiece. Where attritious wear increases the specific cutting, grain and bond fractures counteract this by introducing fresh cutting surfaces. A grinding wheel thus has self-sharpening wear mechanisms, at the expense of losing tool material.

Machining of Porous Material

To fully understand the orthogonal cutting and grinding mechanisms, the properties of the workpiece material needs to be considered as well. In this research, the workpiece material is cancellous bone with its characteristic porous structure. A render of human cancellous bone is shown in Figure 55. The previous sections have shown the different components that comprise the specific cutting and grinding energy. In these models the workpiece material was assumed to be solid and homogenous. Speculating how the cutting, sliding, and ploughing components of the specific energies are influenced by introducing a porous workpiece material, can give more insight in the machining of cancellous bone.

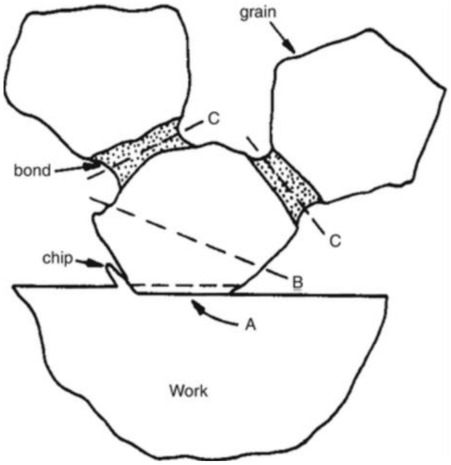

Figure 54: Schematic two-dimensional illustration of different wheel wear mechanisms. A: Attritious wear. B: Abrasive grain fracture. C: Bond fracture (Figure adapted from Malkin. [27]*).*

For the cutting component, a porous workpiece material means that larger pieces of material may break off, besides the normal chip formation. When cancellous bone is cut, the porous structure is compromised. This means that the pillars, or trabecula, at the surface are no longer supported on all sides. It is hypothesised that the cutting tool could break the pillars at their base due to the applied force, instead of cleanly cutting off. Because more material is removed for the same operation, the specific cutting energy decreases for a porous material. Another point to consider, when introducing a porous workpiece material, is that the produced chips can be contained in the cavities of the material and do not need to be removed from the hole. The extent to which this is possible depends on the porosity of the material, which is 30 – 90% in case of cancellous bone.

For the ploughing component, introducing a porous workpiece material might mean that the critical cutting depth is reached earlier. This effect can be explained by comparing up grinding to down grinding. Figure 56 shows the difference between the two grinding types: In up grinding, the abrasive grain starts with zero depth of cut and gradually reaches the critical cutting depth. As seen in Figure 53, ploughing occurs before this cutting depth is reached, resulting in the pile up in front of the abrasive grain. In down grinding, on the other hand, the abrasive grain starts out with its maximum cutting depth, because the grain suddenly comes into contact with the top of the workpiece. When the grain starts with its maximum cutting depth, the ploughing stage is skipped, which results in a lower specific grinding energy [42]. This could also occur when grinding cancellous bone, because the cavities allow the abrasive grains to gain cutting depth, before they come into contact with the trabecular pillars.

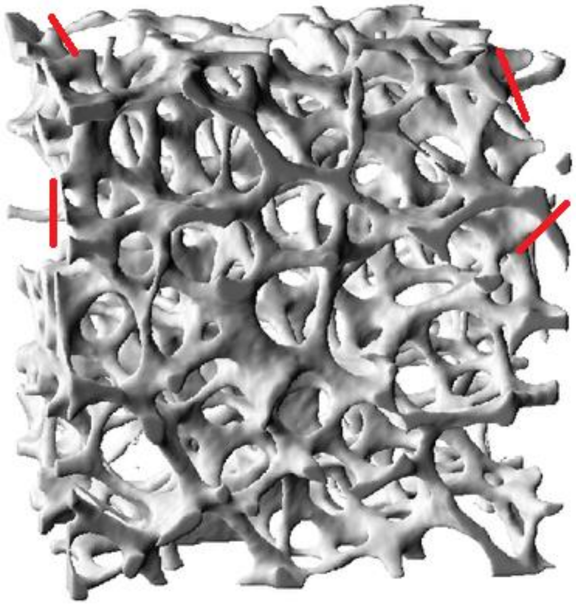

Figure 55: A render of human cancellous bone. The trabecular pillars are approximately 0.1 mm wide, with a mean intertrabecular distance in the range of 1 mm [5]. The red lines indicate a few locations where unsupported pillars can break off. The material is porous enough such that the produced chips can be contained within the cavities. (Figure adapted from Stauber et al. [43]*).*

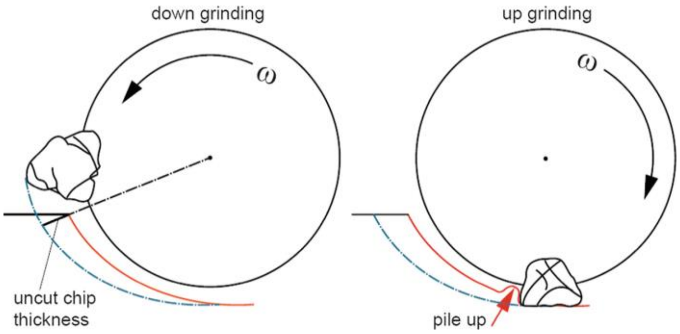

Figure 56: Down grinding (left) compared to up grinding (right). The red lines show the surface of the workpiece material. The blue lines show the path of the abrasive grain through the material. (Figure taken from Wegener. [42]*).*

As for the sliding component, the length and width of the cutting surface decrease due to the porous structure. This logically means that the heat generated by sliding also decreases, compared to a similar volumetric amount of solid material. To summarise, the specific cutting, ploughing, and sliding energies all seem to decrease when a porous workpiece material is introduced.

APPENDIX II: TESTING A SELECTION OF ROTARY TOOL ACCESSORIES

Method

Goal of the experiment

The goal of this experiment is to discover which conventional cutting tool material works best in combination with cancellous bone. For this experiment, a wide range of cutting tool materials was tested on polyurethane foam, which was used as a cancellous bone phantom. The two aspects that were considered are the amount of material that is removed per unit of time, and the amount of heat that is generated as a result. The most suitable cutting tool material is capable of a high material removal rate, with minimal heat generation.

Independent and dependent variables

The independent variables of the setup are the cutting tool material, the cutting speed, and the applied force on the cutting tool. The cutting tool material is varied by the use of the different cutters. A wide range of cutting tool materials was tested. To keep the experimental setup as simple as possible, it is desirable that all cutting tools are compatible with the same piece of equipment, so the only change in the setup between experiments is the cutting tool. For this reason, a Dremel rotary multitool was chosen, along with its compatible cutting tools. The chosen rotary tools are shown in Figure 57, and span the entire Dremel collection: One example of each cutting tool material was chosen for this experiment. Table 2 shows the intended workpiece materials per cutting tool material. In this table, a distinction is made between hard and soft metals. Hard metals include hardened steel, stainless steel, and cast iron. Soft metals include aluminium and copper. The tools can be divided into two groups: One group with clearly defined cutting edges, and one group with abrasive particles. The group with cutting edges consists of two cutting tools: One is made out of high speed steel (HSS), and one is made out of the much harder tungsten carbide. The group with particles consists of four different types of abrasive grains: diamond, structured tungsten carbide, aluminium oxide, and silicon carbide. Two different tools of aluminium oxide were tested: one in the form of a grinding stone, and one in the form of 60 grit sandpaper. The main difference between the two is the size of the abrasive grains, which is much larger in case of the sandpaper.

To compare the different cutting tools, both the cutting speed with respect to the workpiece, and the applied force need to be equal throughout the experiment. As can be seen in Figure 57, the different cutting tools are not available in the same diameter. To compensate for this, the rotations per minute (rpm) of the Dremel tool were set to be inversely proportional to the cutting tool diameter, which ensures that the velocity of the outer surface of each cutting tool is equal. The smallest cutting tool was set to the highest rpm setting of the Dremel tool, because the machine tends to stutter on the lowest rpm setting. Table 3 shows the required rpm setting for each cutting tool.

The dependent variables are the material removal rate, and the generated heat [°C]. The material removal rate $[g/s]$ is calculated by dividing the difference in weight, before and after a cut, by the amount of time it took to make that cut. In this way, the material removal rate is not influenced by the diameter of the cutting tool, or air gaps in the polyurethane foam. The generated heat is measured off of the polyurethane foam, closely to the path that was cut.

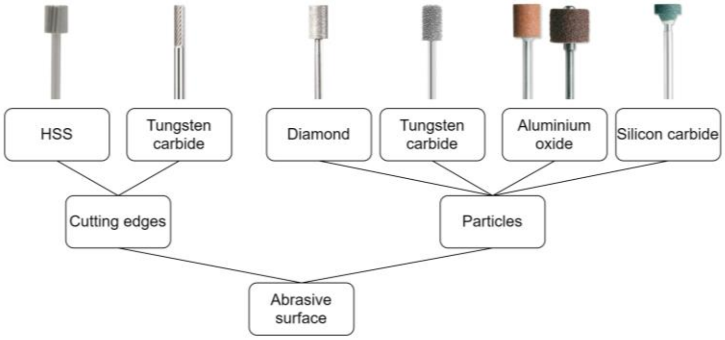

Figure 57: An overview of the selected Dremel cutting rotary tool accessories [33].

Table 3: The required rpm for an equal cutting speed for each cutting tool.

Cutting tool	***Tool diameter (mm)***	***rpm for equal cutting velocity***
HSS	7.8	14,400
Tungsten carbide	3.2	35,000
Diamond	3.2	35,000
Tungsten carbide structured	19	5,900
Aluminium oxide	9.5	11,800
Aluminium oxide sanding	13	8,600
Silicon carbide	9.5	11,800

Table 2: The intended workpiece materials for each cutting tool material [33].

	Hard metals	**Soft metals**	**Ceramics**	**Glass**	**Wood**	**Plastic**	**Stone**
HSS		x			x	x	
Tungsten carbide	x	x	x		x	x	
Diamond	x		x	x	x		x
Structured tungsten carbide			x		x	x	
Aluminium oxide	x						
Aluminium oxide sanding					x	x	
Silicon carbide		x					x

Test setup

Polyurethane foam is used as workpiece material, because both the compression strength and Young's modulus can be made to match those of cancellous bone, which makes it suitable to use as a mechanical bone phantom [44]. Polyurethane foam is also easier to experiment with compared to cadaver bones, because it does not degrade over time, and because it is not bound to strict regulations [45].

Polyurethane foam bone phantoms can be either bought from a commercial supplier, or they can be made. The downside of buying a phantom is that it comes with long delivery times. The cutting tool experiment was meant to quickly provide insight in which cutting surface material should be used in the vertebral drilling device. It is a comparative experiment, so even if the mechanical properties of the phantom are slightly off, it can still provide useful information on the performance of the cutting tools relative to each other. For these reasons, the decision was made to make the polyurethane samples. A store bought two component mixture, which consists of a fixed ratio of isocyanate and polyol, was used to create a block of foam of approximately 30 x 20 x 15 cm. The large block was cut into smaller samples of about 7 x 5 x 4 cm that were used for the experiment. Figure 58 shows one of the smaller blocks of polyurethane.

The mechanical properties of the polyurethane samples were validated according to the NEN-ISO 13314 compression test protocol [46]. Adult cancellous bone has a compressive strength, which is defined as the first maximum of the stress-strain curve, of 0.6 – 6.2 MPa, with a mean of 2.4 MPa [47]. The compression test has shown however, that the polyurethane foam had an average compressive strength of 0.025 MPa. Figure 59 shows the stress-strain curves found in the compression test, in which four cylindrical samples of 15 x 30 mm were used. This means that the compressive strength of the polyurethane samples is roughly an order of magnitude smaller than that of real cancellous bone. Furthermore, the foam is not completely homogenous, instead it has some larger air gaps. These gaps are however few in number and relatively small, so they can be avoided in the experiment. The average pore size of the foam is in the range of 1 mm, which corresponds to the intertrabecular space of cancellous bone [5].

Figure 58: One of the blocks of polyurethane used as a cancellous bone phantom.

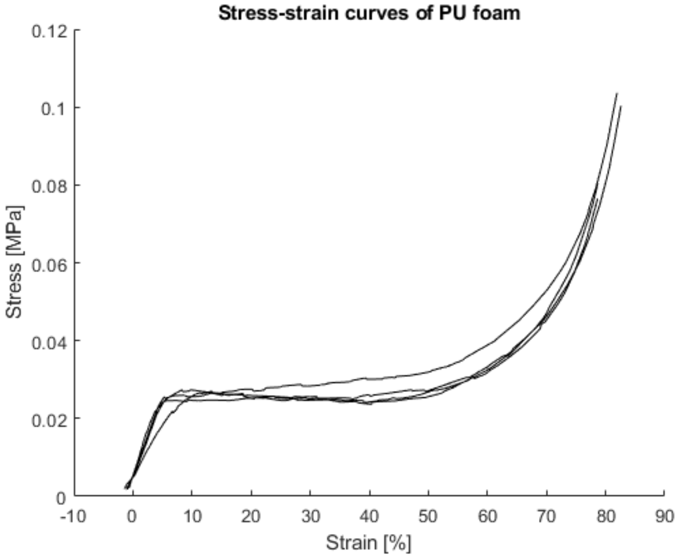

Figure 59: Stress-strain curves of four polyurethane foam test samples, tested according to the NEN-ISO 13314 compression test protocol [46].

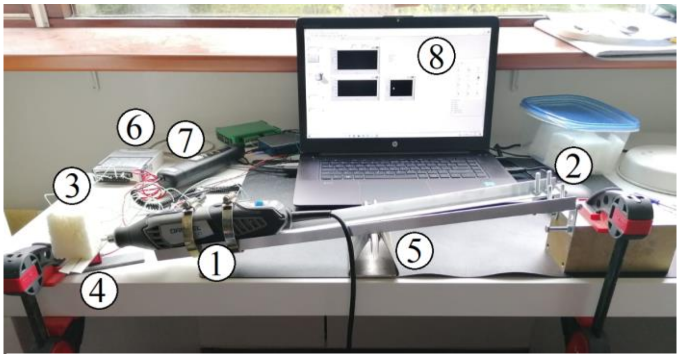

Figure 60: The test setup, consisting of: 1) a Dremel 4000; 2) a lever which is hinged to the desk; 3) a block of polyurethane foam; 4) a load sensor; 5) a stop block; 6) three thermocouples; 7) a tachometer; and 8) a laptop with LabVIEW 2018.

The experimental setup is designed to cut a straight path downwards into a block of polyurethane foam, and is shown in Figure 60. The Dremel tool (1) is connected to a lever arm which is hinged to the desk (2), this allows the cutting tool to move up and down. Because the lever arm is relatively long compared to the angular displacement, the path of the cutting tool is assumed to be straight. This ensures that the applied force is constant throughout the experiment, because it is generated by gravity. A block of polyurethane foam (3) is placed upon the load sensor (4), which is used to measure the time it takes for the cutting tool to cut a path through the block of foam. As soon as the cutting tool comes into contact with the block, the applied force is registered. A stop block (5) is placed under the lever arm to make sure the Dremel does not cut into the load sensor. Because it restricts the lever arm from moving further downwards, the applied force is no longer registered by the load sensor. The time it takes for the cutting tool to cut its path is thus equal to the time that the load sensor is under pressure. Three thermocouples (6) are placed into the block of foam along the cutting path to measure the generated heat. A tachometer (7) is used to validate the cutting speed of the Dremel, because the dial on the machine itself cannot be read precisely. Finally, the data from the load sensor, tachometer, and thermocouples is collected on a laptop with LabVIEW 2018 (8).

Test protocol

The experiment was prepared by mounting one of the different cutting tools into the Dremel tool. As stated before, the tachometer was used to precisely reach the corresponding rpm setting, as shown in Table 3. The following sequence was repeated three times per cutting tool, so 21 times in total:

1) The weight of a block of polyurethane foam was measured using a Kern PCB 100-3 scale, before it was placed upon the load sensor. The scale is capable of measuring a difference as small as a milligram. Such high precision is required, as the foam is relatively light.
2) The three thermocouples were placed into the foam along the path that was about to be cut. The generated heat was thus measured at the beginning, in the middle, and at the end of the path. Great care must be taken to ensure the thermocouples were not placed in the cutting path.
3) Right before the cut was made, the LabVIEW file was started, monitoring the thermocouples and the load sensor. Figure 61a shows the experimental setup at this point.
4) The Dremel tool was turned on and lowered into the block of foam. The Dremel should not be held during cutting, to ensure that the applied force on the workpiece is equal to gravity and thus equal throughout the experiment.
5) Once the Dremel tool had made the cut and was stopped by the stop block, the tool was turned off immediately, otherwise it would have continued to generate heat.
6) The LabVIEW file should be stopped approximately 10 seconds after turning off the Dremel tool, because the generated heat takes time to reach the thermocouples. After the graphs of the thermocouples had reached their highest point, meaning that the heat had reached the thermocouples, the LabVIEW file was stopped. Figure 61b shows the experimental setup at this point.
7) The block of foam was removed from the load sensor, the loose particles were tapped off, and the block was weighed again. The difference in weight was noted.

The blocks of polyurethane foam were used multiple times: Cuts were made along the front and back of the blocks. Depending on the depth of those cuts, a slice could be cut off with a knife, revealing a fresh surface to test on. Depending on the size of the cutters, one block was used six to nine times.

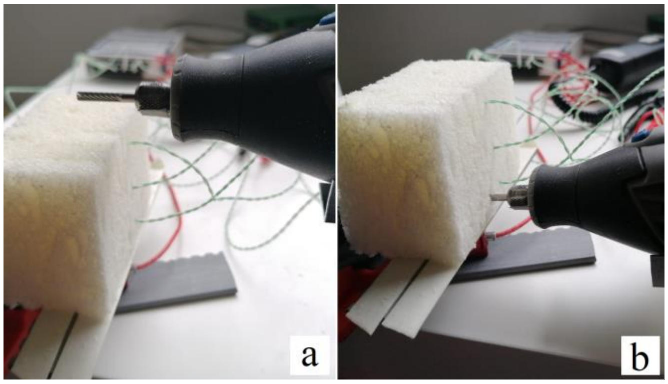

Figure 61: The experimental setup right before (a) and right after (b) the cut was made. The thermocouples are the three green wires, and the load sensor is connected to the red wire.

Data analysis

The time to make the cut is taken from the load sensor data. This is done by measuring the time that the load sensor is under pressure from the cutting tool. Together with the difference in weight, the material removal rate $[g/s]$ is calculated.

Results

Material removal

The removed mass per unit of time is shown for each cutting tool in Figure 62. It is clear that the three cutting tool materials, that were not suitable to be used on plastic according to Table 2, have the lowest material removal rate. Aluminium oxide, silicon carbide, and diamond particles remove almost no mass from the workpiece. They were however capable of moving through the material, be it without chip formation. The three metal cutting tools: HSS, tungsten carbide, and structured tungsten carbide perform equally, with a material removal rate of approximately 0.012 g/s. This makes sense, because the cutting tool material is significantly harder than the polyurethane foam. The difference in hardness between HSS and tungsten carbide does not cause a notable difference in performance. The cutting tool with the highest material removal is aluminium oxide sanding paper. It must be stated that this result is questionable, because this tool did not seem to cleanly cut into the foam. Due to the relatively large and coarse grains, it seemed to rip off whole pieces of material instead of producing chips. This effect could cause the sanding paper to remove relatively more material per unit of time.

Generated heat

The third thermocouple, at the end of the cutting path, consistently measured the highest temperature for all cutting tools. This makes sense, because more heat is generated as the cutting tool moves through the workpiece. The measured maximum temperatures of the third thermocouple are shown in Figure 63 for each cutting bit. It needs to be stated that the distance from the thermocouples to the cutting path is critical, for a small difference has a large influence on the measured temperature. This is why the error bars are relatively large. As can be expected, the cutters that removed the least amount of material: aluminium oxide and silicon carbide, generate the most heat. As stated before in Appendix I, more heat is generated in a grinding operation due to the number of heat affected zones, and because of ploughing. The remaining cutters are able to cut through the workpiece without generating a significant amount of heat.

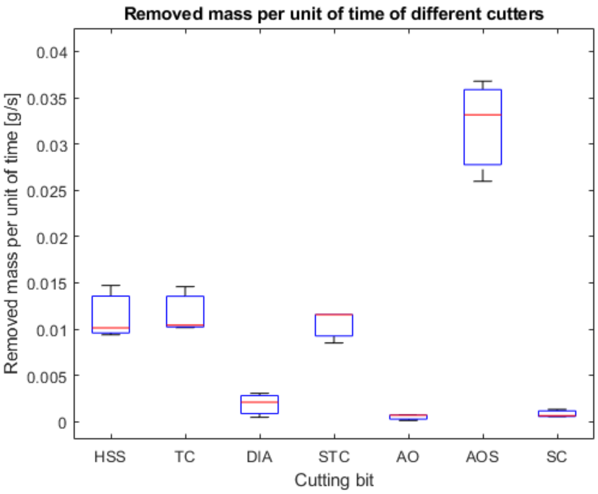

Figure 62: The material removal rate [g/s] of the different cutters.

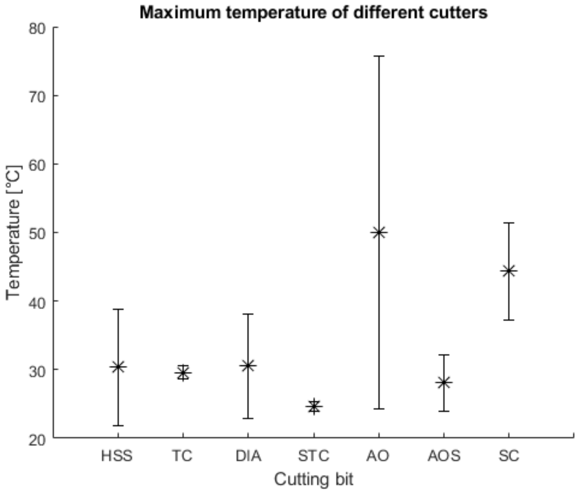

Figure 63: The maximum measured temperatures at the end of the cutting path for each cutting bit. The asterisks indicate the mean temperature, and the error bars show one standard deviation.

Conclusion

To conclude this experiment, HSS, tungsten carbide, structured tungsten carbide, and aluminium oxide sanding paper can be considered as cutting tool material for the vertebral drilling device. These materials are able to effectively remove material without significant heat generation. The remaining three materials: diamond, aluminium oxide, and silicon carbide are not suitable, because they are unable to remove material through chip formation, and because an excessive amount of heat is generated.

APPENDIX III: PROTOTYPE DIMENSIONIG CALCULATIONS

Dimensioning of the cutting head

The necessary rotation of the cutting head can be calculated as follows, if the diameter and desired teeth travel are known. This calculation is illustrated by Figure 64.

$$Necessary\ rotation = \frac{Teeth\ travel * 360°}{Tool\ circumference}$$

$$= \frac{2\ mm * 360°}{\pi * 7.9\ mm} = 30°$$

Transmission ratio

The length of the oscillating arm, y, can be calculated as follows, if the distance between the pins in the cutting head, the rotation of the cutting head, and the rotation of the oscillating input are known. This calculation is illustrated by Figure 65.

$$y = \frac{Pin\ distance * \sin\ (Cutting\ head\ angle)}{\sin\ (Oscillation\ angle)}$$

$$= \frac{4\ mm * \sin\ (30°)}{\sin\ (2.8°)} = 41\ mm$$

Number of pins for buckling prevention

The maximum allowable distance between the leaf springs are calculated in the hypothetical case that the cutting head is fixed. The leaf springs are thus subjected to the full force of the actuator. This applied force can be calculated if the power of the actuator, the speed of the actuator, and the arm length, y, are known.

$$P = T * rpm/60 \qquad [49]$$

$$P = F * y * rpm/60$$

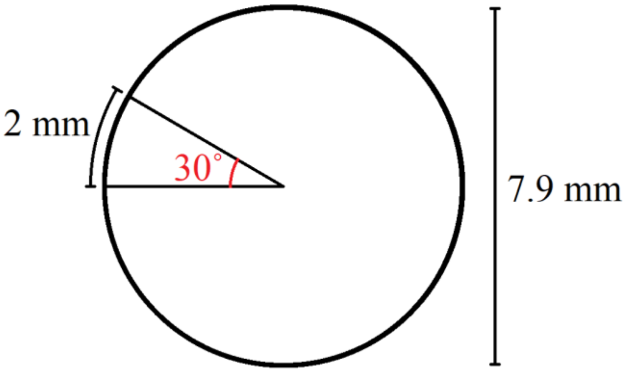

Figure 64: In case of a cutting head with a diameter of 7.9 mm, a rotation of 30° is necessary for 2 mm of travel along the circumference.

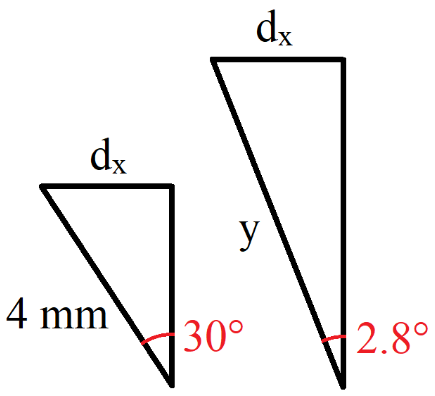

Figure 65: The necessary arm length y can be calculated with the fact that the horizontal displacement d_x of the cutting head (left) and the oscillating arm (right) must be equal.

$$F = \frac{60 * P}{y * rpm} = \frac{60 * 300\ W}{0.041\ m * 22{,}000\ rpm} = 19.96\ N$$

The leaf spring length at which buckling occurs can be calculated with the following formula:

$$F = \frac{n * \pi^2 * E * I}{L^2}$$

The factor accounting for the end conditions, n, was chosen to be 4, because the pins in the leaf springs and the cutting head keep the leaf springs parallel to each other. The different values for n, and the corresponding end conditions are shown in Figure 66. Rewriting the formula for L yields:

$$L = \sqrt{\frac{n * \pi^2 * E * I}{F}}$$

$$L = \sqrt{\frac{4 * \pi^2 * 190 * 10^9 * \frac{1}{12} * 0.006 * 0.0002^3}{19.96}}$$

$$= 0.039\ m$$

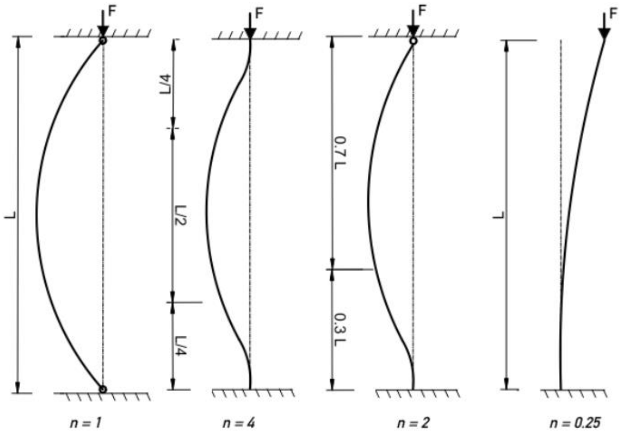

Figure 66: The different end conditions of Euler's buckling formula [50].

Rotation of the cutting head due to bending

The rotation of the cutting head due to bending of the transmission can be calculated if the leaf spring length, L, thickness, and angle are known. The angular displacement of the cutting head is calculated in case the inner leaf spring is bent 90°, which is shown in Figure 67. The radius r_1 is equal to:

$$r_1 = \frac{L * 4}{2 * \pi} \approx 70.02817496\, mm$$

The radius r_2 is one leaf spring thickness larger than r_1:

$$r_2 = r_1 + 0.2\, mm \approx 70.22817496\, mm$$

Deflection of the outer leaf spring A, the angle α, is calculated as follows:

$$\alpha = \frac{360° * \mathrm{L}}{2 * \pi * r_2} \approx 89.74369261°$$

The horizontal distance from the base of the inner leaf spring to point B is equal to its radius, because of the 90° bend:

$$B_x = r_1 \approx 70.02817496\, mm$$

The parameters L, r_2 and α were put into a sketch in Solidworks to find the horizontal distance from the base of the inner leaf spring to point A:

$$A_x \approx 69.71401674\, mm$$

Difference between the ends of the two leaf springs is thus:

$$d_x = B_x - A_x \approx 0.31415822\, mm$$

This results in the following rotation of the cutting head:

$$\theta = \sin^{-1}\left(\frac{d_x}{Pin\ distance}\right) \approx 4.504624246°$$

$$\theta \leq 15°$$

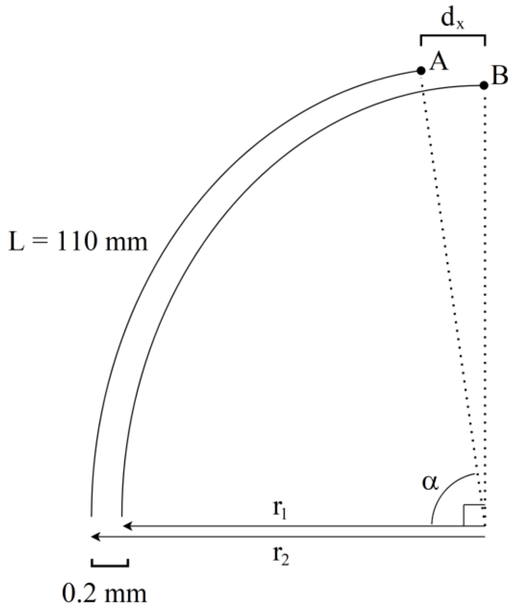

Figure 67: A sketch of the two leaf springs when the device is bent 90°. Because the leaf springs are side by side and the same length, the end of the outer spring (A), lags behind the end of the inner spring (B). The horizontal distance between these points (d_x) determines the offset of the cutting head.

APPENDIX IV: PROTOTYPE FAILURE AND SECOND ITERATION

Prototype failure

The first iteration of the prototype failed during the straight trajectory drilling test. The connection between the leaf springs and the pins in the cutting head proved to be too fragile. Figure 68 shows the first iteration of the prototype right after the leaf spring broke, the cutting head can be seen hanging on one pin. Figure 69 shows close ups at the site where the leaf spring fractured. Damage at the side of the leaf spring below the pin hole, indicated by the red arrow, likely means that the two parts bumped into each other during oscillation. This weakened the leaf spring near the pin hole, and caused a crack to propagate from left to right. This becomes evident when the fracture surfaces are closely examined. The irregular surface at the left side of the pin hole indicates a ductile fracture, while the cleaner surface on the right indicates a brittle fracture.

Figure 68: The first iteration of the prototype after failure during the straight trajectory drilling test.

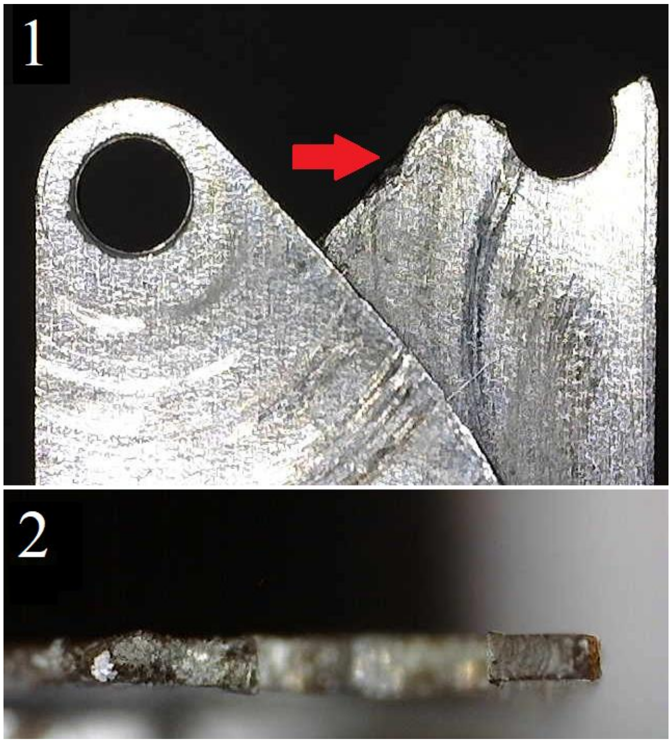

Figure 69: A side and a top view of the fracture site of the leaf spring. 1) The damage to the side of the leaf spring, which weakened the pin hole, is indicated by the red arrow. 2) The surfaces left and right of the pin hole indicate ductile and brittle fractures, meaning the cracks propagated from left to right.

Second iteration

Two improvements were made to prevent failure of the pin holes in the leaf springs: The leaf spring thickness was increased from 0.2 mm to 0.3 mm, and the width of the material around the pin hole was increased from 0.5 mm to 1 mm. The increased width and thickness logically strengthen the material around the pinhole, but also prevent the two leaf springs from damaging each other during oscillation. Figure 70 shows a side view of the old (dark blue) and new (light blue) leaf springs on top of each other. The increase in width around the pin hole required a larger slot in the cutting head.

Rotation of cutting head due to bending

Because the thickness of the leaf springs is increased, the rotation of the cutting head due to bending of the transmission also increases. The calculations of Appendix III should thus be repeated to verify if the second iteration of the device is able to cut in a bent state:

$$r_1 = \frac{L * 4}{2 * \pi} \approx 70.02817496\,mm$$

$$r_2 = r_1 + 0.3\,mm \approx 70.32817496\,mm$$

Deflection of the outer leaf spring A:

$$\alpha = \frac{360° * \mathrm{L}}{2 * \pi * r_2} \approx 89.61608559°$$

$$B_x = r_1 \approx 70.02817496\,mm$$

$$A_x \approx 69.55693959\,mm$$

Difference between the ends of the two leaf springs:

$$d_x = B_x - A_x \approx 0.47123537\,mm$$

Resulting rotation of the cutting head:

$$\theta = \sin^{-1}\left(\frac{d_x}{Pin\ distance}\right) \approx 6.765661465°$$

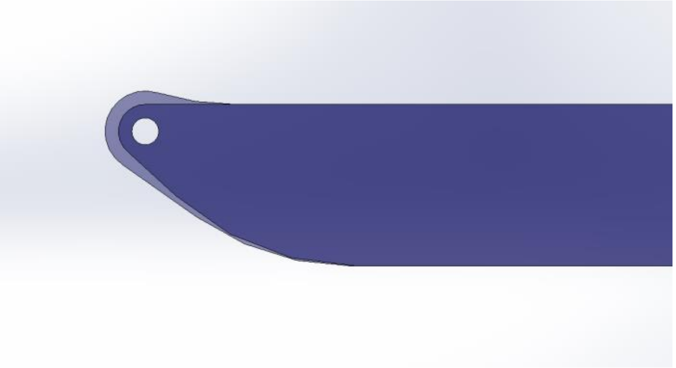

Figure 70: The first iteration of the leaf spring (dark blue) atop of the second iteration (light blue) shows the increase in material around the pin hole.

Because the slot in the cutting head is cut in deeper, the effective diameter of the cutting head is reduced in the neutral position. This is shown in Figure 71. The fact that the resulting rotation of the cutting head, θ, is smaller than 15° does not necessarily guarantee that the whole front face of the device is able to cut. The easiest way is to visually verify this, when the cutting head is in its outer position, while taking into account the resulting rotation, θ. The maximum rotation angle, with respect to the neutral position when bent 90°, is thus:

$$\theta_{max} = 15° - 6.765661465° = 8.234338535°$$

Figure 71 shows that the teeth in front of the slot are still higher than the highest point of the leaf spring. To conclude, a 90° bend should not hinder the cutting capabilities of the device.

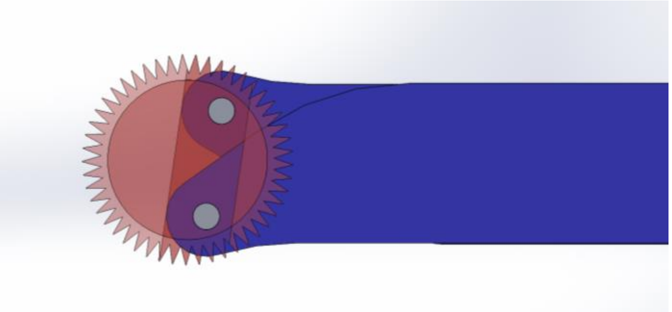

Figure 71: The cutting head in its maximum clockwise rotation in case the transmission is bent 90°. The cutting teeth in front of the slot are still higher than the leaf springs.

APPENDIX V: CAD DRAWINGS

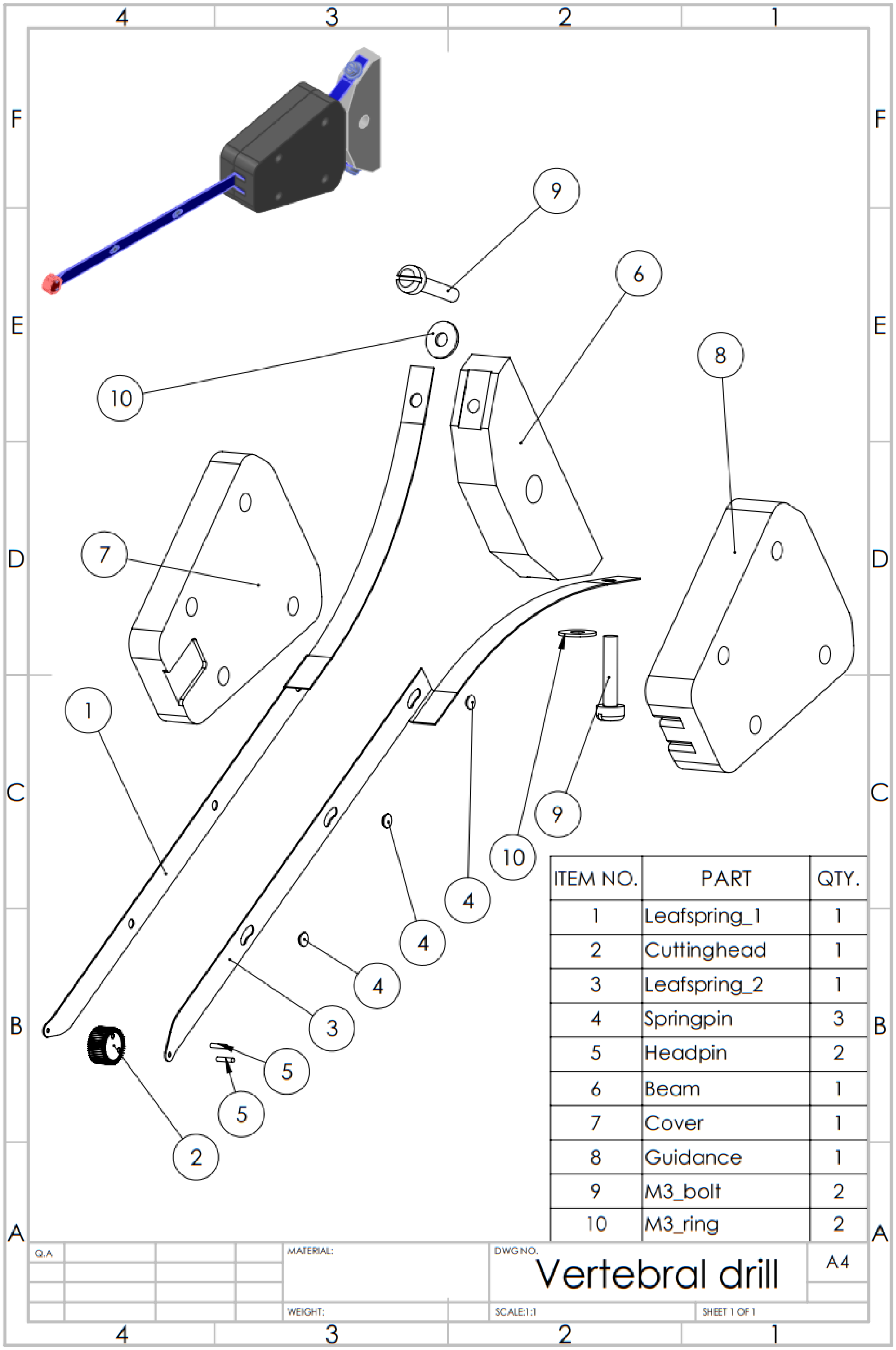

ITEM NO.	PART	QTY.
1	Leafspring_1	1
2	Cuttinghead	1
3	Leafspring_2	1
4	Springpin	3
5	Headpin	2
6	Beam	1
7	Cover	1
8	Guidance	1
9	M3_bolt	2
10	M3_ring	2

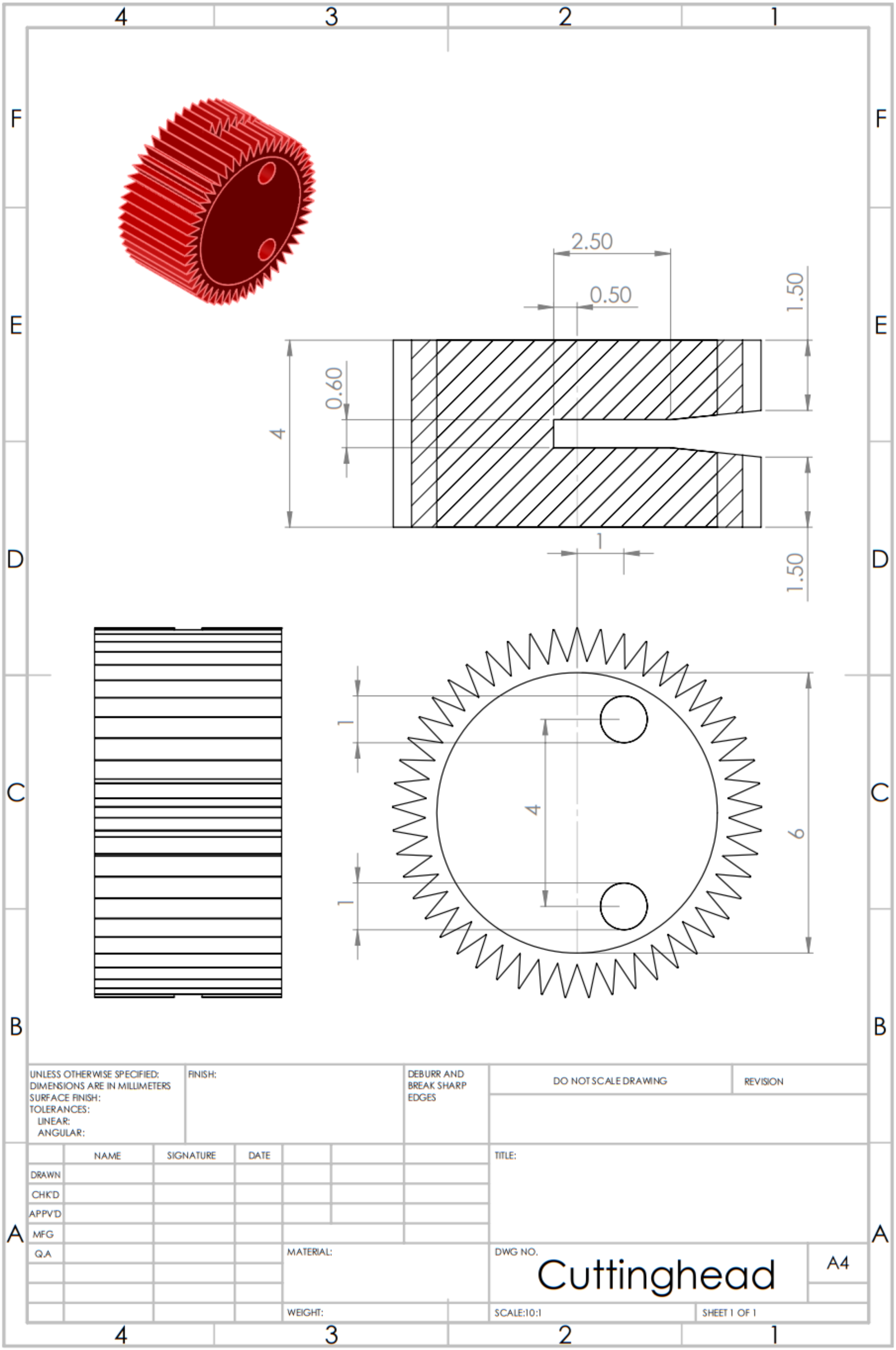
4
3
2
1
F
E
D
C
B
A
2.50
0.50
1.50
0.60
4
1
1.50
1
4
6
1
UNLESS OTHERWISE SPECIFIED:
DIMENSIONS ARE IN MILLIMETERS
SURFACE FINISH:
TOLERANCES:
LINEAR:
ANGULAR:
FINISH:
DEBURR AND BREAK SHARP EDGES
DO NOT SCALE DRAWING
REVISION
NAME
SIGNATURE
DATE
DRAWN
CHK'D
APPV'D
MFG
Q.A
TITLE:
MATERIAL:
DWG NO.
Cuttinghead
A4
WEIGHT:
SCALE:10:1
SHEET 1 OF 1

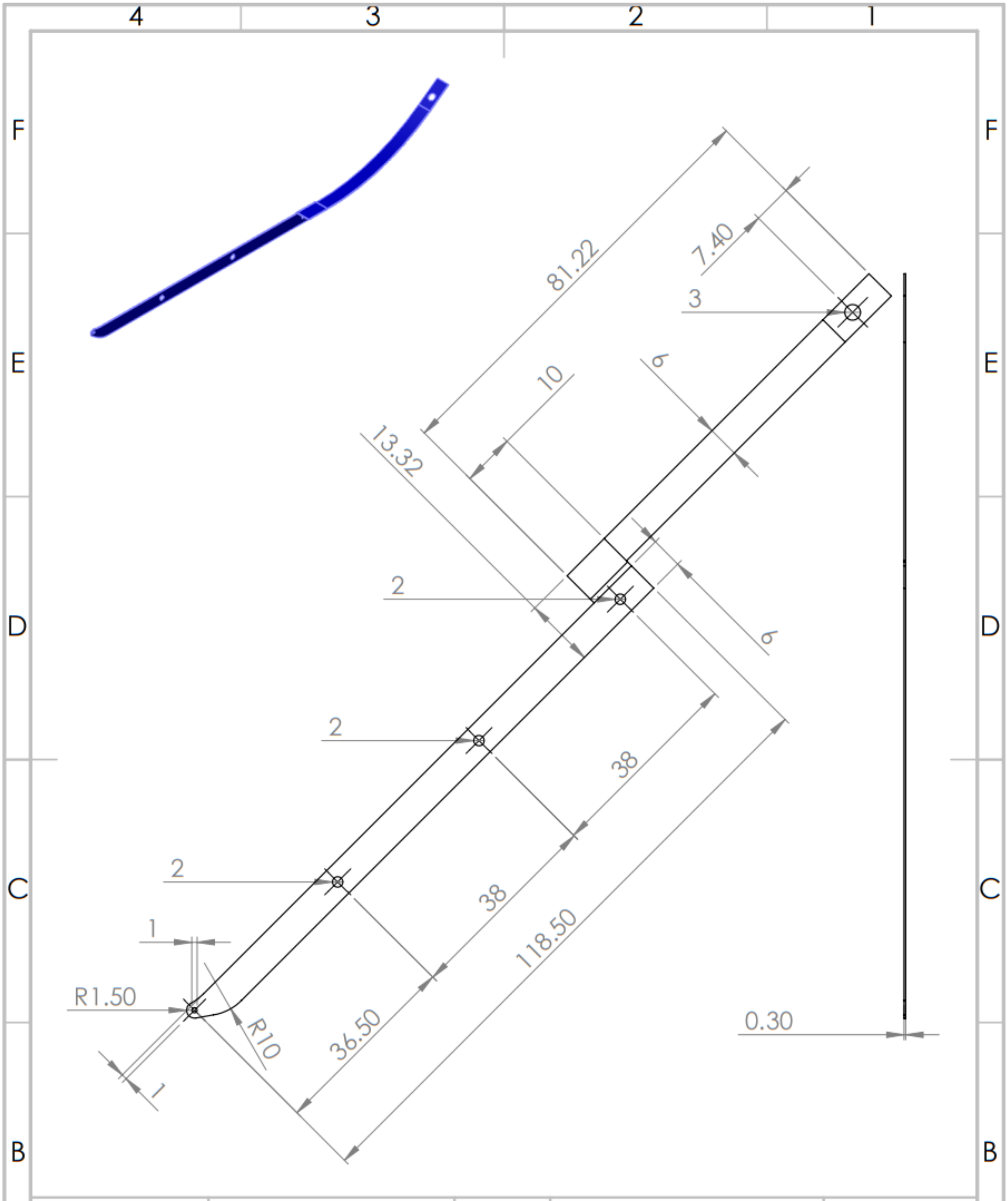

UNLESS OTHERWISE SPECIFIED:
DIMENSIONS ARE IN MILLIMETERS
SURFACE FINISH:
TOLERANCES:
LINEAR:
ANGULAR:

FINISH:

DEBURR AND BREAK SHARP EDGES

DO NOT SCALE DRAWING

REVISION

	NAME	SIGNATURE	DATE
DRAWN			
CHK'D			
APPV'D			
MFG			
Q.A			

TITLE:

MATERIAL:

DWG NO.

Leafspring 1

A4

WEIGHT:

SCALE:1:1

SHEET 1 OF 1

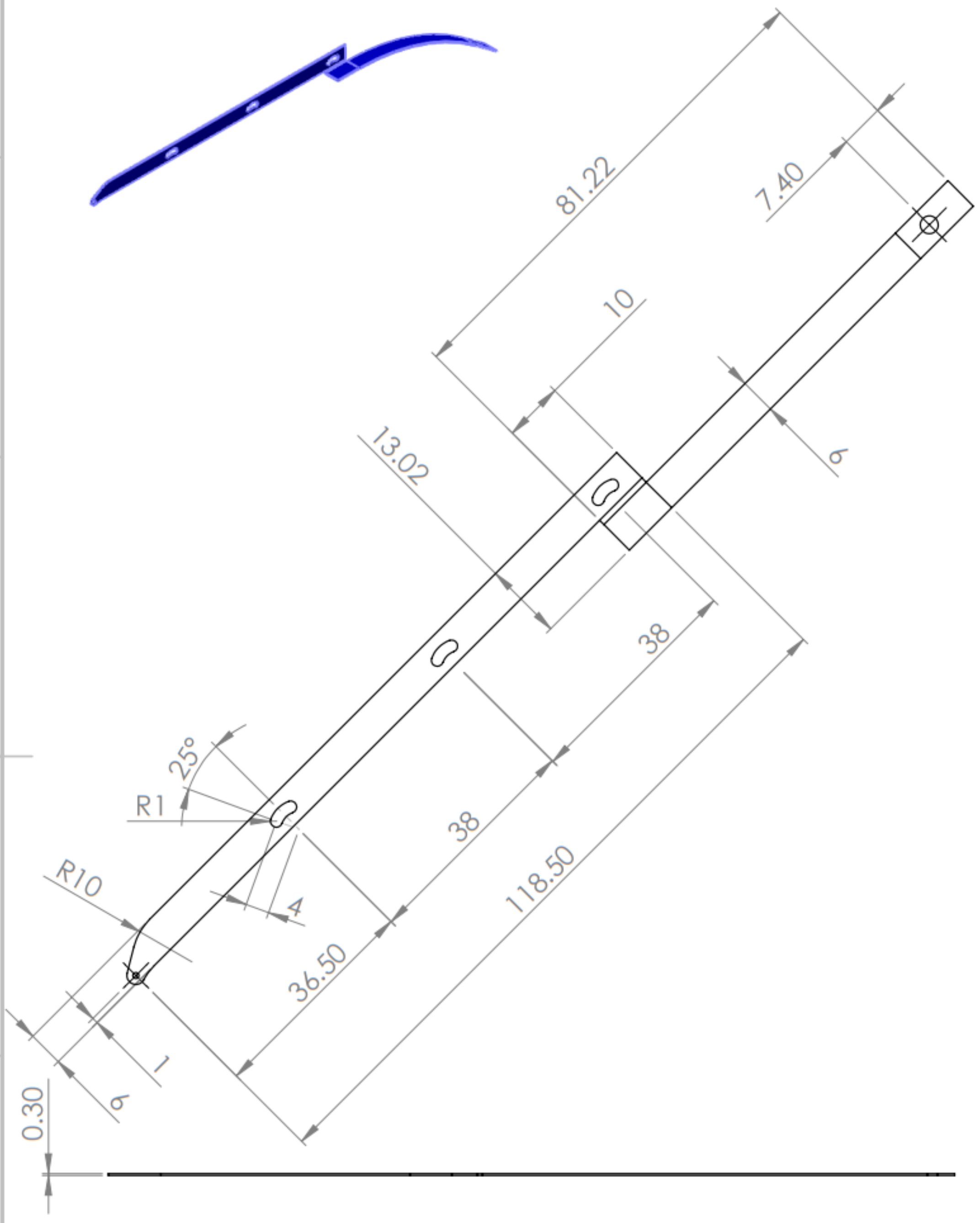

UNLESS OTHERWISE SPECIFIED:
DIMENSIONS ARE IN MILLIMETERS
SURFACE FINISH:
TOLERANCES:
LINEAR:
ANGULAR:

FINISH:

DEBURR AND
BREAK SHARP
EDGES

DO NOT SCALE DRAWING

REVISION

	NAME	SIGNATURE	DATE
DRAWN			
CHK'D			
APPV'D			
MFG			
Q.A			

TITLE:

MATERIAL:

WEIGHT:

DWG NO.

Leafspring 2

A4

SCALE:1:2

SHEET 1 OF 1

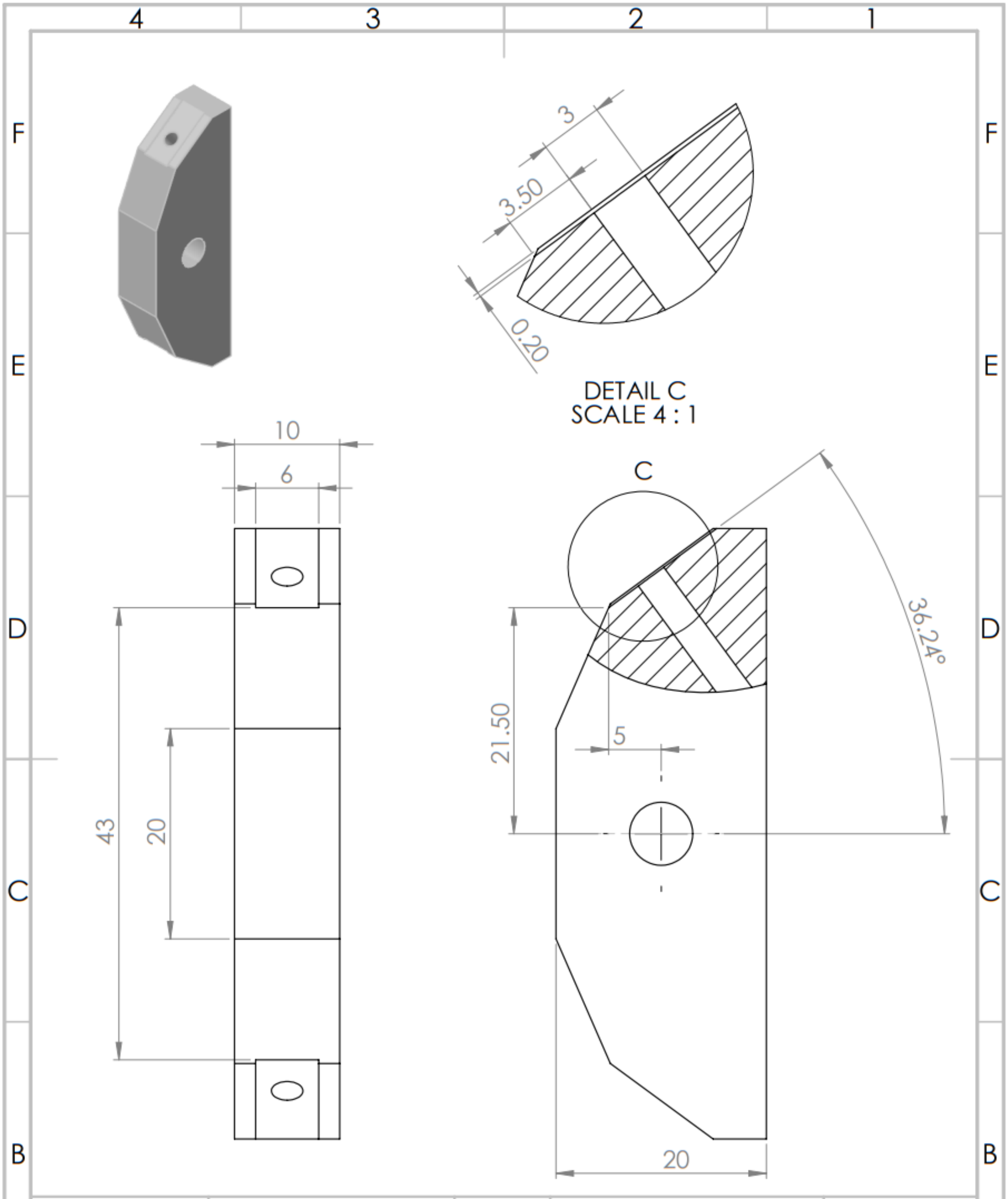

UNLESS OTHERWISE SPECIFIED:
DIMENSIONS ARE IN MILLIMETERS
SURFACE FINISH:
TOLERANCES:
LINEAR:
ANGULAR:

FINISH:

DEBURR AND
BREAK SHARP
EDGES

DO NOT SCALE DRAWING

REVISION

	NAME	SIGNATURE	DATE
DRAWN			
CHK'D			
APPV'D			
MFG			
Q.A			

TITLE:

MATERIAL:

WEIGHT:

DWG NO.

Beam

A4

SCALE:2:1

SHEET 1 OF 1

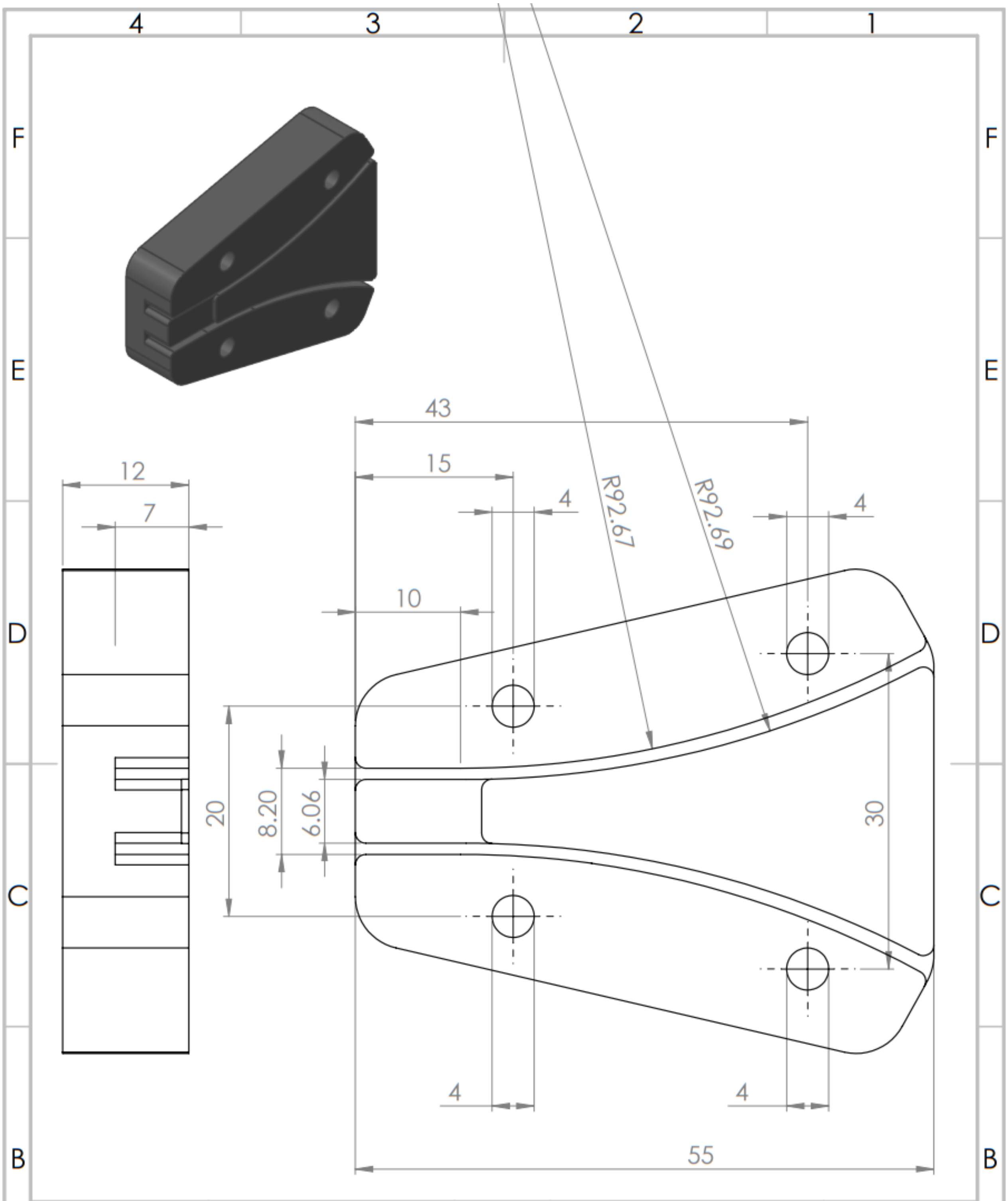

UNLESS OTHERWISE SPECIFIED:
DIMENSIONS ARE IN MILLIMETERS
SURFACE FINISH:
TOLERANCES:
LINEAR:
ANGULAR:

FINISH:

DEBURR AND
BREAK SHARP
EDGES

DO NOT SCALE DRAWING

REVISION

	NAME	SIGNATURE	DATE
DRAWN			
CHK'D			
APPV'D			
MFG			
Q.A			

MATERIAL:

WEIGHT:

TITLE:

DWG NO.

Guidance

A4

SCALE:2:1

SHEET 1 OF 1

APPENDIX VI: EXPERIMENTAL DATA

This Appendix shows the experimental data that were written down by hand. This includes the measured forces in the bending and buckling tests, and the weights of the foam blocks before and after each cut. For the load cell and thermocouple data collected with LabVIEW, the corresponding MATLAB files, or other questions about this research, an e-mail can be sent to: *robmuller18@gmail.com*

Experiment 1: Static deflection 0.2 mm

Deflection [mm]	*Force [N]*		
	Test 1	*Test 2*	*Test 3*
0	0	0	0
5	0.01	0.01	0.01
10	0.03	0.02	0.02
15	0.04	0.04	0.04
20	0.05	0.05	0.05
25	0.06	0.06	0.06
30	0.07	0.07	0.08
35	0.08	0.08	0.09
40	0.09	0.09	0.10
45	0.09	0.09	0.10
50	0.10	0.11	0.11

Experiment 1: Static deflection 0.3 mm

Deflection [mm]	*Force [N]*		
	Test 1	*Test 2*	*Test 3*
0	0	0	0
5	0.05	0.05	0.05
10	0.09	0.10	0.09
15	0.14	0.14	0.12
20	0.19	0.18	0.17
25	0.22	0.24	0.23
30	0.28	0.28	0.31
35	0.34	0.32	0.33
40	0.37	0.36	0.36
45	0.40	0.37	0.38
50	0.44	0.42	0.45

Experiment 2: Static buckling 0.2 mm

Deflection [mm]	*Force [N]*		
	Test 1	*Test 2*	*Test 3*
0	0	0	0
1	1.00	0.98	1.18
2	1.44	1.64	1.67
3	1.90	1.93	1.88
4	2.08	2.01	1.96
5	2.12	2.08	2.05
6	2.13	2.12	2.10
7	2.14	2.14	2.11
8	2.15	2.15	2.12
9	2.16	2.17	2.14
10	2.19	2.19	2.16

Experiment 2: Static buckling 0.3 mm

Deflection [mm]	*Force [N]*		
	Test 1	*Test 2*	*Test 3*
0	0	0	0
1	3.25	3.42	3.04
2	7.07	5.48	5.27
3	7.56	6.52	6.63
4	7.61	7.29	7.39
5	7.72	7.94	7.55
6	7.77	8.26	8.15
7	7.78	8.59	8.42
8	7.83	8.59	8.42
9	7.83	8.54	8.48
10	7.83	8.32	8.48

Experiment 3: Straight trajectory drilling 0.3 mm

Removed mass per cut of the prototype

5 PCF 50 mm/min 22,000 rpm			
cut	m_{before} *[g]*	m_{after} *[g]*	$m_{removed}$ *[g]*
1	7.923	7.865	0.058
2	7.865	7.791	0.074
3	7.791	7.697	0.094
4	7.697	7.620	0.077
5	7.620	7.527	0.093
6	7.522	7.448	0.074

10 PCF 50 mm/min 22,000 rpm			
cut	m_{before} *[g]*	m_{after} *[g]*	$m_{removed}$ *[g]*
1	16.032	15.849	0.183
2	15.849	15.690	0.159
3	15.690	15.543	0.147
4	15.543	15.413	0.130
5	15.413	15.278	0.135

5 PCF 30 mm/min 22,000 rpm			
cut	m_{before} *[g]*	m_{after} *[g]*	$m_{removed}$ *[g]*
1	7.446	7.391	0.055
2	7.391	7.312	0.079
3	8.212	8.154	0.058
4	8.154	8.091	0.063
5	8.675	8.590	0.085

5 PCF 70 mm/min 22,000 rpm			
cut	m_{before} *[g]*	m_{after} *[g]*	$m_{removed}$ *[g]*
1	8.590	8.518	0.072
2	8.518	8.456	0.062
3	8.456	8.394	0.062
4	8.394	8.342	0.052
5	8.342	8.267	0.075

5 PCF 50 mm/min 16,000 rpm			
cut	m_{before} [g]	m_{after} [g]	$m_{removed}$ [g]
1	8.267	8.200	0.067
2	8.079	8.031	0.048
3	8.031	8.001	0.030
4	7.965	7.878	0.087
5	7.878	7.775	0.103

5 PCF 50 mm/min 10,000 rpm			
cut	m_{before} [g]	m_{after} [g]	$m_{removed}$ [g]
1	7.712	7.637	0.075
2	7.637	7.573	0.064
3	7.573	7.524	0.049
4	7.524	7.464	0.060
5	7.464	7.406	0.058

Removed mass per cut of the conventional drill

5 PCF 50 mm/min 200 rpm			
cut	m_{before} [g]	m_{after} [g]	$m_{removed}$ [g]
1	8.483	8.427	0.056
2	8.427	8.375	0.052
3	8.375	8.322	0.053
4	8.322	8.274	0.048
5	8.274	8.223	0.051

10 PCF 50 mm/min 200 rpm			
cut	m_{before} [g]	m_{after} [g]	$m_{removed}$ [g]
1	17.603	17.507	0.096
2	17.507	17.411	0.096
3	17.411	17.313	0.098
4	17.313	17.212	0.101
5	17.212	17.119	0.093

ACKNOWLEDGMENT

I would like to pay my special regards to Ir. Esther de Kater for her help and guidance throughout this project. This research would not have taken shape without her insight and experience. Also, I would like to thank precision technician David Jager for manufacturing and repairing the prototypes.

REFERENCES

[1] E. Verdult, “Drilling Back, Design & Development of a Directional Drilling Device, New Spinal Anchoring Technique,” Delft Universitly of Technology, 1998.

[2] P. J. Mansfield and D. A. Neumann, *Essentials of Kinesiology for the Physical Therapist Assistant*, 3rd editio. Mosby, 2019.

[3] R. B. Ashman and Jae Young Rho, “Elastic modulus of trabecular bone material,” *J. Biomech.*, 1988, doi: 10.1016/0021-9290(88)90167-4.

[4] G. Burström *et al.*, “Diffuse reflectance spectroscopy accurately identifies the pre-cortical zone to avoid impending pedicle screw breach in spinal fixation surgery,” *Biomed. Opt. Express*, 2019, doi: 10.1364/boe.10.005905.

[5] C. Bergot, A. M. Laval-Jeantet, F. Prêteux, and A. Meunier, “Measurement of anisotropic vertebral trabecular bone loss during aging by quantitative image analysis,” *Calcif. Tissue Int.*, 1988, doi: 10.1007/BF02571311.

[6] R. A. Deyo, A. Nachemson, and S. K. Mirza, “Spinal-Fusion Surgery — The Case for Restraint,” *N. Engl. J. Med.*, 2004, doi: 10.1056/nejmsb031771.

[7] P. T. Guillen, R. G. Knopper, J. Kroger, N. D. Wycliffe, O. A. Danisa, and W. K. Cheng, “Independent assessment of a new pedicle probe and its ability to detect pedicle breach: A cadaveric study - Laboratory investigation,” *J. Neurosurg. Spine*, 2014, doi: 10.3171/2014.6.SPINE131028.

[8] T. Fujimoto, A. Sei, T. Taniwaki, T. Okada, T. Yakushiji, and H. Mizuta, “Pedicle screw diameter selection for safe insertion in the thoracic spine,” *Eur. J. Orthop. Surg. Traumatol.*, 2012, doi: 10.1007/s00590-011-0846-2.

[9] S. B. Lien, N. H. Liou, and S. S. Wu, “Analysis of anatomic morphometry of the pedicles and the safe zone for through-pedicle procedures in the thoracic and lumbar spine,” *Eur. Spine J.*, 2007, doi: 10.1007/s00586-006-0245-2.

[10] H. C. Sagi, R. Manos, R. Benz, N. R. Ordway, and P. J. Connolly, “Electromagnetic field-based image-guided spine surgery part one: Results of a cadaveric study evaluating lumbar pedicle screw placement,” *Spine (Phila. Pa. 1976).*, 2003, doi: 10.1097/01.BRS.0000087851.51547.00.

[11] A. R. Vaccaro *et al.*, “Placement of pedicle screws in the thoracic spine: Part II: An anatomical and radiographic assessment,” *J. Bone Jt. Surg. - Ser. A*, 1995, doi: 10.2106/00004623-199508000-00009.

[12] M. F. A. Akhbar and A. R. Yusoff, “Optimization of drilling parameters for thermal bone necrosis prevention,” *Technol. Heal. Care*, 2018, doi: 10.3233/THC-181221.

[13] B. Bhushan, “Insects locomotion, piercing, sucking and stinging mechanisms,” *Microsyst. Technol.*, vol. 24, no. 12, pp. 4703–4728, 2018, doi: 10.1007/s00542-018-4175-9.

[14] U. Cerkvenik, B. Van De Straat, S. W. S. Gussekloo, and J. L. Van Leeuwen, “Mechanisms of ovipositor insertion and steering of a parasitic wasp,” *Proc. Natl. Acad. Sci. U. S. A.*, vol. 114, no. 37, pp. E7822–E7831, 2017, doi: 10.1073/pnas.1706162114.

[15] Y. Gao, A. Ellery, M. Jaddou, and J. Vincent, “Deployable wood wasp drill for planetary subsurface sampling,” in *IEEE Aerospace Conference Proceedings*, 2006, vol. 2006, [Online]. Available: https://www.scopus.com/inward/record.uri?eid=2-s2.0-34047094505&partnerID=40&md5=1c7b32a3ba84002b0f2ce0dc122973d2.

[16] H. W. Krenn and H. Aspoeck, “Form, function and evolution of the mouthparts of blood-feeding Arthropoda,” *ARTHROPOD Struct. Dev.*, vol. 41, no. 2, pp. 101–118, 2012, doi: 10.1016/j.asd.2011.12.001.

[17] J. Chaudonneret, “Les pièces bucales des Insectes : Thèmes et variations.,” *Bull. Mens. la Société linnéenne Lyon*, vol. 60, no. 8, p. 302, 1990.

[18] A. Wenk, P., Renz, “Parasitologie: Biologie der Humanparasiten.,” *Georg Thieme Verlag, Stuttgart, New York*, 2003.

[19] A. Sendrowicz, M. Scali, C. Culmone, and P. Breedveld, “Surgical drilling of curved holes in bone–a patent review,” *Expert Review of Medical Devices*. 2019, doi: 10.1080/17434440.2019.1596794.

[20] U. Cerkvenik, D. Dodou, J. L. van Leeuwen, and S. W. S. Gussekloo, “Functional principles of steerable multi-element probes in insects,” *Biol. Rev.*, vol. 94, no. 2, pp. 555–574, 2019, doi: 10.1111/brv.12467.

[21] A. Sakes, D. Dodou, and P. Breedveld, “Buckling

prevention strategies in nature as inspiration for improving percutaneous instruments: a review," *Bioinspir. Biomim.*, vol. 11, no. 2, Apr. 2016, doi: 10.1088/1748-3190/11/2/021001.

[22] S. Oikonomidis *et al.*, "Probe versus drill: A biomechanical evaluation of two different pedicle preparation techniques for pedicle screw fixation in human cadaveric osteoporotic spine," *Clin. Biomech.*, 2020, doi: 10.1016/j.clinbiomech.2020.104997.

[23] Sawbones, "BIOMECHANICAL TEST MATERIALS VALIDATION STUDIES | SAWBONES." https://www.sawbones.com/validation-studies (accessed Nov. 15, 2021).

[24] A. Vaccaro, F. Kandziora, M. Fehlings, and R. Shanmughanathan, "AO Surgery Reference, Pedicle screw insertion." https://surgeryreference.aofoundation.org/spine/trauma/thoracolumbar/basic-technique/pedicle-screw-insertion (accessed Apr. 17, 2021).

[25] "Bioskills Lab: Posterior Pedicle Screws - Robert Hart, M.D.," *Seattle Science Foundation*. https://www.youtube.com/watch?v=Xm89f28pzTM (accessed May 06, 2021).

[26] I. Gilad and M. Nissan, "Sagittal evaluation of elemental geometrical dimensions of human vertebrae.," *J. Anat.*, 1985.

[27] S. Malkin, "Grinding Processes," in *Encyclopedia of Tribology*, Q. J. Wang and Y.-W. Chung, Eds. Boston, MA: Springer US, 2013, pp. 1573–1580.

[28] D. Birmingham, *Pop-up!: A Manual of Paper Mechanisms,* 2nd ed. Tarquin, 1997.

[29] C. Culmone, P. W. J. Henselmans, R. I. B. van Starkenburg, and P. Breedveld, "Exploring non-assembly 3D printing for novel compliant surgical devices," *PLoS One*, 2020, doi: 10.1371/journal.pone.0232952.

[30] S. Kalpakjian and S. Schmid, *Manufacturing engineering and technology, SI 6th Edition*. 2013.

[31] "Black and Decker Model Nr. MT300KA 300W Oscillerende Multitool." https://www.blackanddecker.nl/products/power-tools/multi-tools/300w-oscillerende-multitool/mt300ka (accessed May 06, 2021).

[32] thyssenkrupp Materials UK, "Stainless Steel 301 1.4310." https://www.thyssenkrupp-materials.co.uk/stainless-steel-301-14310.html.

[33] "All Accessories," *Dremel*. https://us.dremel.com/en_US/accessories-and-attachments/-/subcategory/accessory/find-by-tool/27343/rotary/904 (accessed Jun. 16, 2021).

[34] F. Karaca, M. Köm, and B. Aksakal, "Structural and histopathologic changes of calf tibial bones subjected to various drilling processes," *Kafkas Univ. Vet. Fak. Derg.*, 2013, doi: 10.9775/kvfd.2012.7884.

[35] Minitab, "Interpret the key results for One-Way ANOVA," 2019. https://support.minitab.com/en-us/minitab-express/1/help-and-how-to/modeling-statistics/anova/how-to/one-way-anova/interpret-the-results/key-results/.

[36] H. Attia, A. Sadek, and M. Meshreki, "High speed machining processes for fiber-reinforced composites," in *Machining Technology for Composite Materials*, 2012.

[37] R. K. Pandey and S. S. Panda, "Drilling of bone: A comprehensive review," *Journal of Clinical Orthopaedics and Trauma*. 2013, doi: 10.1016/j.jcot.2013.01.002.

[38] Köhler J., "Grinding Parameters. In: The International Academy for Production Engineering," *CIRP Encycl. Prod. Eng.*, 2014, doi: https://doi.org/10.1007/978-3-642-20617-7_6424.

[39] N. B. Dahotre and S. S. Joshi, *Machining of bone and hard tissues*. 2016.

[40] S. Kannappan and S. Malkin, "Effects of grain size and operating parameters on the mechanics of grinding," *J. Manuf. Sci. Eng. Trans. ASME*, 1972, doi: 10.1115/1.3428258.

[41] S. Malkin and C. Guo, *Grinding Technology - Theory and Applications of Machining with Abrasives (2nd Edition)*. Industrial Press, 2008.

[42] K. Wegener, "Ploughing (in Grinding)," in *CIRP Encyclopedia of Production Engineering*, 2014.

[43] M. Stauber and R. Müller, "A sensitivity analysis of the volumetric spatial decomposition algorithm," *Comput. Methods Biomech. Biomed. Engin.*, 2007, doi: 10.1080/10255840601090053.

[44] V. Shim, J. Boheme, C. Josten, and I. Anderso, "Use of Polyurethane Foam in Orthopaedic Biomechanical Experimentation and Simulation," in *Polyurethane*, 2012.

[45] J. Elfar, R. M. G. Menorca, J. D. Reed, and S. Stanbury, "Composite bone models in orthopaedic surgery research and education," *Journal of the American Academy of Orthopaedic Surgeons*. 2014,

doi: 10.5435/JAAOS-22-02-111.

[46] ISO 13314:2011, “Mechanical testing of metals - Ductility testing - Compression test for porous and cellular metals,” *Int. Stand.*, 2011.

[47] X. Banse, T. J. Sims, and A. J. Bailey, “Mechanical properties of adult vertebral cancellous bone: Correlation with collagen intermolecular cross-links,” *J. Bone Miner. Res.*, 2002, doi: 10.1359/jbmr.2002.17.9.1621.

[48] D. Zaytsev, M. V. Gilev, and M. Y. Izmodenova, “Mechanisms of Fracture of the Trabecular Bone Tissue of Periarticular Localization during a Depressed Fracture,” *Russ. Metall.*, 2020, doi: 10.1134/S0036029520040369.

[49] Edmund Isakov, “Understanding tangential cutting force when milling,” *Cutting Tool Engineering*, 2012. https://www.ctemag.com/news/articles/understanding-tangential-cutting-force-when-milling# (accessed Jun. 16, 2021).

[50] “Euler’s Column Formula,” *The Engineering Toolbox*, 2012. https://www.engineeringtoolbox.com/euler-column-formula-d_1813.html (accessed Jun. 16, 2021).

[51] D. A. Neumann, *Kinesiology of the Musculoskeletal System Foundations for Rehabilitation*, 2nd Editio. Mosby, 2009.

[52] M. Malowney, “The Shock Absorbers of the Spine,” 2013. http://drmchiro.blogspot.com/2013/02/the-shock-absorbers-of-spine.html (accessed Apr. 13, 2021).

[53] “Victrex,” *Weigao uses semi-rigid rods made of PEEK-OPTIMA*, 2015. https://www.victrex.com/pt-br/news/2015/05/weigao-uses-semi-rigid-rods-made-of-peek-optima (accessed Jul. 10, 2021).

[54] Y. Chen, S. Deb, R. Jabarkheel, L. Pham, M. Patel, and H. Singh, “Minimally Invasive Lumbar Pedicle Screw Fixation Using Cortical Bone Trajectory: Functional Outcomes,” *Cureus*, 2018, doi: 10.7759/cureus.3462.

[55] W. Gibson, L. Peacock, and R. Hutchinson, “Microarchitecture of the tsetse fly proboscis,” *Parasites and Vectors*, vol. 10, no. 1, 2017, doi: 10.1186/s13071-017-2367-2.